PROCEEDINGS OF THE 31ST ANNUAL CONDENSED MATTER AND MATERIALS MEETING

WAGGA WAGGA

6 – 9 FEBRUARY 2007

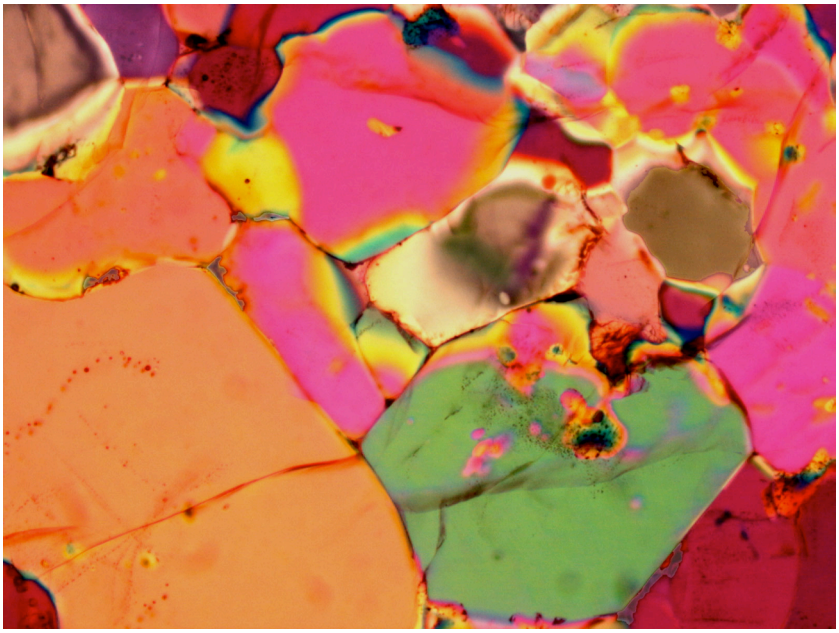

ISBN 978-0-9598064-9-6

THEORY, MODELLING & EXPERIMENTAL APPROACHES IN
CONDENSED MATTER PHYSICS & CHEMISTRY
MATERIALS SCIENCE & ENGINEERING
SPECTROSCOPY & SYNCHROTRON PHYSICS
NEUTRON DIFFRACTION & SCATTERING
NANOSCIENCE & NANOTECHNOLOGY
CERAMIC & GEOLOGICAL MATERIALS
SOFT MATTER, SURFACE & INTERFACE SCIENCE
MAGNETIC, ELECTRONIC & PHOTONIC MATERIALS

Every presenter at this Meeting in Wagga Wagga was invited to submit a manuscript of 3 pages for the Conference Proceedings. Manuscripts submitted during the Meeting were each reviewed anonymously by 2 peers.

Manuscript-review Team :- A. Barnhoorn, K.D. Becker , J.E. Butler, S.J. Campbell, J.D. Cashion, Y. Chen, B.-M. Cheng, M.B. Cortie, S.A. Danilkin, M.P. Das, G.J.J.B. de Groot, T.R. Finlayson, J.D. Gale, D.J. Goossens, C.J. Hamer, I. Jackson, M. James, A-K. Larsson, R.A. Lewis, C.D. Ling, Y. Liu, N.R. Lobanov, J.C. Macfarlane, N.B. Manson, C. Martelli, D.A. Neumann, L. Noren, D.C. Price, N. Savvides, J.R. Sellar, M.J. Sellars, T.J. Senden, J.G. Shapter, D.Q. Shi, C. Sloggett, A.E. Smith, G.A. Stewart, G.J. Troup, E.R. Vance, E.G. Wang, G. White and R.L. Withers.

Selection of reviewers, transmission of their comments and subsequent vetting of authors' revisions were handled by members of the Editorial Team:

A. Barnhoorn[1], J.D. Fitz Gerald[1], I. Jackson[1] and T.J. Senden[2].

[1] Research School of Earth Sciences

[2] Research School of Physical Sciences and Engineering

Both at Australian National University, ACT 0200, Australia.

Correspondence: john.fitzgerald@anu.edu.au

ORAL CONTRIBUTIONS

What controls the shapes of crystals? Insights from computer simulation

Julian Gale, Curtin University ***INVITED***

The 0.7 structure: correlated electron flow through a quantum point contact at finite temperature

Clare Sloggett, UNSW

High-ZT thermoelectric materials

Nick Savvides, CSIRO Industrial Physics

Cation, anion and charge ordering in the misfit-layered thermoelectric $[Ca_2CoO_{3-\square}][CoO_2]_q$, q □ 1.61

Chris Ling, University of Sydney

Probing the properties of III-nitrible-based materials for opto- and magneto-electronic device applications from first principles

Catherine Stampfl, University of Sydney ***INVITED***

Size dependence of critical transition temperature of MgB2

Chuncheng Yang, UNSW

Unusual magnetic behaviour: thermal and spontaneous remagnetisation in $Nd_3(Fe,Ti)_{29}$ and $Nd_3(Fe,Re)_{29}$

Steve Collocott, CSIRO Industrial Physics

A step up to self-assembly

Enge Wang, Chinese Acad. of Sciences, Beijing ***INVITED***

Spectroscopic studies into the reactivity of solids

Klaus Becker, Braunschweig University of Technology, Braunschweig, Germany ***INVITED***

Luminescence of blue diamonds: donor-acceptor pair recombination?

James Butler, Naval Research Laboratory, Washington, DC, USA

Porphyrin thin-films inside structured optical fibres

Cicero Martelli, University of Sydney

AC impedance spectroscopy study of geopolymers doped with Ca and Mg cations and Cl, NO_3 and SO_4 anions

Philip Walls , ANSTO

What to do when your nuclear reactor goes critical

Michael James, Bragg Institute, ANSTO ***INVITED***

The effect of filters on X-ray phase contrast imaging

Anthony Greaves, Swinburne University, Melbourne

Material analysis using high energy electron back-scattering

Michael Went, ANU

Frequency-modulated superconducting infra-red detector

John Macfarlane, Strathclyde University, Glasgow, UK

Neutrons and hydrogen storage materials

Dan Neumann, NIST, Gaithersburg, Maryland, USA ***INVITED***

Inelastic neutron scattering of $Tb_2Sn_2O_7$

Kirrily Rule, Hahn-Meitner Institut, Berlin, Germany

Superstucture phase of microwave dielectric $(Bi_{1.5}Zn_{0.5})(Ti_{1.5}\ Nb_{0.5})O_7$ pyrochlore

Yun Liu, ANU

Product and process development through understanding and manipulating nano-scale molecular and surface forces

Calum Drummond, CSIRO Industrial Physics ***INVITED***

The Australian Synchrotron - a new facility for research

Nigel Kirby, Australian Synchrotron, Melbourne ***INVITED***

Three-layer Aurivillius phases containing magnetic transition metal cations: Ru (IV), Ir (IV) and Mn (IV)

Neeraj Sharma, University of Sydney

Crystallography of biomimetic silica carbonate precipitates

Ann-Kristin Larsson, ANU

Functionalisation of silicon substrates using single walled carbon nanotubes

Joseph Shapter, Flinders University ***INVITED***

Cathodoluminescence for high resolution non-destructive luminescence depth profiling of nanocrystal layers

Annette Dowd, University of Technology Sydney

Hydration of cement: application of quasielastic and inelastic neutron scattering

Vanessa Peterson, Bragg Institute, ANSTO

X-ray anomalous scattering and X-ray absorption spectroscopy methods to study the Au overlayer to prevent the aggregation of monolayer FePt nanoparticles

Chih-hao Lee, National Tsing Hua University, Hsinchu, Taiwan

Can computed tomography replace lab work?

Tim Senden, ANU

Investigating the photonic behaviors of ZnO nanocrystals

Yee-yan Tay, Nanyang Technological University, Singapore

Recent applications of ion-surface modification

John Colligon, Manchester Metropolitan University, UK ***INVITED***

POSTER CONTRIBUTIONS

Authors	Title
A. Ahmad	Characterization of Ta-doped Titanium Dioxide Nanoparticles Produced by Sol-gel Method
Y. Aizawa, A. Barnhoorn, U.H. Faul, J.D. FitzGerald and I. Jackson	The Influence of Water on Seismic Wave Attenuation in the Earth's Upper Mantle: an Exploratory Experimental Study
A.L. Alexander, J.J. Longdell, M.J. Sellars, G. Hétet and P.K. Lam	Quantum Optics Using Solid State Materials
P.A. Altin and D.J. Goossens	Diffuse X-ray Scattering from Optically Pure Ibuprofen
J. Armellin and S. Li	The Size Dependence of the Mechanical Properties of ZnO Nanobelts
N. Armstrong, R.C. Hoft, M.J. Ford and M.B. Cortie	Asymmetric Tunneling Currents across Metal-molecule-metal Junctions
N. Armstrong	Model Selection Method Using Bayesian Techniques in X-ray Reflectometry
H. Bai M. Berkahn and M.B. Cortie	Effect of Reduction and Calcination on the Preparation of VO_2-M_1: an Optically Functional 'Smart' Material.
A. Barnhoorn, I. Jackson and J.D. Fitz Gerald	Grain-size Sensitive Viscoelastic Relaxation in High-purity MgO
R. Barry and S. Hodgman	Development of a Simulation Board Game Based on the Physical Principles of Superconductivity and Magnetism for Use as a Teaching Aid
S.E. Beavan, E. Fraval, J.J. Longdell and M.J. Sellars	Experimental Investigation of the Use of Multiple Pulse Sequences to Minimise the Decoherence of Solid State Qubits
M. Binder, B. Usher, J. Petrolito	Cancellation of Surface Streses due to Threading Dislocations

C. Bowles, A.S. Kheifets, M. Vos and M.R. Went	Electron Momentum Spectroscopy of Single Crystal Noble Metals
J.D. Cashion, W.P. Gates and A. Thomson	Determination of Cation Site Distributions in Clay Minerals
H. Chen, Y. Chen, C.-P Li, H. Zhang, J.S. Williams, Y. Liu, Z. Liu and S.P. Ringer	Cathodoluminescence of Boron Nitride Nanotubes Doped by Europium
Y. Chen, H. Chen, J. Yu, V. Craig and J.S. Williams	Focused Ion Beam Milling as a New Template Technique for Patterned Growth of Carbon Nanotubes
Y.-J. Chen, B. Chi, Q-X. Liu, D.C. Mahon and Y. Chen	Mullite ($Al_{5.65}Si_{0.35}O_{9.175}$) nanowires
W.-H. Zheng, C.J. Hamer, R.R.P. Singh	Emergence of Composite Spin-One Behaviour in Alternating Spin-Half Chains
S.A. Danilkin	Neuron Scattering Study of Diffuse Scattering and Lattice Dynamics of Fast Ionic Conductor $Cu_{2-\square}Se$
B. Fairchild, P. Olivero, A. Cimmino, M. Draganski, B.C. Gibson, A.D. Greentree, D. Hoxley, S.T. Huntington, J. Rabeau, P. Reichart, S. Rubanov, A. Stacey, J. Salzman, B. Meyler, I. Bayn, A. Lahav, D.N. Jamieson and S. Prawer	Fabrication of Nanostructures in Single-Crystal Diamond
T.R. Finlayson, J.R. Griffiths, D.M. Viano, M.E. Fitzpatrick, E.C. Oliver, and Q.G. Wang	The Partition of Stresses in Al-Si-based Metal-Matrix Composites
A. Glushenkov, H.Z. Zhang, J. Zou, G.Q. Lu and Y. Chen	Growth of Oxide Nanostructures by Annealing of Ball Milled ZnO and V_2O_5 Powders
D.J. Goossens and A.P. Heerdegen	ZMC: A Program for Modelling Short-Range Order in Molecular Crystals
Z.P. Guo, L. Liu and H.K. Liu	Electro-oxidation of Methanol on Pt-POM/CNT Electrocatalyst
M.P. Hedges, J.J. Longdell and M.J. Sellars	Coherence Time Measurements of the Electronic Ground State Hyperfine Transitions Eu^{3+}: Y_2SiO_5
W.D. Hutchison, G.J. Bowden and L. Norén	HoF_3 as a Low Temperature Refrigerant

W.D. Hutchison, D.J. Goossens, B. Saensunon, G.A. Stewart, M. Avdeev and K. Nishimura	Magnetic Order Studies of $ErNiAl_4$
J. Kolmeder, D.A. Scott and D.C. Price	In Situ Monitoring of Corrosion in Aluminium Sheet
J.C. Lashley, N. Hur, B. Mihaila, J.L. Smith, T.R. Finlayson, C.P. Opeil, R.A. Fisher	Effects of Electric and Magnetic Fields on the Thermophysical Properties of Triglycine Sulphate - New Results on an Old Material!
R.A. Lewis and L.J. Bignell	Terahertz Reflectance of III-V, II-VI and I-VII Crystals
R.A. Lewis and D. Pond	Electroresistance of Electronic Oxides
L. Li, Y. Chen and C.P. Li	Thin Layer Coating of Boron Nitride Nanotubes
N.R. Lobanov, D.C. Weisser	Intermodulation Measurements in Electroplated PbSn Superconducting Split-Loop Resonators
N. Loh, D.-H. Yu, C. Harland, R.A. Robinson, A.P.J. Stampfl, R. Stamps, Y.-C. Tseng, and D. Haskel	The Magnetism of CrO_2 under Pressure Studied Using Hard X-Ray Magnetic Circular Dichroism
N. Loh, P. Brigden, D.-H. Yu, J.D. Riley, R.L. Stamps, C. Harland, R.A. Robinson, A.P.J. Stampfl, J.W. Freeland, D.J. Keavney and R.A. Rosenberg	Spin Glass Dynamics Studied Using Soft X-Ray Magnetic Circular Dichroism
L. Lu, R. Zeng, J.L. Wang, D.Q. Shi, J. Horvat, H.K. Liu and S.X. Dou	Enhancement of Superconducting Properties of MgB_2 by C-nanocoating on B Particles
N.B. Manson, J.P. Harrison, R.L. McMurtrie, M.J. Sellars, Ph. Tamarat, F. Jelezko and J. Wrachtrup	N-V centre in Diamond for Quantum Information Processing
D.J. Miller	Control of Entanglement in a Closed, 3-qubit System Interacting via an Isotropic Heisenberg Hamiltonian
J. Murison, L. Wong, M.J.Y. Tayebjee, N. Loh, D.-H. Yu, G. Triani, P. Evans, L. Vance, A.P.J. Stampfl, R. Clements, C.D. Ling, B. Kennedy and T.-W. Pi	The Valence Electronic Structure of ZrO_2
L. Norén, A.-K. Larsson, R.L. Withers and H. Rundlöf	Te for Two, II: A Neutron Powder Diffraction Study of the Structure of the "Ni_2InTe_2" Solid Solution

J. Oitmaa, W.H. Zheng and C.J. Hamer	The Spin-1 Heisenberg Magnet with Uniaxial $(S^z)^2$ Anisotropy
J. Oitmaa and I.G. Enting	A Simple Ferrimagnetic Ising Model
R.O. Piltz	Domain Structure of Ferroelectric PZN-PT during Poling
M.N. Read	Electronic Surface Band Structure of Cu(111) by the 2D Green's Function (KKR) Method
B. Saensunon, K. Nishimura and G.A. Stewart	The Magnetic Environment of the Rare Earth Site in the Intermetallic Compounds RCr_2Si_2 and RMn_2Si_2 (R = rare earth)
P.J. Saines, J. Spencer and B.J. Kennedy	Interesting Phase Transitions in $Ba_2LnB'O_6$: a Finely Balanced Series
H.A. Salama, D. Scott, J.B. Taboada, N. Strickland, H. O'Neill and G.A. Stewart	Preparation of Orthorhomobic Phase of $YbMnO_3$ and $Yb_{2/3}Ca_{1/3}MnO_3$
M.A. Santin and G.J.J.B. de Groot	Vibration Characterisation of a Joule-Thomson Cryocooler for a SQUID-based Metal Detection System
N. Savvides and S.A.G. Vrouwe	Niobium Step Josephson Junctions
M.J. Sellars, J.P. Harrison, N.B. Manson and J. Rabeau	Investigating the Use of the Nitrogen-Vacancy Centre in Diamond Nano-crystals as a Single Electron Spin Probe
D. Shi, A. Li, R. Zeng, X. Wang and S.X. Dou	$La_{0.7}Sr_{0.3}MnO_3$ Buffer Laser Deposited by PLD
A.E. Smith	Scattering Potentials in Condensed Matter for Very Low Energy Electrons
A.P.J. Stampfl, N. Loh, L. Wong, M.J.Y. Tayebjee, D.-H. Yu, R.A. Robinson, R.L. Stamps, P. Brigden, J.D. Riley and T.-W. Pi	Valance-band Photoemission Studies of $Cu_{0.75}Mn_{0.25}(100)$
A. Sudholz, A.J. Hill, T.J. Bastow and J.R. Sellar	PALS Study of Cubic Yttria-Stabilized Zirconia
N. Suwuntanasarn, W.D. Hutchison, G.D. Milford and R. Bramley	A Novel Probe Head for an Electron Spin Echo Study of an Australian Coal

C. Ton-That	Characterisation of Endohedral Fullerenes Using Synchrotron-based Techniques
G.J. Troup, L. O'Dea, D.R. Hutton and S. Langford	EPR and Antioxidant Studies of a Red Wine Vinegar and a Cider Vinegar
G.J. Troup and D.R. Hutton	An EPR Study of Dark (>75% Cocoa) Chocolate
G.J. Troup, D.R. Hutton, L. O'Dea and S. Langford	EPR and Antioxidant Efficiency Comparisons of the Flavonoids Quercitin and Fisetin
G.J. Troup, L. O'Dea, S. Langford and D.R. Hutton	Resveratrol: EPR and Antioxidant Efficiency Studies
E.R. Vance and J.H. Hadley	Positron Annihilation Lifetime Spectroscopy in Titanate Ceramics
M. Went, M. Vos, Y. Zhao, Y. Wu and S-X. Dou	Electron Rutherford Backscattering as a Surface Analytical Tool: a Case Study of MgB_2 Films
J.L. Wang, S.J. Campbell, M. Avdeev, A.J. Studer, M. Hofmann, M. Hoelzel	Magnetic Structures of $Pr_{1-x}Y_xMn_2Ge_2$ Compounds
N.A.S. Webster, F.J. Lincoln, C.L. Raston and C.D. Ling	Fluorite-type Bi_2O_3-Ln_2O_3 - PbO Materials: Structure and Conductivity
K.F. Wilson and D.J. Goossens	Improving Student Engagement in Third Year CMP: a Case Study
R.L. Withers, Y. Liu, X. Wei and J.D. Fitz Gerald	Structured Diffuse Scattering and Polar Nano Regions in the $Ba(Ti_{1-x}Sn_x)O_3$ Relaxor Ferroelectric System
X.Y. Xiong and T.R. Finlayson	Phase Transformation and Magnetic Properties of Melt-Spun $Sm(Co_{0.68}Fe_{0.2}Cu_{0.1}Zr_{0.02})_{7.5}$ Alloy Ribbons
J. Yu, D. Yu, Y. Chen, L. Li, B.-M. Cheng and A. Stampfl	Photoluminescence Spectroscopy of BN Nanotubes Using Synchrotron VUV Radiation
J. Yu, Y. Chen, R.G. Elliman, M. Petravic, D.-H. Yu, M.M. Elcombe and M. Tayebjee	Istoptically Enriched ^{10}BN Nanotubes for Shielding Deep-space Radiations
R. Zeng, J.L. Wang, D.Q. Shi, L. Lu, H.K. Liu and S.X. Dou	Effect of Ni Substitution for Mn on the Magnetic and Magnetocaloric Properties of $(Mn_{1-x}Ni_x)_3Sn_2$ Compounds

R. Zeng, R. Pierre, Z.P. Guo, L. Lu, D.Q. Shi, H.K. Liu and S.X. Dou	New Synthesis Route and Electromagnetic Properties of $Dy_{1-x}Ca_xMnO_3$

CONTENTS OF THE PROCEEDINGS

15. *Intermodulation measurements in electroplated PbSn superconducting split-loop resonators*
N.R. Lobanov and D.C. Weisser

16. *Control of entanglement in a closed, 3-qubit system interacting via an isotropic Heisenberg Hamiltonian*
D.J. Miller

17. *Te for two II: A neutron powder diffraction study of the structure of the "Ni_3InTe" solid solution*
L. Noren, A.-K. Larsson, R.L. Withers and H. Rundlöf

18. *A simple ferrimagnetic Ising model*
J. Oitmaa and I.G. Enting

19. *The spin-1 Heisenberg magnet with uniaxial $(S^z)^2$ anisotropy*
J. Oitmaa, W.H. Zheng and C.J. Hamer

20. *Electronic surface band structure of Cu(111) by the 2D Green's function (KKR) method*
M.N. Read

21. *The magnetic environment of the rare earth site in RT_2Si_2 compounds (R = rare earth, T = Cr & Mn)*
B. Saensunon, K. Nishimura and G.A. Stewart

22. *Preparation of orthorhombic phase $YbMnO_3$ and $Yb_{2/3}Ca_{1/3}MnO_3$*
H.A. Salama, D. Scott, J.B. Taboada, N. Strickland, H. O'Neill & G.A. Stewart

23. *Vibration characterisation of a Joule-Thomson cryocooler for a SQUID-based metal detection system*
M.A. Santin and G.J.J.B. de Groot

24. *Niobium step Josephson junctions*
N. Savvides and S. A. G. Vrouwe

25. *Neutron diffraction results for three-layer Aurivillius phases containing magnetic transition metal cations: Ru (IV), Ir (IV) and Mn (IV).*
N. Sharma, B.J. Kennedy, M.M. Elcombe, M. Avdeev and C.D. Ling

26. *Scattering potentials in condensed matter for low energy electrons*
A.E. Smith

27. *A novel probe head for an electron spin echo study of an Australian coal*
N. Suwuntanasarn, W.D. Hutchison, G. Milford and R. Bramley

28. *Investigating the photonic behaviours of ZnO nanocrystals*
Y.Y. Tay, S. Li and M.H. Liang

29. *Mössbauer spectroscopy of iron sites in four Na- and Ca-saturated ferruginous smectites*
A. Thomson, J.D. Cashion, W.P. Gates

30. *EPR and antioxidant efficiency studies of Resveratrol, Quercitin and Fisetin*
G.J. Troup, D.R Hutton , L. O'Dea and S.J. Langford

31. *EPR and antioxidant studies of Dark Chocolate, a Red Wine Vinegar and a Cider Vinegar*
G.J. Troup, D.R.Hutton, L. O'Dea and S.J. Langford

32. *Improving student engagement in third year CMP: a case study*
K.F. Wilson and D.J. Goossens

33. *Size dependence of critical transition temperatures of* MgB_2
C.C. Yang and S. Li

34. *Emergence of composite spin-1 behaviour in alternating spin-1/2 chains*
W. Zheng, C.J. Hamer and R.R.P Singh

The Influence of Water on Seismic Wave Attenuation in the Earth's Upper Mantle: An Exploratory Experimental Study

Yoshitaka Aizawa[a,b,c], Auke Barnhoorn[a], Ulrich H. Faul[a,d], John D. Fitz Gerald[a] and Ian Jackson[a]

[a] *Research School of Earth Sciences, Australian National University, Canberra, Australia*
[b] *Institute for Study of the Earth's Interior, Okayama University, Misasa, Japan*

Established methods for the study of viscoelastic behaviour at simultaneously high temperature and pressure have been extended to allow the maintenance of a high pore fluid pressure during prolonged annealing and micro-strain mechanical testing. A natural olivine-rich rock, initially containing water in accessory hydrous phases subjected to in situ dehydration within a welded Pt capsule, was tested with low-frequency forced-oscillation methods. The observed viscoelastic relaxation was significantly enhanced by the presence of the pressurised aqueous pore fluid.

1. Introduction

The viscoelasticity of the Earth's mantle, manifest in the dispersion and attenuation of seismic waves, is potentially strongly influenced by the presence of water – either as a free fluid phase or associated with defects in nominally anhydrous silicate minerals like olivine [1]. Here we demonstrate a new procedure for the encapsulation of rock specimens that allows high-temperature mechanical testing under water-saturated conditions.

2. Experimental method

2.1 Mechanical testing

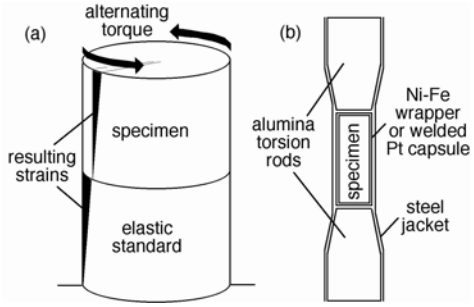

Fig. 1. (a) The principle underpinning studies of viscoelastic behaviour through observation of torsional forced oscillations. (b) Detail of the specimen assembly showing alternative arrangements in which the specimen is either wrapped in Ni-Fe foil or sealed within a welded Pt capsule.

In our laboratory, torsional forced-oscillation tests (Fig. 1a) are performed on cylindrical rock specimens under conditions of simultaneously high temperature and pressure [2]. The cylindrical rock specimen is mounted between alumina torsion rods within the hot-zone of a furnace operated within a gas-charged pressure vessel. The specimen and alumina torsion rods are housed within a thin-walled steel jacket sealed at both ends onto hollow steel

[c] *Present address: Research Center for Seismology, Volcanology and Disaster Mitigation, Nagoya University, Nagoya, Japan*
[d] *Present address: Department of Earth Sciences, Boston University, Boston, USA*

torsion members in order to exclude the argon pressure medium (Fig. 1b). Venting of the hollow interior of the steel assembly ensures that a normal stress equal to the confining pressure acts across each interface within the system, thereby providing the necessary mechanical coupling.

The specimen assembly is first subjected to a prolonged period (~100 h) of annealing at the highest working temperature T (typically 1300°C) and a confining pressure P_c of 200 MPa, during which any evolution of the mechanical behaviour associated with microstructural changes is monitored. Mechanical testing involves the conduct of forced-oscillation tests at selected oscillation periods T_o between 1 and 1000 s at maximum strain amplitudes of order 10^{-5} and complementary torsional microcreep tests of duration <10000 s. Once the mechanical behaviour has stabilized, testing is done during slow staged cooling.

2.2 Specimen preparation and characterisation

For this study we chose a fine-grained natural rock from Anita Bay, New Zealand, composed mainly of the upper-mantle mineral olivine along with ~0.3 wt % H_2O mainly in accessory hydrous silicate phases. In order to prevent chemical alteration of the ferromagnesian silicate minerals, such a specimen is normally wrapped in Ni-Fe foil (Fig. 1b) that serves to maintain an appropriate oxygen fugacity. Gravimetric analysis and Fourier-transform infrared spectroscopy were used to measure the water concentration in specimens recovered following prolonged annealing and mechanical testing. The microstructures of the starting material and recovered specimens were examined by light microscopy and SEM.

2.3 Data analysis

Analysis of the forced-oscillation experiments provides determinations of the shear modulus G and strain energy dissipation Q^{-1} for the rock specimen. These data were fitted to a model based on a Burgers creep function $J(t) = J_U + \delta J\,[1 - \exp(-t/\tau)] + t/\eta$ modified to incorporate a suitable distribution $D(\tau)$ of anelastic relaxation times τ. J_U is the unrelaxed compliance, δJ the recoverable anelastic contribution, and η the steady-state viscosity.

3. Results: mechanical testing and microstructural characterisation

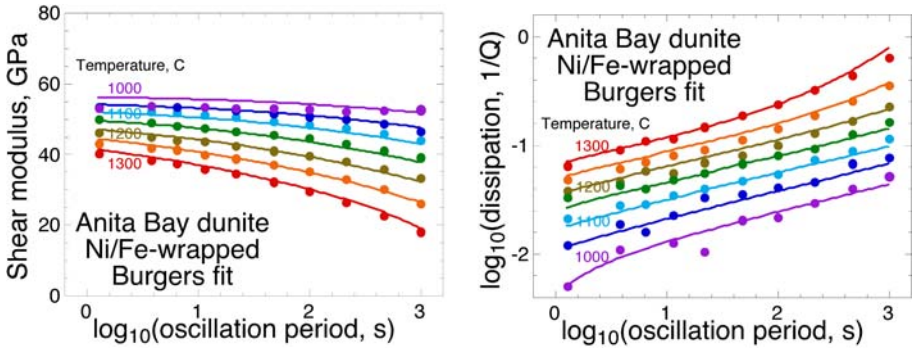

Fig. 2. The variation of shear modulus and dissipation with oscillation period and temperature for the specimen tested 'dry' within an Ni-Fe wrapper. The curves represent the Burgers model fit to the data.

The specimen tested in the Ni-Fe foil wrapper was recovered essentially dry (~40 wt ppm water) proving that this arrangement is incapable of retaining the water released by in situ dehydration for the extended duration of these experiments. The forced-oscillation tests for this specimen (Fig. 2) reveal a broad viscoelastic absorption band without any evidence of a superimposed dissipation peak.

Examination of another specimen recovered following testing within a welded Pt capsule provided clear evidence of the retention of essentially the entire inventory of water as a pressurised pore fluid occupying ~2% of newly created porosity (Fig. 3).

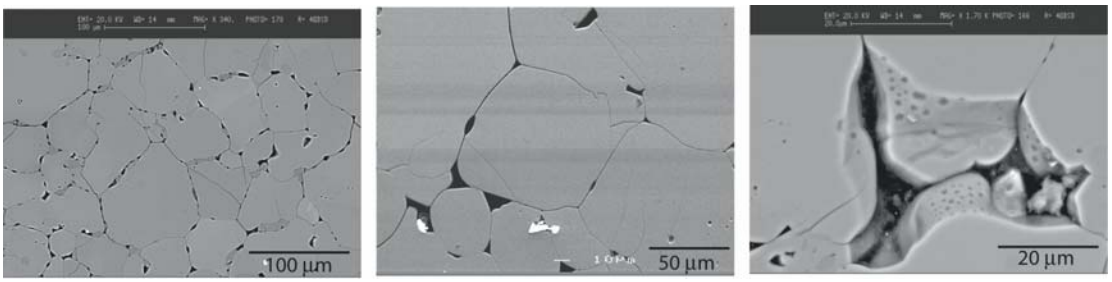

Fig. 3. SEM micrographs highlighting the porosity created in the Pt-encapsulated specimen of Anita Bay dunite during dehydration and subsequently maintained by high pore-fluid pressure.

For this specimen, tested to a maximum temperature of 1150°C, qualitatively similar absorption-band behaviour was observed but with systematically lower shear modulus and higher dissipation (Fig. 4).

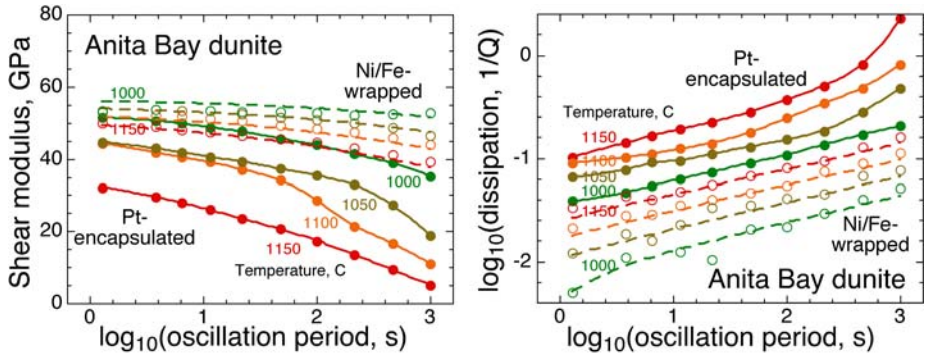

Fig. 4. A comparison of the forced-oscillation data for the essentially dry (Ni-Fe-wrapped) and water-saturated (Pt-encapsulated) specimens of Anita Bay dunite for a representative common temperature range 1000-1150°C.

4. Discussion and conclusions

This exploratory study clearly demonstrates the utility of Pt-encapsulation for essentially quantitative retention of water during prolonged periods of annealing and mechanical testing to temperatures of 1150°C at a confining pressure of 200 MPa. The overall textural maturity of the specimens is attributed to the role of water in enhancing grain growth. The very marked reduction in shear modulus for temperatures >1000°C is attributed to the widespread wetting of grain boundaries resulting from hydrofracturing and the maintenance of conditions of low differential pressure $P_d = P_c - P_f$, where P_f is the pore pressure. During staged cooling, accompanied by decreasing P_f and increasing P_d, a different microstructural regime is encountered in which the fluid is increasingly accommodated in arrays of partly-isolated grain-boundary pores. The more pronounced viscoelastic behaviour observed within this regime for the Pt-encapsulated specimen than for the dry specimen is tentatively attributed to enhanced grain-boundary sliding facilitated by the presence of interconnected pore fluid & lower grain-boundary viscosity. Future work will focus on the role of trace amounts of water associated with defects within the crystal structure of synthetic olivine.

References

[1] S. Karato, Mapping water content in the Earth's upper mantle, *The Subduction Factory*, AGU Monograph, 135, (2003).

[2] I. Jackson and M. S. Paterson, *Pure Appl. Geophys*. **141**, 445 (1993).

Diffuse X-ray Scattering from Optically Pure Ibuprofen

P.A. Altin[a] and D.J. Goossens[b]

[a] *Department of Physics, Australian National University, Canberra 0200, Australia.*
[b] *Research School of Chemistry, Australian National University, Canberra 0200, Australia.*

The crystal structure of optically pure Ibuprofen ('S+ibuprofen') has been studied through diffuse x-ray scattering. Data from a single crystal were compared with calculated patterns using a model crystal placed in thermal equilibrium using a Monte Carlo (MC) algorithm. We present some preliminary results from analysis and interpretation of the structured diffuse scattering.

1. Introduction

Diffuse scattering, the weak background between sharp Bragg peaks in an x-ray diffraction pattern, arises due to deviations from the ideal crystal lattice, often due to thermal motion. Correlations in these displacements, which reflect the flexibility and interactions of molecules in the lattice environment, affect the pattern of diffuse scattering observed from a sample [1]. Studying these interactions through diffuse scattering can provide insight into the conformational behaviour of polymorphic pharmaceuticals.

In this work, x-ray scattering data was collected at room temperature from crystals of S+ibuprofen. A model crystal was constructed based on the known average crystal structure and placed in thermal equilibrium using a MC simulation. Inter- and intra-molecular interactions were modelled by simple harmonic potentials with variable force constants. Computed scattering patterns were compared to the experimental data to isolate key features of the model.

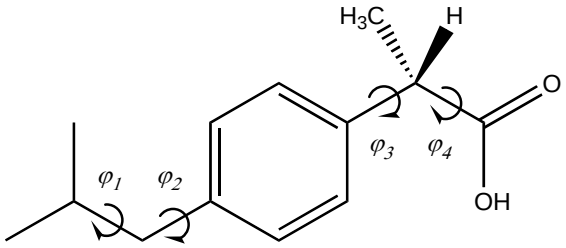

Fig. 1. S+ibuprofen. Rotation (modelled by torsional springs) is permitted about the four single bonds marked, giving four internal degrees of freedom φ_i.

2. Experimental

S+ibuprofen single crystals were grown by slow evaporation from n-hexane and by temperature change (40°C to 10°C at 5Kd^{-1}) in acetonitrile. Diffuse scattering data were collected using a mar345 image plate area detector and 17.5 keV (λ = 0.71069 Å) Mo Kα x-rays. Reciprocal space planes were extracted from the raw data and processed to remove artefacts [2]. Fig. 2 shows diffuse scattering in the *h*1*l*, *hk*0 and a 101 plane.

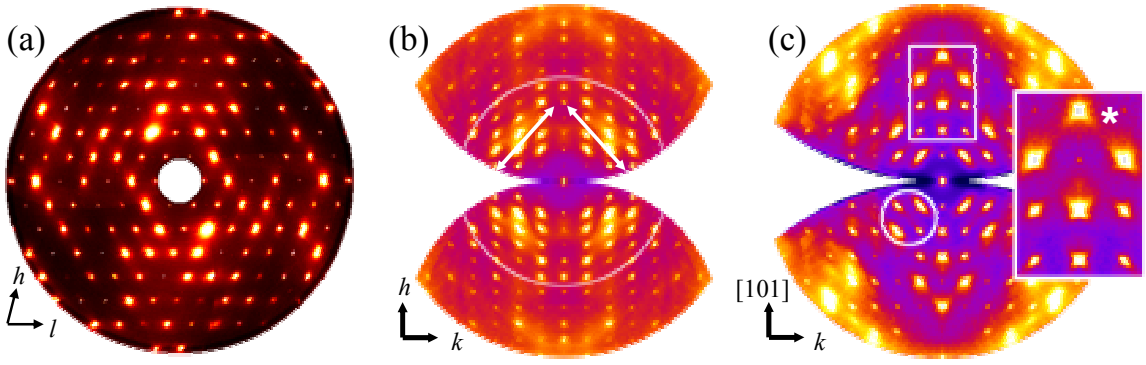

Fig. 2. Diffuse scattering in the (a) *h*1*l*, (b) *hk*0 and (c) 101 planes. The circle in (b) indicates the section of the plane calculated from the model (Fig. 4). False colour palettes have been applied.

3. The Model Crystal

A network of contact vectors describes the intermolecular interactions in the model crystal. Each contact is treated as an ideal spring. A harmonic energy is also associated with torsional rotation of the bonds marked in Fig. 1, giving:

$$E_{total} = E_{inter} + E_{intra} = \sum_{\substack{contact \\ vectors}} \kappa_i \left(d_i - d_{0i}\right)^2 + \sum_{molecules} \left(\sum_i \kappa_i^* \left(\Delta\varphi_i\right)^2 \right)$$

where κ and κ^* are the force constants, $(d - d_0)$ is the displacement of each contact from its equilibrium length, and $\Delta\varphi$ is the change in torsional angle. The lattice parameters applied were: a = 12.456(4) Å, b = 8.0362(11) Å, c = 13.533(3) Å and β = 112.86(2)° [3]. A Metropolis Monte Carlo algorithm was used to bring the model crystal into thermal equilibrium [4]. Diffraction patterns were then calculated from the correlated equilibrium structure. Bragg peaks were subtracted to make the diffuse scattering more apparent.

4. Results and Analysis

4.1 Isotropic intermolecular contacts:

A simple model with all intermolecular spring constants equal and no torsional rotation allowed reproduced the scattering in the *h*0*l* and *h*1*l* planes well (see Fig. 3). This suggests that correlations in these planes are isotropic as there seems to be no dominant interaction. However, this basic model failed to recreate key features of the *hk*0 plane, particularly the lengthening of diffuse spots along the diagonal (marked with arrows in Fig. 2).

4.2 Torsional rotation model:

This model was then adjusted to allow bond rotation. With the torsional spring constants k_i^* set to zero (such that $E_{intra} << E_{inter}$), the fit of the *h*0*l* and *h*1*l* planes to the experimental data was improved, and the expected stretching of diffuse spots in the *hk*0 plane (Fig. 4) was observed. The agreement of this calculation with the experimental data suggests that quite unhindered torsional rotation is important in the S+ibuprofen crystal, with significantly less energy in such motion than in the intermolecular interactions.

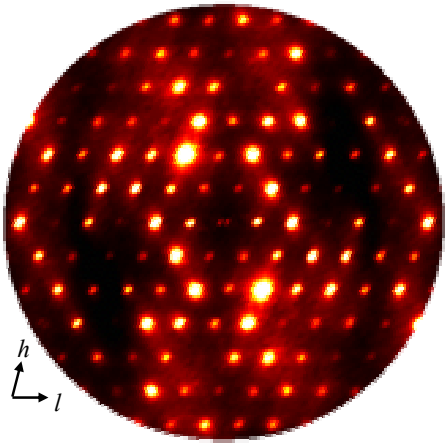

Fig. 3. Calculated diffuse scattering in the *h*1*l* plane with all spring constants equal. Compare with Fig. 2 (a).

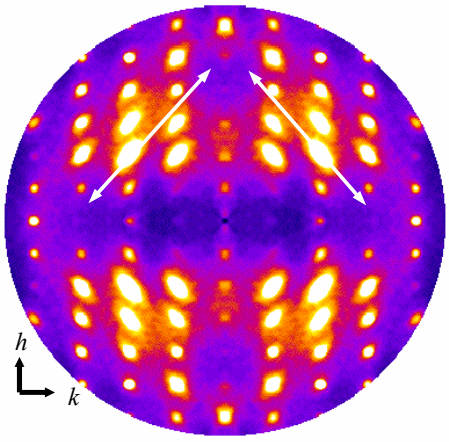

Fig. 4. Calculated diffuse scattering in the *hk*0 plane with torsional spring constants set to zero. Compare with the inner part of Fig. 3 (c).

4.3 Dimerising hydrogen bonding interaction:

It was expected that the strongest intermolecular interaction in the S+ibuprofen crystal would be the dimerising -COOH—HOOC- hydrogen bond, as recently found to be the case in the racemate [5]. Initial analysis of the experimental data appears to support this, with diffuse features stretched more in the 101 plane (Fig. 2c) where the direction of this interaction coincides with the molecular axis. This forms chains of molecules (Fig. 5) which collapse diffuse scattering into characteristic stretched lines. In addition, several box-shaped features are seen along the vertical axis (marked with an asterisk in Fig. 2c). These also suggest strong correlations at ~ 45° to the horizontal. A model with these H-bond contacts strengthened 100-fold (Fig. 6) reproduced the elongation and these box-shaped figures.

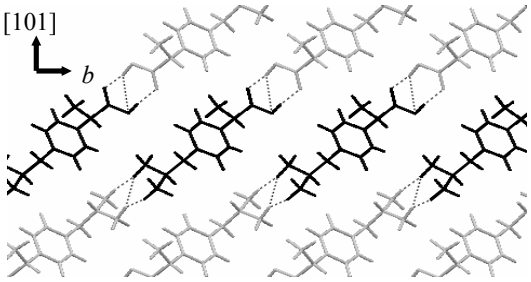

Fig. 5. A section of the crystal as seen along the [-101] direction, showing as dashed lines the dimerising hydrogen bonding interactions running at ~ 45° to the horizontal.

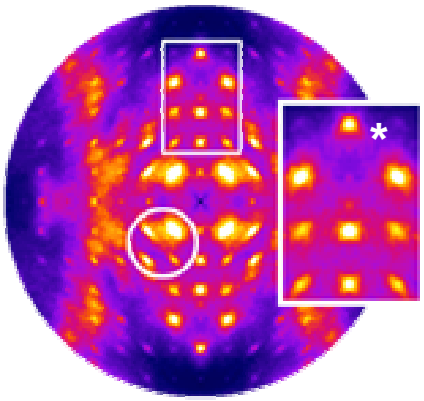

Fig. 6. Calculated diffuse scattering in the 101 plane with H-bond contacts strengthened by a factor of 100. Compare with Fig. 2(c).

Although the calculated pattern in this plane is not a precise reproduction of the diffuse scattering data, the presence of some corresponding attributes is evident. In particular, the scattering figures magnified in the inset in Fig. 6 successfully recreate the equivalent section of the experimental data (Fig. 2c) with good accuracy. The uppermost box-shaped spot marked with an asterisk (*) is manifestly wider at the bottom than at the top, both in the calculated pattern and in the data; and the surrounding spots display the expected profiles.

Acknowledgments

This work was carried out at the Research School of Chemistry at the Australian National University. The authors thank the Disordered Materials Group for sponsoring this work; and in particular Aidan Heerdegen, for help with the experimental work and in extracting and post-processing the data; and Richard Welberry, for assistance with the data collection.

References

[1] T.R. Welberry, *Diffuse X-ray Scattering and Models of Disorder* (Oxford University Press Inc., New York, 2004).
[2] T.R. Welberry, D.J. Goossens, A.P. Heerdegen and P.L. Lee, *Z. Kristallogr.* **220** 1052 (2005).
[3] L.K. Hansen, G.L. Perlovich and A. Bauer-Brandl, *Acta Cryst.* **E59** 1357 (2003).
[4] N. Metropolis, A.W. Rosenbluth, M.N. Rosenbluth, A.H. Teller and E.J. Teller, *Chem. Phys.* **21(6)** 1087 (1953).
[5] D.J. Goossens, A.P. Heerdegen, T.R. Welberry, and A.G. Beasley, unpublished work.

Characterization of nanometer-sized VO_2 nanoparticles prepared by an aqueous route

H. Bai[a,b] , M. Berkahn[a] and M.B. Cortie[a]

[a]*Institute for Nanoscale Technology, University of Technology Sydney, NSW 2007, Australia*
[b]*on leave from Nanjing University of Science and Technology, Nanjing, 210094, China*

We describe a convenient aqueous route to prepare VO_2, based on the reductive precipitation of vanadium dioxide VO_2 from a vanadate solution. The effect of the reaction conditions is systematically studied, and a protocol to optimize the production of VO_2 while minimizing the appearance of other compounds is presented. The products were characterized using calorimetry, X-ray diffraction and high-resolution scanning electron microscopy.

1. Introduction

Vanadium oxides have attracted attention because of their potential or actual applications as catalysts, chemical sensors, electrodes for lithium batteries, and as the active components of various electrical and optical devices[1, 2]. Vanadium dioxide (VO_2) is particularly interesting as some forms of it undergo a reversible metal/insulator phase transition at ~67ºC with a large attendant change in electrical and optical properties[3]. This has suggested its application as, for example, a 'smart' window coating, or in optical switches[2, 4]. VO_2 itself has at least six known polymorphs and some hydrated $VO_2.nH_2O$ compounds are also known[5, 6]; however it is the metastable monoclinic VO_2-B, tetragonal VO_2-R, and monoclinic VO_2-M_1 phases that are most relevant in the present context. VO_2-R is metallic and has the rutile structure, while VO_2-M_1 is a semi-conductor, with a band gap of about 0.6 eV[7]. The latter two polymorphs are related to one another by a reversible, displacive phase transformation at about 67ºC, with VO_2-R being stable above that temperature and VO_2-M_1 below it. There are several methods by which VO_2-M_1 or VO_2-R can be produced, including physical vapour deposition, ion implantation, chemical vapour deposition, sol-gel processing and lyphilization of suitable precursor solutions. Commonly, however, VO_2-B is first prepared by whatever means and then it is converted to VO_2-R by heat treatment in an inert environment and at a temperature in excess of 330˚C. We sought a method suitable for producing VO_2 in relatively large quantities. Our protocol invokes the reductive-precipitation of $VO_2.nH_2O$ from a vanadate solution, and is based on a process apparently first disclosed by two groups in 1998[1, 8]. Calcination of the $VO_2.nH_2O$ converts it into VO_2-R. We use ammonium metavanadate (NH_4VO_3) solution as our source of V, and KBH_4 as reductant.

2. Experimental

NH_4VO_3 was purchased from Ajax Chemicals Ltd, Sydney, Australia. KBH_4 was purchased from Sigma Chemical Co., and HCl (37%) was obtained from Labscan Asia Co., Ltd.. All reagents were used without further purification. The KBH_4 solution was freshly produced, as needed, by dissolving the compound in ice-cold MilliQ water. The temperature must be kept low to prevent hydrolysis of borohydride ion. Concentrated HCl was first added dropwise into between 10 to 50 ml of the NH_4VO_3 solution to adjust its pH to a selected value between 4.0 and 6.5. The reducing power of KBH_4 increases with the decreasing of pH value of the medium suggesting that it might be more effective at the lower end of the pH range[1].

The reduction reaction was then carried out at the desired pH by slowly adding the KBH_4 solution while continuing the dropwise additions of HCl and simultaneously stirring. At the end of the reduction reaction, the brown-black precipitate of $VO_2.nH_2O$ was collected by filtration, washed several times with a mixture of water and methanol, and dried at about 90 ˚C in an air oven. The dry solid is amorphous or at best nanocrystalline at this stage, in agreement with product produced in other wet chemical reductive schemes, e.g.[1]. This phase, in turn, can be converted to VO_2-R by heating at temperatures greater than ~330˚C in an inert environment[1, 9] In the present work we used an environment of pure argon or nitrogen. Finally, on reverting to room temperature the VO_2-R transformed to VO_2-M_1 by the metal-to-insulator transition.

The as-synthesized samples were characterised by X-ray diffraction (XRD, Siemens D5000 Diffractometer) with Cu Kα radiation (λ=0.15406 nm). Scanning electron microscopy (SEM) images were taken with a Zeiss Supra 55VP SEM. A differential scanning calorimeter (DSC 2920, TA Instruments Inc., U.S.A.) was employed to test the phase transformation. X-ray diffraction patterns were calculated from the published lattice data using the program Crystallographica (produced by Oxford Cryosystems Ltd, of the United Kingdom).

3. Results

After systematic investigation, we found that VO_2-M_1 could be reliably produced if the pH of the reaction was held at about 4.2, the ratio of KBH_4 to NH_4VO_3 was 5, the temperature of the reaction at about 20 to 25˚C, and calcination was carried out at 600˚C.

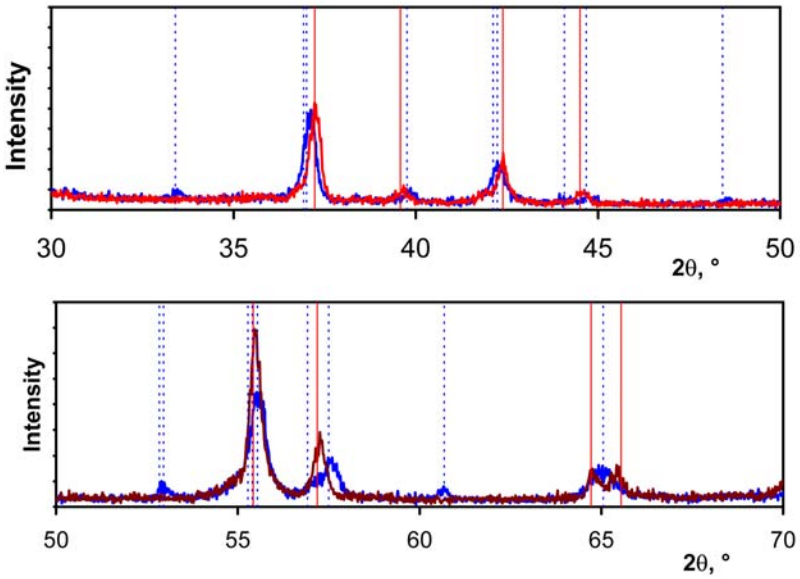

Fig. 1 XRD patterns of VO_2-M_1 (blue) at room temperature and VO_2-R (red) at ~80˚C, also showing standard peak positions (coloured lines) for each phase.

Fig. 1 shows the X-ray diffraction patterns for such 'optimum' material, which was converted to VO_2-R (JCPDS 73-2362) by heat treatment and cycled between VO_2-M_1 (JCPDS 44-0252) and VO_2-R on a hot stage. Under the optimum conditions the resulting material is almost pure, and has an XRD pattern nearly identical to the standards. The remaining small peaks in this case match the pattern of V_6O_{13}, an oxide of mixed valence. Fig. 2 shows that the diameter of the VO_2-M_1 particles is about 100 nm, which is about twice the diameter of the particles of precursor material, as dried in air oven at 85˚C for 1 h. The result demonstrates that crystallization of the VO_2-R is accompanied by particle coarsening. In Fig. 3 we examine the metal-insulator transition in more detail. In this case the VO_2-M_1 was heated from room temperature to 120 ˚C at 3˚C/min under a flowing air atmosphere, and then back to

room temperature. The insulator-to-metal transition occurred at 66˚C, and the metal-to-insulator transition at 61˚C.

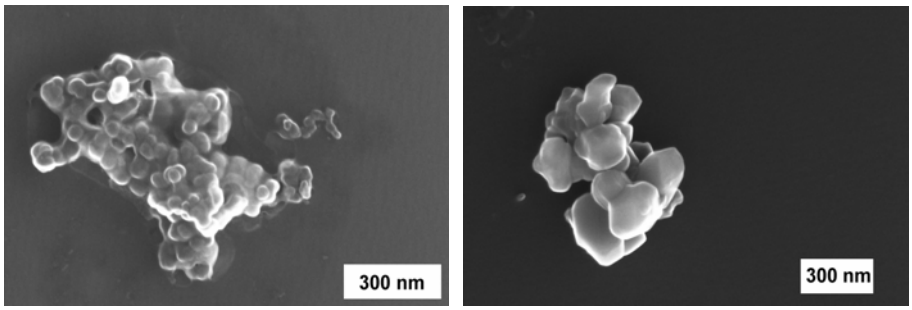

(a) (b)

Fig.2 SEM photos of VO_2 nano-particles produced as described in the text. (a) Dried in air oven at 85˚C for 1h. (b) Dried in tube oven at 600˚C under flow of argon for 20h.

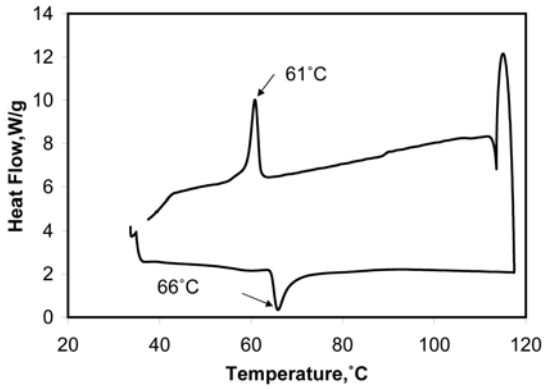

Fig. 3 DSC curve showing the reversible VO_2-$M_1 \leftrightarrow VO_2$-R phase transformation in the present material. There is a hysteresis of 5˚C in the reaction.

Conclusions

Nano-crystalline VO_2-M_1 was successfully synthesized by a convenient process involving aqueous reductive-precipitation at room temperature followed by calcination. If the pH and ratio of KBH_4 to NH_4VO_3 during the precipitation reaction are both kept in the range 4~5, and if the subsequent annealing temperature is 600˚C, then the synthesized nano-crystals of VO_2-M_1 are about 100 nm in size. The transition temperature of the material produced was in the range 61 to 66˚C.

References

[1] C. F. Tsang, J. Kim and A. Manthiram, *J. Mater. Chem.* **8**, 425 (1998).
[2] M. Soltani, M. Chaker, E. Haddad and R. Kruzelesky, *Measurement Science and Technology* **17**, 1052 (2006).
[3] F.J. Morin, *Phys. Rev. Lett* **3**, 34 (1959).
[4] T.D. Manning and I.P. Parkin, *Journal of Materials Chemistry* **14**, 2554 (2004).
[5] C. Leroux and G. Nihoul, *Physical Rev. B* **57**, 5111 (1998).
[6] Z. Gui, R. Fan, X.H. Chen and Y.C. Wu, *J. Solid State Chemistry* **157**, 250 (2001).
[7] S. Biermann, A. Poteryaev, A.I. Lichtenstein and A. Georges, *Phys. Rev. Lett* **94**, 026404 (2005).
[8] V. Manivannan and J.B. Goodenough, *Materials Research Bulletin* **33**, 1353–1357 (1998).
[9] Z. Gui, R. Fan, W. Mo, X. Chen, L. Yang, S. Zhang, Y. Hu, Z. Wang and W. Fan, *Chem. Mater.* **14**, 5053 (2002).

Grain-Size Sensitive Viscoelastic Relaxation of High-Purity MgO

Auke Barnhoorn, Ian Jackson and John D. Fitz Gerald

Research School of Earth Sciences, The Australian National University, Canberra, ACT 0200 Australia

High-temperature mechanical spectroscopy experiments have been performed on newly prepared polycrystalline MgO samples with average grain sizes of 3, 9 and 100 μm. Viscoelastic relaxation is strongly grain size dependent above temperatures of 800°C with a frequency and temperature-dependent 'background' consisting of a broad anelastic relaxation band intensified by the onset of viscous deformation. Data analysis using a master variable approach suggests that grain boundary sliding processes dominate viscoelastic relaxation.

1. Introduction

The high-temperature breakdown of strictly elastic behaviour in fine-grained materials is usually attributed to grain-boundary sliding facilitated by the low effective viscosity of the thin grain-boundary region or to diffusional mechanisms. Both grain boundary sliding and diffusion are grain size dependent deformation mechanisms. This study aims to determine which viscoelastic relaxation mechanism is responsible for the viscoelastic relaxation in high-purity ceramic MgO material. The new data will ultimately contribute to constructing improved micro-mechanical models for grain boundary sliding [1,2].

2. Sample preparation

For fabrication of the samples, high-purity (> 99.99 wt.%) MgO nanopowder with a grain size of 45-60 nm (supplied by Ube Materials Industries Ltd.) has been used. Samples with low porosity (ϕ < 1%) and controlled grain sizes have been obtained by a multi-stage fabrication process: (1) Cold isostatic pressing at 200 MPa for 0.5 hour to yield samples of ~50% porosity; (2) Pressureless sintering at 900-1100°C for 2 hours in an N_2-rich environment to evaporate residual CO_2 and H_2O followed by slow cooling at 2 °C/min to prevent sample cracking (ϕ~40%); (3) Hot-isostatic pressing of the sample in a steel jacket in a gas-medium apparatus at 300 MPa argon confining pressure at elevated temperatures. For the finest grained sample (1-3 μm). Hot-pressing for 24 hours at 1100°C resulted in minor further densification of the sample (ϕ ~1%) and minor grain growth to an average grain size of 1-3 μm. The second sample has been made using two-stage hot-pressing; first at 1100°C for 24 hours for densification followed by 1300 °C for 24 hours to allow grain growth to 5 μm. The third sample had to be hot-isostatically pressed at a confining pressure of 30 MPa and a temperature of 1600°C for 2 hours in facilities at Okayama University in Japan to obtain a sample with a much larger grain size of 100 μm.

Torsional forced-oscillation experiments[3] were conducted at 200 MPa confining pressure over the temperature range 20-1300°C. Sinusoidally varying stresses were applied at 10 different periods between 1s and 1000s at torque amplitudes equivalent to maximum shear stresses of 0.3 MPa, resulting in maximum shear strains of 3.10^{-5} at the highest temperature. Before performing routine torsional forced-oscillation measurements, the assemblies were thoroughly annealed at the highest temperature and the mechanical behaviour was monitored. Small changes in shear modulus G and strain-energy dissipation Q^{-1} with time at the

beginning of the experiment reflect minor microstructural changes (grain size increase from 1 to 3 and 5 to 9 µm, Fig.1). After stabilization of the microstructure, torsional forced-oscillation experiments were performed over the complete range of oscillation periods in temperature steps of 50°C, starting at the highest temperature. Mechanical data in the form of shear modulus and dissipation were determined for each oscillation period at each temperature.

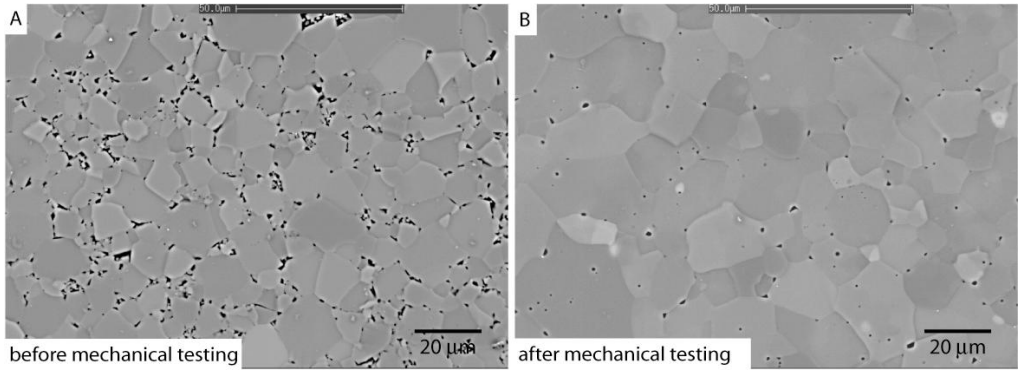

Fig. 1. Backscattered electron image of (a) hot-isostatically pressed sample (total 48 hours at high-temperature) and (b) the same sample after further annealing and mechanical testing involving several days at temperatures > 1000°C resulting in slow continuous grain growth and reduction of porosity.

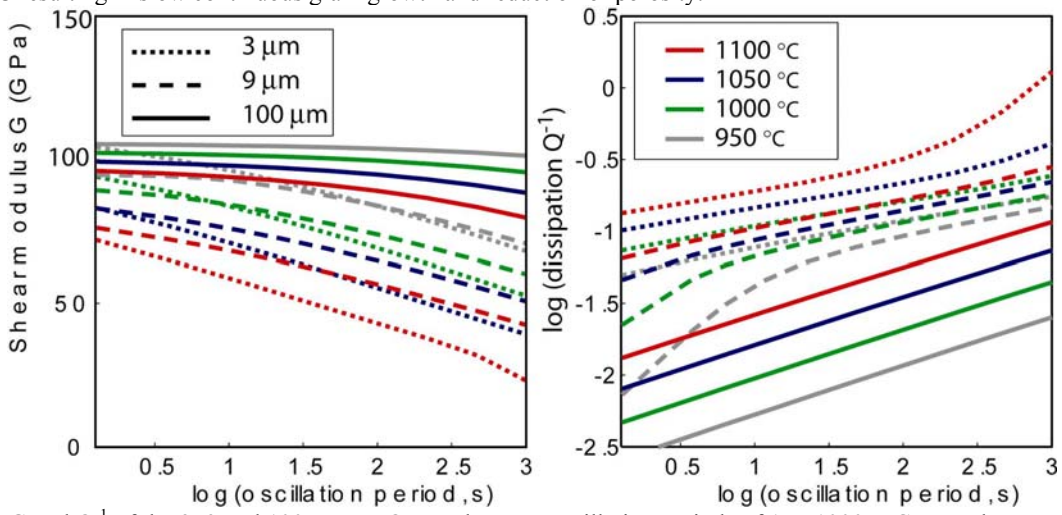

Fig. 2: G and Q^{-1} of the 3, 9 and 100 µm MgO samples over oscillation periods of 1 to 1000 s. Curves shown are least-square fits to an extended Burgers model[4,5]. Line colour and pattern indicate temperature and grain size, respectively, in both diagrams.

3. Results

All three MgO samples with different grain sizes deform essentially elastically at temperatures ≤800°C. At higher temperatures, viscoelastic relaxation occurs with the strongest degree of viscoelastic deformation at the highest temperature, longest oscillation period and smallest grain size (Fig. 2). Maximum reduction in G between 1 and 1000 s at 1300°C is 70%. The systematic monotonic variations in G and Q^{-1} exclude the presence of any localised dissipation peak of significant height on top of the frequency-dependent dissipation background. G and Q^{-1} data for each individual sample were modelled using an extended Burgers model[4,5] describing the full viscoelastic relaxation of MgO resulting in generally small misfit of the experimental data.

Analyses of the Q^{-1} data only using a master variable approach[6] $X \sim \omega d^m \exp(E/RT)$, where E and R are the activation energy and the gas constant. This approach shows that the collapse of all three datasets is best when a linear grain size dependence (m=1) is included in

the approach. When using on optimal activation energy of 330 kJ/mol, both individual datasets and combined datasets collapse on a linear trend. A grain size sensitivity of 3 (m = 3) does not result in a good collapse on a linear trend irrespective of the value for *E*. Only individual datasets collapse on a linear trend. This indicates that the dissipation data of MgO is best described by a grain size dependence of 1, meaning that relaxation mechanisms with linear grain size dependence dominate over relaxation mechanisms with a grain size dependence of 3. We therefore conclude that grain boundary sliding (m=1) dominates over diffusion processes (m=3) in high-purity MgO[1,7].

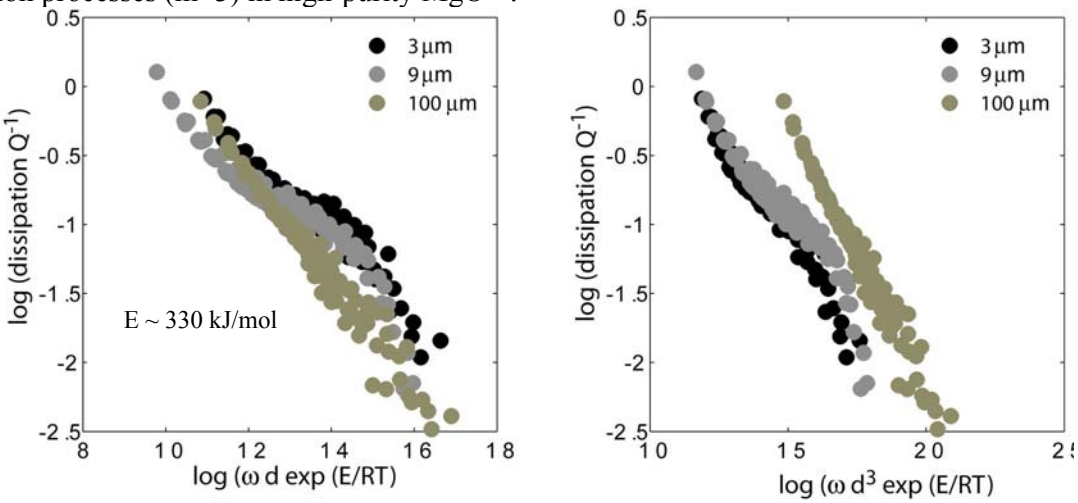

Fig. 3. Master variable approach of the dissipation data[6] $X \sim \omega d^m \exp(E/RT)$, where m=1,3. Collapse of the data with m=1 is narrower than for m=3, indicating grain boundary sliding mechanisms (m=1) dominate over diffusion mechanisms (m=3).

4. Conclusions

- Systematic grain size dependence of viscoelastic relaxation in MgO.
- Grain boundary sliding processes dominate over diffusion processes in high-purity MgO.

Acknowledgments

Akiro Kishimoto (Okayama University) is acknowledged for the high-temperature hot-isostatic pressing of the largest grain size sample. This work was supported by Australian Research Council grant DP0450929.

References

[1] R. Raj and M. F. Ashby, *Metal. Trans.* **2** 1113 (1971).
[2] R. Raj, *Metal. Trans.* **A 6A** 1499 (1975).
[3] I. Jackson and M. S. Paterson, *Pure Appl. Geoph.* **141** 445 (1993).
[4] U.H. Faul and I. Jackson, *Earth Planet. Sci. Lett.* **234** 119 (2005).
[5] I. Jackson, in *Advances in high-pressure technology for geophysical applications*, eds J. Chen, Y. Wang, T.S. Duffy, G. Shen and L.F. Dobrzhinetskaya , (Elsevier, 2005).
[6] I. Jackson, U.H. Faul, J.D. Fitz Gerald and B.H. Tan, *J. Geophys. Res.* **109** B06201 doi:10.129/2003JB002406 (2004).
[7] J.-P. Poirier, *Creep of crystals: High-temperature deformation processes in metals, ceramics and minerals*, (Cambridge University Press, 1985).

Development of a Simulation Board Game Based on the Physical Principles of Superconductivity and Magnetism for use as a Teaching Aid

R. Barry and S. Hodgman

Physics Department, The Australian National University, Canberra, 0200, Australia.

We have designed a tactical simulation board game based on the physical principles of superconductivity and magnetism. This could be used as a teaching aid to engage the interest of students, and help them gain a qualitative understanding of physical concepts. Preliminary play testing with undergraduate students indicates that the game achieves this result.

1. Introduction

Students generally learn material better when they engage actively with the subject matter and if their interest is stimulated [1,2]. This can be especially useful in helping students gain an intuitive understanding of many physics concepts [3]. To assist in developing this qualitative comprehension, a tactical simulation board game based on the principles of superconductivity and magnetism has been developed. This could be used as a teaching aid to help motivate students and assist in their understanding of these physics concepts. The Vortex! Game was developed as an assignment submission for the 3rd year condensed matter physics course, PHYS3032, at the ANU in 2006.

2. Game Mechanics

The game was designed in a science fiction setting, where the players control futuristic spaceships trying to destroy each other. The setting and goal were designed to appeal to physics students, thus adding an extra element of motivation. Elements of magnetism and superconductivity are incorporated in the way the ships move. The spaceships are made of magnets so that they interact with the magnetic terrain. The terrain over which the ships move consists of a hexagonal grid of different types of material: ferromagnetic, superconducting (type II) and non-magnetic (Fig. 1). For example, ferromagnetic terrain is represented by orange hexes with a domain arrow that indicates the direction of the horizontal component of the local magnetic field. Hence if ships move in the same direction as the field vector they will move further (lower energy cost) than if they are moving in the opposite direction.

Players are also able to modify the terrain by firing missiles at the terrain. For example, heating a superconducting or ferromagnetic hex above the critical or Curie temperatures respectively, will cause them to lose their magnetic properties for some time. The direction of the ferromagnetic domain in a hex can also be changed, which affects the domains in the neighbouring hexes. Another major terrain modification occurs when a strong magnetic field is introduced into one of the type II superconductor hexes. As the superconductor works to exclude the magnetic field, it undergoes a transition from the Meissner state to a vortex state, characterised by circular vortices of large currents. The vortex lattice is hexagonal, which fits very well with the hex map used to represent terrain in the game, which is partially why the hex map was used.

The game rules are deliberately designed to be simple and accessible, while still incorporating a substantial amount of correct physical modeling of magnetic behaviour.

It should also be noted that similar games designed around numerous other physical theories are also possible. In this respect, Vortex! can be seen as an example of how the abstracting of a physical theory into qualitatively accurate game mechanics can be achieved. The platform on which such a game is designed may also vary. The obvious alternative format is a computer. The main advantage of a computer application over a board game is that the relevant physics may be expressed quantitatively and in real-time due to the available processing power. The board game format, however, has a number of other advantages as discussed below.

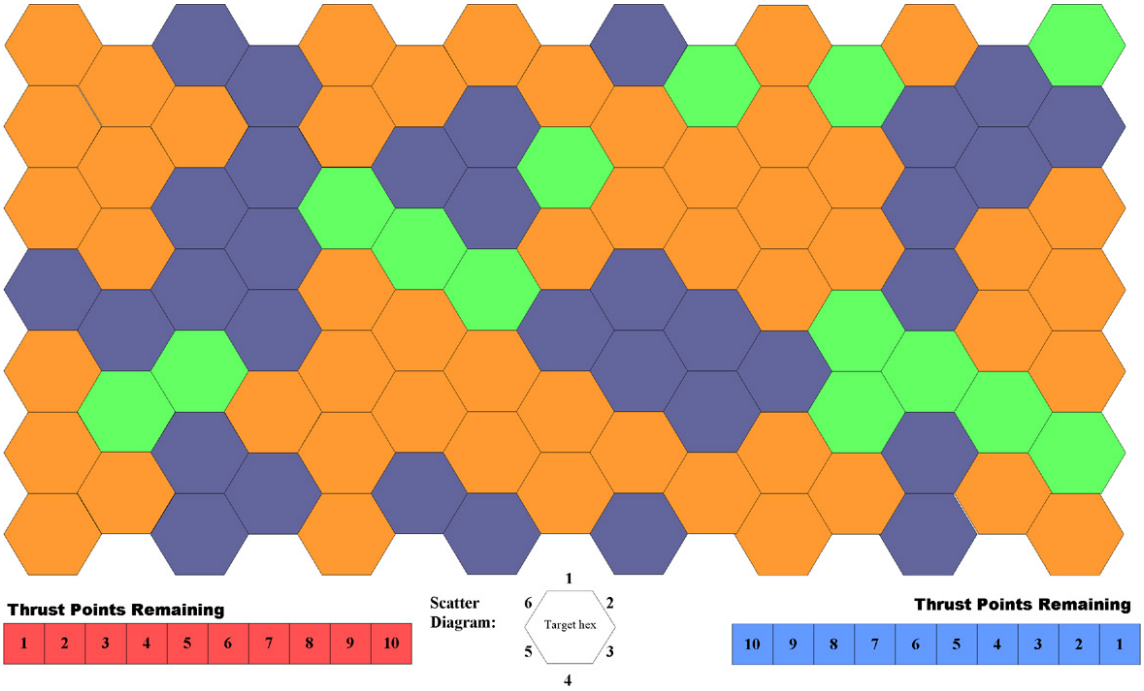

Fig. 1. The board used in the game showing the hex grid.

3. Educational Rationale

In order to aid in the development of an intuitive understanding of a physical theory, which due to its nature is usually a type of abstract mathematical construction, a tool is often beneficial that allows the student to directly manipulate the important properties of the theory while avoiding any lengthy calculations.

The Vortex! board game is such a tool that allows players to develop their ideas of magnetism and energy conservation. This is achieved by abstracting the involved physical principles into game mechanics such that they are qualitatively but not completely quantitatively accurate. The format for such a tool may vary as well – in this case a board game was chosen, but other platforms, such as computer applications, may also be used. An advantage of a computer game implementation is that the relevant physics may be expressed quantitatively and in real-time due to the available processing power. A board game implementation, however, has a number of other advantages. These include appealing to a broader group of students, including those who are not computer game players, as well as it being more social and consequently requiring personal interaction, thus encouraging co-operative learning. In addition, unlike a computer game, a board game requires no additional software or hardware other than what comes in the game box, thus making it more manageable in a classroom environment. The social aspect of the game is of particular interest and is one of its major advantages over the computer game format. In testing the

game, it drew the interest and participation of students and academics, some of who would not have participated in a computer game.

As a second educational benefit, as well as providing the players with a basic insight into the physical principles, it is hoped that it will do so in a manner that is substantially more engaging then a list of textbook questions. By providing students with this prospect of interacting with familiar subject matter from such a different perspective they will be motivated to engage with the material - even if it is only out of a sense of curiosity rather then a genuine interest in the game itself [2].

The game is not intended to replace traditional problem sets that provide quantitative understanding of the physics, but is instead designed to supplement them by providing an engaging and interactive introduction to magnetism. Initial class testing in 2006 indicates that students do find the game engaging. Further class testing in 2007 will investigate student learning outcomes from use of the game in a third year CMP course at the ANU.

4. Conclusion

The game successfully abstracts the relevant physical principles of magnetism such that they were playable in a game format while remaining qualitatively accurate.

Students were intrigued by the prospect of interacting with physical principles from a new perspective and were thus enthusiastic to play the game.

As a teaching aid, the game complements traditional quantitative learning tools in that it allows for students to become familiar with the central concepts of the theory while avoiding lengthy calculations.

Acknowledgments

The authors would like to thank Kate Wilson and Darren Goossens for their encouragement and support throughout the game design and manufacturing. We also thank all the 2006 PHYS 3032 students who assisted in playtesting for their positive feedback.

References

[1] R. Knight, *Five Easy Lessons: Strategies for successful physics teaching.* (Addison Wesley, 2002).
[2] P. Ramsden, *Learning to Teach in Higher Education* (Taylor and Francis, 2003).
[3] R. Hake, *Am. J. Phys.* **66,** 1 (1998).

An Investigation of the Structural Dynamics in the Fast Ionic Conductor $Cu_{2-\delta}Se$ using Neutron Scattering

S.A. Danilkin[a], N.N. Bickulova[b]

[a]*Bragg Institute, ANSTO, NSW 2234, Australia*
[b] *Sterlitamak University, Sterlitamak, Russia*

A neutron scattering study with energy analysis was performed on polycrystalline $Cu_{2-\delta}Se$ samples. Experiments show that the diffuse scattering in the super-ionic α-$Cu_{2-\delta}Se$ phase is mainly inelastic and most probably comes from correlated thermal displacements of the ions.

1. Introduction

The compound $Cu_{2-\delta}Se$ ($0 \leq \delta \leq 0.25$) is a mixed ionic-electronic conductor. For stoichiometric Cu_2Se the phase transition temperature to the super-ionic α - phase is 414K, but transition temperature depends on the composition and decreases with increasing values for δ. At room temperature the super-ionic α-phase exists over the composition range from δ = 0.15 to 0.25 [1].

The structure of the α-phase is reported as cubic with Se atoms in fcc positions and Cu ions randomly distributed over interstitial sites [2]. The low-temperature β-$Cu_{2-\delta}Se$ phase is a triclinic fluorite-based superstructure with vacant Cu sites forming a $\sqrt{3} \times \sqrt{3}$ network in the [111] plane [3]. The vacant Cu layers stack at every fourth metal layer along the [111] axis.

Characteristic of super-ionic conductors is the presence of strong diffuse scattering. The copper selenide is no exception showing diffuse scattering features in neutron diffraction patterns of polycrystalline and single crystal samples [4, 5]. Diffuse scattering originates from static disorder and/or correlated dynamic displacement. In a conventional diffraction experiment the diffuse background contains both these components. In order to separate static and dynamical contributions in Cu_2Se Sakuma *et al.* [4] used a triple-axis spectrometer in $\Delta E \approx 0$ mode with the analyser crystal adjusted to reflect elastically scattered neutrons from the sample. The contribution of inelastic scattering processes was then estimated from the data measured with the analyser crystal and without it, in conventional double-crystal mode. The experiment showed that the inelastic component in the diffuse background was small, probably because of an insufficient energy resolution of the spectrometer [4].

In order to clarify the role of static disorder versus low-energy phonons in the diffuse scattering we performed energy resolved neutron scattering measurements at higher resolution. The paper presents the results of these neutron diffraction measurements taken in $\Delta E \approx 0$ mode together with conventional diffraction data from the super-ionic α - phase ($Cu_{1.98}Se$ at 435K and $Cu_{1.75}Se$ at 300K) and the ordered β - $Cu_{1.98}Se$ at 300K.

2. Sample preparation

The samples were prepared by solid-state reaction of high purity Cu and Se powders in evacuated ($p < 10^{-5}$ mbar) sealed quartz ampoules. The mixed components were heated up to 720K for about 100 hours with subsequent annealing for 48 hours at 420-520K. After slow cooling to room temperature the product was ground and then homogenised under vacuum for 100 hours at 670 K.

Neutron diffraction patterns of the samples were measured with the E1 triple-axis spectrometer (HMI, Berlin) using a PG monochromator and analyser at a wavelength of

2.355 Å [6]. The collimation of the spectrometer was 40′-40′-40′-80′ with a resolution at the elastic line of $\Delta E \approx 0.7$ meV. The cylindrical samples of $Cu_{1.75}Se$ and $Cu_{1.98}Se$, with masses of 4.8 and 8.5 g respectively, were measured in a standard cryofurnace at room and elevated temperatures.

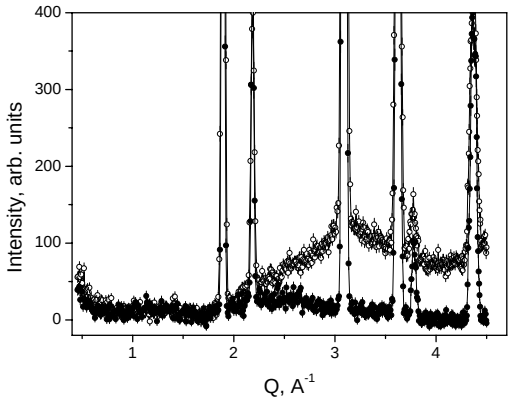

Fig. 1. Diffraction pattern of $Cu_{1.75}Se$ in the α - phase at 300K.

∘ – double–axis scan, • – triple–axis ($\Delta E \approx 0$) scan.

Figures 1 and 2 show diffraction patterns of the $Cu_{1.75}Se$ and $Cu_{1.98}Se$. The data were taken with and without the analyser crystal in otherwise identical experimental conditions. After subtraction of the flat background, the spectra of $Cu_{1.98}Se$ and $Cu_{1.75}Se$ were normalised to the sample mass and counts of the incident neutron beam monitor. Spectra measured with and without the analyser crystal, were normalised to the area intensity of Bragg reflections.

3. Results and Discussion

In α - $Cu_{1.75}Se$ the diffraction peaks correspond to an fcc structure (Fig. 1) with the lattice parameter $\boldsymbol{a} = 5.75$ Å in agreement with data of Tonejc [7]. The diffraction pattern of α - $Cu_{1.98}Se$ at 435K also corresponds to the cubic phase, although the intensities of the (200) and (222) reflections ($Q \approx 2.2$ and 3.8 $Å^{-1}$ respectively) are lower. In addition to the peaks from the fcc structure, α - $Cu_{1.98}Se$ at 435K also has two small additional maxima at $Q \approx 2.6$ and 4.2 $Å^{-1}$ which are probably related to ordering of the Cu atoms even at temperature slightly above the reported phase transition. Note that our diffraction experiments with a single crystal of $Cu_{1.85}Se$ performed at ambient temperature - thus according to literature [1, 2] in "disordered" α - phase, in fact show the presence of superstructure reflections at the $\boldsymbol{G} \pm 1/2 \langle 111 \rangle$ and $\boldsymbol{G} \pm 1/3 \langle 220 \rangle$ positions of reciprocal space [5].

Along with these Bragg peaks, the diffraction pattern of the α - phase taken in the conventional two-axis geometry has a broad maximum related to diffuse scattering centred at $Q \approx 3$ $Å^{-1}$, close to the (220) Bragg reflection (Fig. 1 and 2(a)). The observed diffuse peak resembles the spectrum of α - Cu_2Se at 470 K measured in two-axis geometry in paper [4]. Contrary to earlier findings [4], our measurements show a strong suppression of this diffuse component in the spectrum measured with the analyser crystal. On the other hand, the diffraction pattern of the non super-ionic β - phase (Fig. 2b) shows only minor differences between spectra measured with and without the analyser crystal (Fig. 2b). This clearly indicates a strong contribution to the diffuse scattering in the super-ionic phase from inelastic scattering.

As mentioned above, in experiment [4] the spectrum taken in $\Delta E \approx 0$ mode was very similar to the diffraction pattern measured by the conventional double - axis technique in the region of the first diffuse maxima at $Q \approx 3$ $Å^{-1}$. This can occur if the contribution from the low-energy phonons and the quasielastic scattering are not filtered off by analyser crystal due to the limited energy resolution of the spectrometer. Such phonons with energies about 2 - 4 meV were observed in the phonon frequency distribution of $Cu_{2-\delta}Se$ compounds and in phonon dispersion curves. The density of states of low- energy phonons is relatively high

because the dispersion curves change slope at wavevectors of q>0.2-0.4 and acoustic branches become nearly flat having an energy of about 4 meV [8].

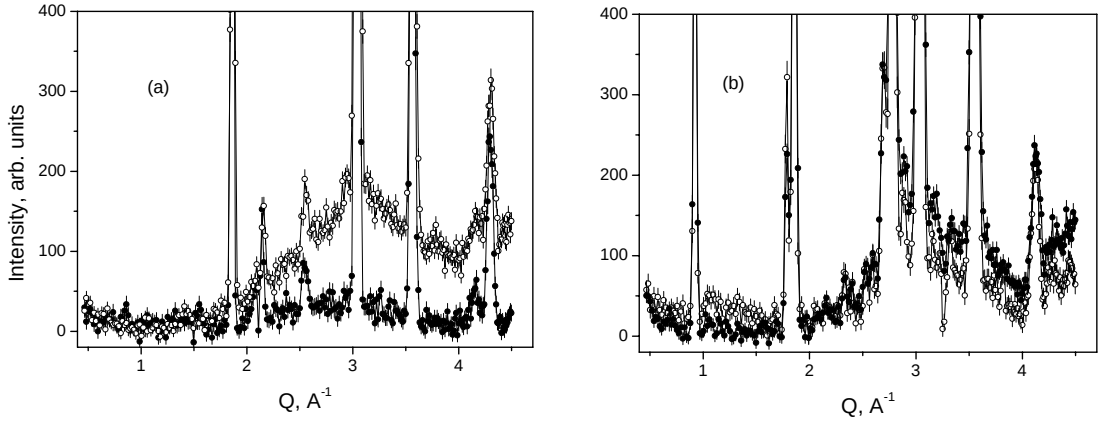

Fig. 2. Diffraction patterns of $Cu_{1.98}Se$ in the α - phase at 435K (a) and the β - phase at 300K (b).

○ – double–axis scan, ● – triple–axis ($\Delta E \approx 0$) scan.

The high spectral density of low-energy phonons, they can play a role in the transport of Cu ions. A calculation of diffuse scattering performed in paper [4] shows strong correlations between the thermal displacement of Se and Cu atoms at short distances. Such correlations are probably responsible for the strong dampening of acoustic phonons observed in α - $Cu_{1.85}Se$ at $q/q_m \geq 0.4$ [8] and indicate a coupling of low-energy phonon modes with displacement of mobile ions.

Acknowledgments

The support of HMI Berlin in providing the neutron facilities used in this work is acknowledged.

References

[1] N.H. Abrikosov, V.F. Bankina, M.A. Korzhuev, G.K. Demski and O.A. Teplov, *Sov. Phys. - Solid State* **25,** 1678 (1983).
[2] M. Oliveria, R.K. McMullan and B.J. Wuensch, *Solid State Ionics*, **28-30,** 1332 (1988).
[3] S. Kashida and J. Akai, *J. Phys. C.: Solid State Physics* **21,** 5329 (1988).
[4] T. Sakuma, T. Aoyama, H. Takahashi, Y. Shimoto and Y. Morii, *Physica B* **213-214,** 399 (1995).
[5] S. Danilkin, Phase transformations in $Cu_{2-\delta}Se$, BeNSC (Experimental Reports 2001, HMI Berlin), p 96.
[6] Neutron-Scattering Instrumentation at the Research Reactor BER II Berlin Neutron Scattering Center (BENSC, March 2001), p 6.
[7] A. Tonejc, *J. Mater. Sci*. **15,** 3090 (1980).
[8] S.A. Danilkin, A.N. Skomorokhov, A. Hoser, H. Fuess, V. Rajevac and N.N. Bickulova, *J. Alloys and Compounds* **361,** 57 (2003).

The Partition of Stresses in Al-Si-based Metal-Matrix Composites

T.R. Finlayson[a], J.R. Griffiths[b], D.M. Viano[b], M.E. Fitzpatrick[c], E.C. Oliver[d] and Q.G. Wang[e]

[a] *School of Physics, The University of Melbourne, Parkville, Victoria. 3010*
[b] *CSIRO Manufacturing & Materials Technology, Pullenvale, Queensland. 4069*
[c] *The Open University, Milton Keynes, MK7 6AA, U.K.*
[d] *CCLRC Rutherford Appleton Laboratory, Didcot, OX11 0QX, U.K.*
[e] *General Motors, Powertrain Materials Engineering, Pontiac, MI 48340-2920, U.S.A.*

Neutron diffraction methods have been used to measure the strains (and hence stresses) in the eutectic Si particles and the Al matrix of an Al-7Si-0.4Mg casting, as functions of the applied tensile strain, Three components of stress have been identified: (i) the thermal misfit stress; (ii) the elastic misfit stress; and (iii) the plasticity misfit stress.

1. Introduction

Al-7Si-0.4Mg is a widely used casting alloy. The microstructure, in our case, (Fig. 1) comprises (i) dendrite colonies or grains with a diameter of ~0.8 mm, (ii) Al dendrites with secondary dendrite arm spacings (SDASs) ranging from 20μm to 70 μm and (iii) a eutectic of micron-sized Si particles and Al. During tensile straining the Si particles cleave, the number of broken particles increasing with strain until complete fracture of the alloy occurs at between 3% and 12% strain [1]. The ductility increases with decreasing SDAS.

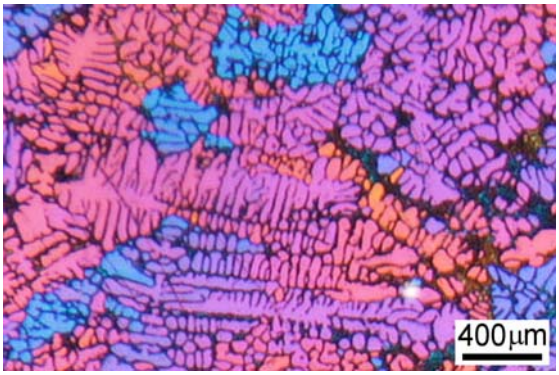

1a

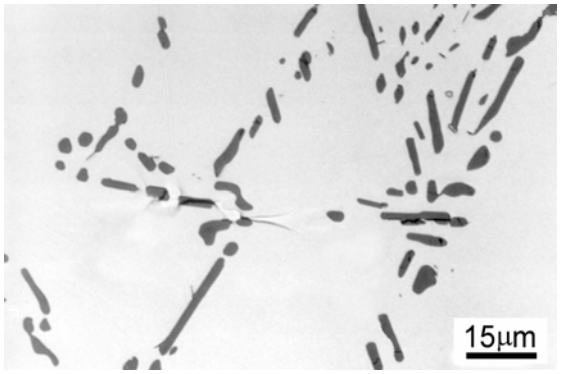

1b

Fig. 1: Microstructure of the casting. (1a) is photographed under polarized light in which individual colonies show as different colours; (1b) shows arrays of Si particles between dendrite arms.

Controversy exists concerning (a) the fracture strength of the Si particles [2,3] and (b) how they contribute to the yield stress and work-hardening rate of the alloy [4,5]. These controversies centre on estimates of the partitioning of stress between the Al matrix and the Si particles, on which there is almost no reliable experimental information.

The aim of this research is to provide such information.

2. Experimental details

Plates (140 x 160 x 25 mm) of nominal composition (wt%) Al-6.6Si-0.4Mg were sand-cast in moulds having a large chill at one end to produce a range of SDASs from 20 μm at the chill end to 70 μm at the other end. Slices were cut from either end of the plates and solution

heat-treated at 540°C for 6 hours followed by a cold water quench (condition T4). A second microstructural condition (T6) involved aging for 6 hours at 170°C. Tensile specimens with a parallel gauge length of 20 mm and a diameter of 8 mm were then machined from the slices.

In-situ neutron diffraction lattice strain measurements were made during tensile testing using the ENGIN-X instrument at the ISIS pulsed source. The instrument has two fixed-angle detector banks centered on scattering angles of ±90°. The detectors measure time-resolved diffraction patterns corresponding to scattering vectors aligned at ±45° to the incident beam with a timing window set to detect interplanar spacings in the range $0.076 \leq d_{hkl} \leq 0.24$ nm. The load axis was at 45° to the incident beam allowing simultaneous measurements of lattice strains parallel and perpendicular to the applied load. The diffraction patterns were analyzed by Rietveld refinement. "Zero strain" lattice parameters were measured using NIST standard Si powder (lattice parameter, $a_0 = 0.543119$ nm) and powders made by filing alloys following the T4 and T6 treatments, both of which gave $a_0 = 0.404921$ nm for the Al phase.

3. Results and Discussion

3.1 Thermal Misfit Stresses

Measured lattice parameters as functions of applied stress (less than yield) were used to derive the lattice parameters for both the Si and the Al matrix phases at zero applied stress, since the initial diffraction pattern for each sample was collected with the sample positioned on the testing machine but at a very low applied stress (~ 10 MPa). These extrapolations (for, say, a T6 sample) gave (for Si) 0.542784 nm and 0.542722 nm for the axial and transverse measurements, respectively, and (for the Al matrix) 0.404992 nm and 0.404966, indicating, as expected from the relative thermal expansion coefficients, that the Si phase is under an hydrostatic compressive strain of -617×10^{-6} and the Al matrix an hydrostatic tensile strain of 143×10^{-6}. Using values of 162 GPa and 0.22 for the Young's modulus and Poisson's ratio (for Si) and 70 GPa and 0.34 for Al [6], these strains converted to stresses of -180 MPa in the Si particles and +29 MPa in the Al matrix.

The volume fraction of Si particles is 0.0757 so the net stress is (- 13.6 + 26.6) MPa, implying a violation of stress equilibrium of 13 MPa. Comparable small imbalances were found for all samples measured.

Application of the Eshelby theory [7] predicts a thermal misfit stress in the Si particles of 1.5 MPa/°C so that the value of -180 MPa suggests a temperature difference of 120°C, smaller than that which is experienced during the material processing. A likely explanation for this observation is stress relaxation during cooling.

3.2 Elastic Misfit Stresses

These arise in a composite under load because of differences in the elastic constants of the phases. From measured lattice constants in the elastic regime, strains (and hence stresses) in the phases were determined. For a T6 sample, for example, these were 1.28 MPa per MPa applied, in the Si particles and 0.93 per MPa in the Al matrix (see Fig.2). Using $(V_f\sigma_{Si} + (1 - V_f)\sigma_{Al} - 1)$, where the σs are the measured misfit stresses and V_f is the volume fraction of Si particles, the stress equilibrium violation at an applied stress

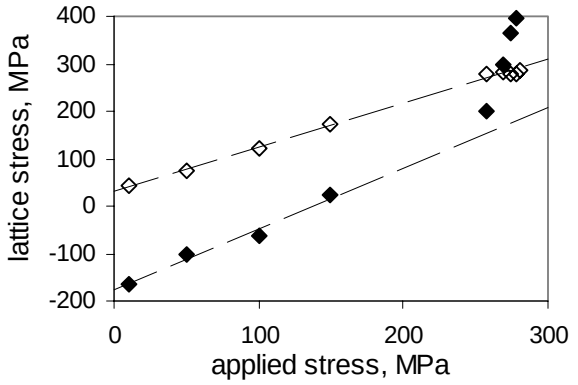

Fig. 2. Axial stresses in the Si particles (solid symbols) and Al matrix (open symbols) as the specimen is loaded (T6, fine SDAS). Dashed lines show the elastic regime.

of 1 MPa is -0.044 MPa (that is, an error of 4.4%). Eshelby theory [7] predicts elastic stresses of 1.27 MPa in the Si per MPa applied and 0.98 MPa in the Al matrix, in reasonable agreement with the measured data, although it is emphasized that the microstructures of the present composites are more complex than can be treated by Eshelby theory.

3.3 Plasticity Misfit Stress

This arises when the Al matrix begins to flow around the Si particles. Its onset is evident in Fig. 2 in which the axial stresses in the Si particles and Al matrix are plotted as the specimen is loaded beyond yield, by departures from the dashed elastic lines. Unfortunately, it is not possible to extract the plasticity contribution from the data except at high plastic strains as explained below. The apparently obvious assumption that $\sigma_{total} = \sigma_{thermal} + \sigma_{elastic} + \sigma_{plastic}$ is invalid. This is because the $\sigma_{thermal}$ term is not constant. It is a function of the plastic strain, reducing from its full initial value at a plastic strain of zero (i.e., for all applied stresses up to and including yield) to almost zero at a plastic strain of 1% or 2% [8]. This problem was not appreciated by us in our earlier work [9] and a full numerical stress analysis is in the process of being carried out for a future publication.

3.4 The Fracture Strength of the Si Particles

Si particles, particularly larger ones, begin to fracture at a plastic strain of ~ 0.01 [1] at which σ_{total} is in the range 300 – 330 MPa for T6 and 200 – 220 MPa for T4 material. These give a lower limit to the particle strength, and this is considerably less than the 500 – 3500 MPa suggested from earlier work involving Weibull analysis of data following mechanical testing and optical observations of cracked particles [5]. Future experiments are planned, particularly involving compression testing for which this initial particle cracking will not be an issue.

Acknowledgments

We acknowledge CCLRC for access to ENGIN-X and General Motors R&D for the cast plates. TRF, JRG and DV acknowledge support from the Access to Major Research Facilities Programme, a component of the International Science Linkages Programme under the Australian Government's innovation statement, Backing Australia's Ability.

References

[1] C.H. Cáceres, C.J. Davidson, J.R. Griffiths and Q.G. Wang, *Metall. Mater. Trans.* **30A,** 2611 (1999).
[2] J. Campbell, *Mater. Sci. & Technol.* **22**, 127 (2006).
[3] J.R. Griffiths, *Mater. Sci. & Technol.* **22**, 1001 (2006).
[4] A.A. Benzerga, S.S. Hong, K.S. Kim, A. Needleman and E. van der Giessen, *Acta Mater.* **49**, 3071 (2001).
[5] C.H. Cáceres and J.R. Griffiths, *Acta Mater.* **44**, 25 (1996).
[6] V.A. Lubarda, *Mechanics of Materials*, **35**, 53 (2003).
[7] T.W. Clyne and P.J. Withers, *An Introduction to Metal Matrix Composites*, (Cambridge University Press, 1993).
[8] J. LLorca, A. Martin, J. Ruiz and M. Elices, *Metall. Trans.* **24A**, 1575 (1993).
[9] T.R. Finlayson, J.R. Griffiths, D.M. Viano, M.E. Fitzpatrick, E.C. Oliver and Q.G. Wang, in *Shape Casting: The Second Int. Symposium*, eds. P N Crepeau, M Tiryakioglu, J Campbell, TMS (The Minerals, Metals and Materials Society), p.127 (2007).

Electrical Properties of Pure and Oxygen-Intercalated Fullerene Films

M. Foley, C. Ton-That and L. Kirkup

Department of Physics and Advanced Materials, University of Technology Sydney,
P.O. Box 123, Broadway, NSW 2007, Australia
Email: Matt.J.Foley@gmail.com

The conductivity of polycrystalline fullerene films as a function of oxygen concentration was investigated and found to be affected significantly by changes in oxygen partial pressure. The conductivity of the film was fitted to an Arrhenius curve. Analysis of the data indicated that a change of 0.11eV in activation energy occurred as the oxygen pressure was varied over two orders of magnitude.

1. Introduction

In recent years it has been shown that the electrical characteristics of fullerene films are sensitive to environmental factors. Another notable feature of solid fullerene structures is the intercalation of molecular gases into the interstitial sites of these structures. Previous studies have shown influence of oxygen gas and temperature changes on the electrical, optical and structural properties of fullerene materials as determined by electron paramagnetic resonance (EPR) intensity changes and x-ray diffraction patterns [1], as well as more conventional electrical measurements [2-4]. The aim of this work is to investigate the effects of oxygen partial pressures on the conductivity of fullerene thin films. We were able to determine a relationship between the oxygen pressure and the electrical conductivity of the film and to provide insight into the electronic structure of oxygen-intercalated C_{60} film.

While previous work has been performed on the reactions between fullerene films and oxygen gas, such work focussed primarily on the impact of oxygen saturation on the fullerene material [3, 5-7], or the extent of oxygen photopolymerisation of the fullerene chains [8,9]. By contrast, the work reported here considers the use of vacuum chambers in conjunction with evaporation methods and heat stages in order to control the oxygen partial pressures in the sample chamber. This in turn allows us to obtain a conductivity/temperature plot for the oxygen partial pressures in order to determine a relationship between activation energies and oxygen partial pressures.

2. Experimental

Films of C_{60} were prepared by sublimation onto a clean glass substrate in a vacuum chamber operating at better than 10^{-7} Torr, which contain pre-deposited gold electrodes. The starting material C_{60} (Sigma-Aldrich Company, USA) was over 99% pure. A quartz-crystal microbalance was used to monitor the rate of deposition and final film thickness. Film thickness and uniformity in depth were also characterised by carrying out a series of image scans across scratches cut through the film using an Atomic Force Microscope tip scratch method described previously [10]. Conductivity measurements were performed using a Keithley Two Probe Electrometer in the dark vacuum chamber (pressure less than 10^{-7} Torr), and in oxygen atmospheres with pressures of 10^{-3} and 10^{-5} Torr. The temperature of the sample was controlled using an electric heater and measured with a thermocouple attached to the rear of the sample.

3. Results

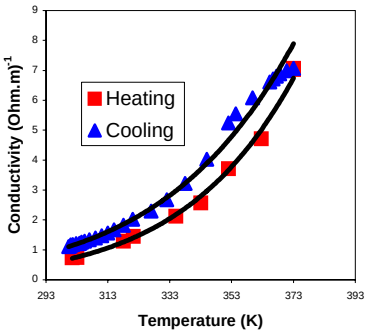

Figure 1. Temperature dependence of conductivity of a C_{60} film in vacuum 10^{-7} Torr after one heating/cooling cycle.

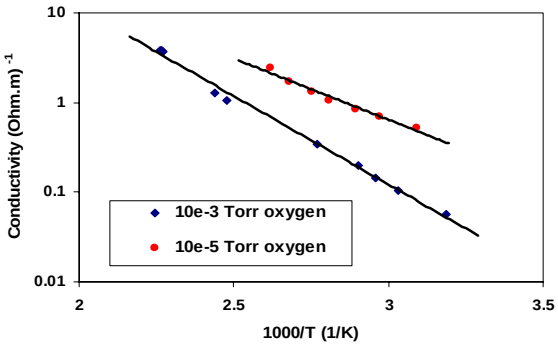

Figure 2. Arrhenius plot of conductivity showing its clear dependence of the conductivity on the oxygen pressure.

3.1 Heating and Cooling Cycles

As is apparent from Figure 1, the room temperature conductivity of the film remains almost constant after the first cycle, indicative of a more stable – but potentially polycrystalline – material, unaffected by further annealing cycles [3]. Subsequent annealing of the film does not cause significant changes to the film conductivity, allowing the temperature-dependent electrical measurements to be carried out in situ without causing further changes in the polycrystalline structure of the film.

While the thickness of the film was being determined, it was observed that the film showed signs of crystalline grains approximately 200nm in diameter on the surface of the fullerene film. This is indicative of a polycrystalline C_{60} film, confirming the polycrystalline structure of the film.

3.2 Impact of Oxygen Partial Pressures

Electrical conductivity of fullerene films was found to be highly sensitive to oxygen partial pressures in the pressure range from 10^{-3} to 10^{-5} Torr. It was noted that maintaining the film in an atmosphere of nitrogen has no significant effects on the conductivity. Exposure to oxygen at a pressure of 10^{-3} Torr induces an abrupt fall of the conductivity by two orders of magnitude. Figure 2 shows that the change in temperature at each oxygen concentration has a significant influence on the electrical conductivity. The linear relationship of lnσ against 1000/T observed for the pure and oxygen-intercalated films indicates the temperature-dependent electrical conductivity is thermally activated and can be described by the Arrhenius relation (Equation 1). This relation also indicates the nature of semiconductor conduction as it refers to the rate at which the carriers diffuse through the material as a function of temperature.Log-linear plot of conductivity σ against 1/*T*, as shown in Figure 2, allows the determination of the activation energy for the fullerene films. Table 1 shows the activation energies of our films as well as previously reported values, which show that the activation energies of oxygen-intercalated films are generally higher than pure films kept in vacuum. The fact that the activation energy of the fullerene film increases from 0.27 to 0.38 eV as the oxygen pressure increases from 10^{-5} to 10^{-3} Torr indicates that oxygen has a significant impact on the film electrical properties.

$$\sigma = \sigma_0 e^{\left(-\frac{E_a}{kT}\right)}$$

Equation 1. The Arrhenius Equation where σ_0 is the pre-exponential factor and E_a is the activation energy.

Oxygen molecules can interact with fullerene films and form a dipole moment from the C_{60} to the O_2 [4]. This creates a complex centre that can act as either an acceptor to free

electron carriers [5], or as a scattering centre that reduces carrier mobility. If the electrons are trapped by the oxygen-fullerene dipoles, it is reasonable to assume that there will be a reduction in the carrier concentration directly correlated to the concentration of oxygen gas present within the fullerene film, which in turn is related to the concentration of oxygen in the environment. The drop in carrier concentration leads to a reduction in electrical conductivity and an increase in activation energy.

	E_a (eV)
Single fullerene crystal [2]	~0.2
Fullerene film (Highly crystalline) [3]	0.26
Fullerene film – 10^{-5} Torr oxygen (this study)	0.27
Single crystal under high pressure (7.5×10^6 Torr) [11]	0.32
Fullerene film – 10^{-3} Torr oxygen (this study)	0.38
C_{60}/C_{70} film [12]	0.43

Table 1. Activation energies of pure and oxygen-intercalated fullerene films.

Our fullerene films exhibit an association between oxygen pressure and activation energy. The increase in the activation energy as oxygen pressure increases indicates that oxygen concentration within the film is directly related to the oxygen pressure surrounding the film. It was also observed during the measurements that there were no significant changes in the film conductivity after 38 min oxygen exposure so long as the oxygen pressure and sample temperature were maintained unchanged. This indicates the film has reached oxygen equilibration within the time period.

4 Conclusions

We found that oxygen intercalation into fullerene films has a considerable impact on the film electrical properties, with their conductivities dropping by several orders of magnitude in an oxygen atmosphere. Both pure and oxygen-intercalated fullerene films show the semiconductor conduction and follow the Arrhenius relationship. As the oxygen partial pressure increases from 10^{-5} to 10^{-3} Torr, the activation energy of the fullerene film decreases by 0.11 eV. It appears credible that further development into fullerene-based gas sensors could be feasible.

Acknowledgements

The authors would like to thank Geoff McCredie for his assistance in thin film deposition and patterning.

References

[1] E.A. Katz et al., *Physica B* **304**, 348 (2001).
[2] Y.J. Xing et al., *Appl. Phys. Lett.* **87**, 263117 (2005).
[3] A. Zahab and L. Firlej, *Solid State Comm*. **87**, 893 (1993).
[4] C.-M. Yang, J.-L. Liao, and K.-C. Chiu, *J. Appl. Phys.* **96**, 1934 (2004).
[5] T. Arai et al., *Solid State Comm.* **84**, 827 (1992).
[6] Bernier et al., *Phys.Rev.* B **53**, 7535 (1996).
[7] Duclos et al., *Solid State Comm.* **80**, 481 (1991).
[8] A.M. Rao et al., *Science* **259**, 955 (1993).
[9] P. Zhou, Z. Dong, A.M. Rao, and P.C. Eklund, *Chem. Phys. Lett*. **211**, 337 (1993).
[10] C. Ton-That, A.G. Shard, and R.H. Bradley, *Langmuir* **16**, 2281 (2000).
[11] B. Sundqvist, *Adv. in Phys.* **48**, 1 (1999).
[12] Pichler et al., *J. Phys.: Cond. Matt*. **3**, 9259 (1991).

The effect of filters in x-ray phase contrast imaging.

A. W. Greaves, and P. Cadusch

Department of Engineering and Industrial and Sciences, Swinburne University, Victoria 3121, Australia.

Phase contrast experiments using a polychromatic, micro-focus x-ray source were conducted on dialysis fibres with and without various filter materials, showing a reduction in phase contrast. The spectrums were measured using multi-channel analyzer and incorporated into computer simulations using Fresnel diffraction. Calculations showed little difference between the filtered and unfiltered cases until source and detector considerations were taken into effect, giving rise to a possible explanation for phase contrast reduction.

1. Introduction

X-ray phase contrast imaging offers potential advantages over traditional absorption radiography such as the ability to image low atomic Z materials that do not appreciably attenuate the beam, with the added advantage that regions of different refractive index are delineated by a diffraction edge providing greater visual acuity. Furthermore the phase component of the complex index of refraction is less dependent on higher photon energies giving rise to the possibility of reduced patient dose in techniques such as mammography[1].

The requirements for phase contrast are an x-ray source with sufficient spatial coherence and sufficient propagation distance between the detector and the sample to allow the transformation of phase information into recordable intensity variations. If polychromatic sources are to be used, often the lower energy x-rays must be filtered from the beam as they have insufficient energy to contribute to useful diagnostic information, and hence add only to sample dose. However, experiments have shown that the use of filters can decrease the phase contrast information considerably and the mechanism for this effect is not clear.

Using a microfocus x-ray tube with a fibre as a suitable phase object, measurements of phase contrast were made with and without various filter materials such as Aluminium, Copper, Nickel and Polymethylmethacrylate(PMMA). The spectrums of each case were also measured and used in a custom Fresnel diffraction program to determine if the reduction in phase contrast were due to the spectrum change alone. Surprisingly it was found not to be the case and other mechanisms in the imaging chain such material dispersion in the target and the finite source size and the scanning of the image plate were found to have significant effects.

2. Experimental

The x-ray source was a Feinfocus microfocus FXE 225-20, located at the CMMT of CSIRO. The source to detector distance was 2 meters, while the object was placed around 20 cm from the source. Detection was via Fujifilm image plates, scanned with a Fujifilm BAS5000 scanner at 25 μm resolution. The phase object was a Cuprophan™ fibre, made from regenerated cellulose with a 200 μm diameter and 8 μm wall thickness. All images were converted into photostimulable luminescent values (psl) format via reference [2].

The images were further software processed to ‘straighten’ the fibres for better phase contrast measurement. Natural deformities could be corrected in this way as well as fibre misalignment with scanner direction, which is important when averaging line profiles for noise reduction. Phase contrast was defined via

$$pc=(max-min)/(max+min). \quad (1)$$

3. Results

Phase contrast was found to decrease with increasing thickness of Aluminium, Silicon, Copper and PMMA. An example is shown (Fig. 1) for a range of Aluminium thicknesses from 0.03 to 1mm.

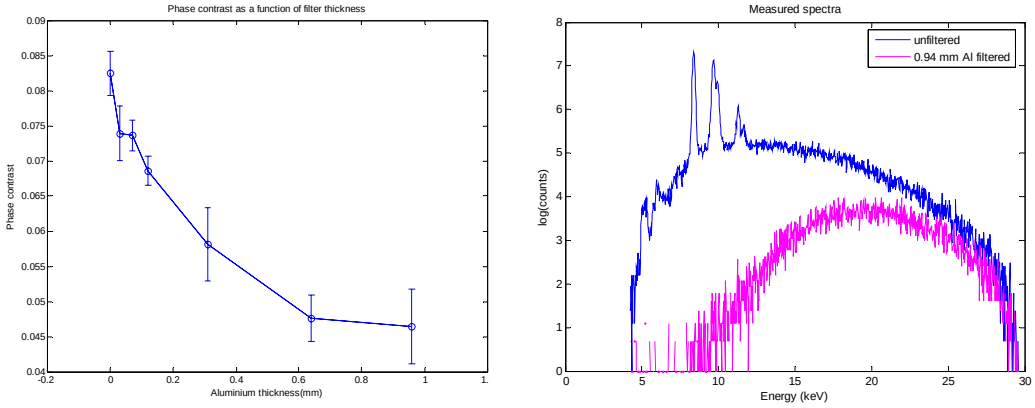

Fig. 1. Phase contrast as a function of aluminium thickness(left) and Fig.2 Measured spectra (right).

The measured unfiltered and 0.94 mm Al filtered spectra show (Fig. 2) strong L lines in the unfiltered case and a hardening of the beam as expected for the filtered case. It may be surmised that the strong phase contrast can be attributed to these L lines which are absent in the filtered cases, but in calculations based on Fresnel diffraction this proved not to be the case.

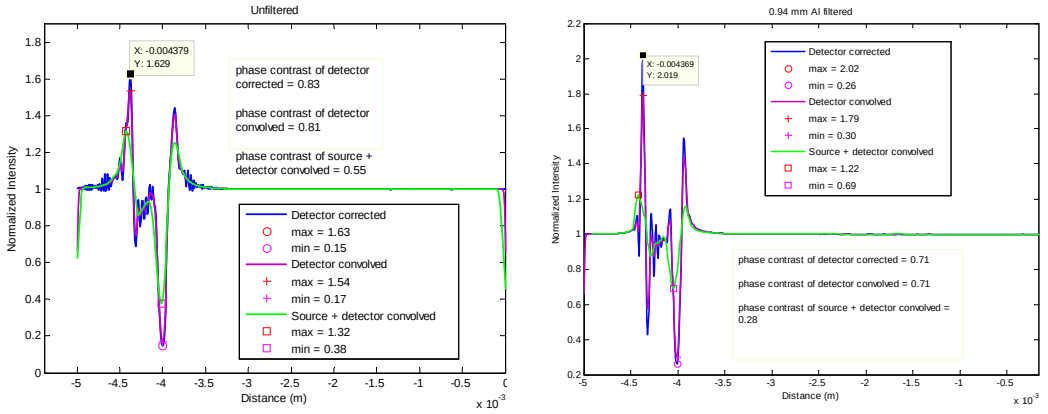

Fig. 3. Raw and convolved Fresnel diffraction pattern for unfiltered (left) and Fig. 4. 0.94 mm Al filtered diffraction pattern (right) respectively.

When a filter is used, the resulting x-ray spectrum is shifted towards the higher energies (Fig.2) and this changes the amount of dispersion in the fibre so that overall pattern due to refraction narrows compared to the unfiltered pattern. Upon convolution (Fig.3 and 4) with the source size and scanner as described in reference [3], these narrower peaks are smoothed out significantly more than the unfiltered peaks, resulting in a decrease of the calculated phase contrast values as observed in experiments. Phase contrast for example is decreased by approximately 50% from 0.55 to 0.28, in the case of a 0.94 mm Aluminium filter. There are discrepancies in the absolute values of the phase contrast but good agreement with the relative changes due to the introduction of certain filters. This not surprising considering the exact

shape and size of the source and density of the target material are unknown, and is the subject of further reseach.

Finally, figure 5 shows the effect of the Fresnel based calculations with the measured spectra of different materials. It shows that phase contrast is reduced for higher Z materials as well as thickness by the same mechanism as before with the Aluminium. Also the placement of the filter whether near the source or detector has little effect on phase contrast as does the size of the grain structure showing that the effect is largely due to the bulk and not the internal structure of the material.

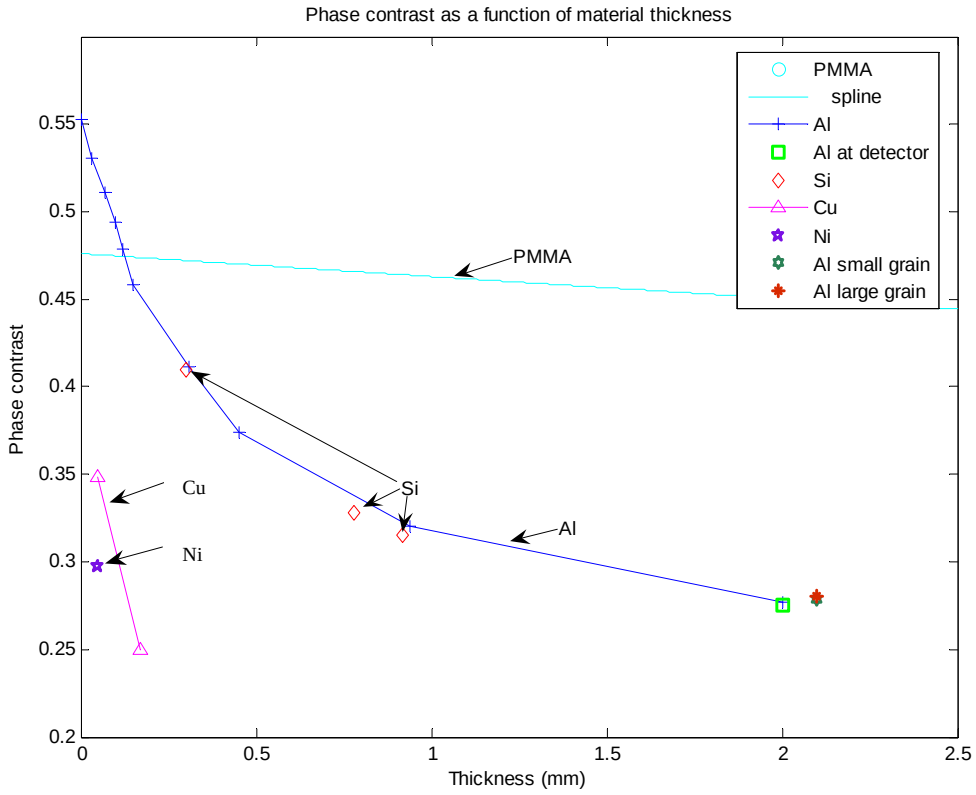

Fig. 5. Phase contrast calculations for various materials and thickness.

Acknowledgments

Andrew Stevenson and Andrew Pogany of CSIRO are acknowledged.

References

[1] S.W. Wilkins, T.E. Gureyev, D. Gao, A. Pogany, and A.W. Stevenson, *Nature* **384**, 335 (1996).

[2] http://www.esrf.eu/computing/scientific/FIT2D/FIT2D_REF/node104.html

[3] D.M Tucker and P.S Rezentes. *Medical Physics* **24(6)** 887 (1997).

Magnetic Order Studies of $ErNiAl_4$

W. D. Hutchison[a], D.J. Goossens[b], B. Saensunon[a], G. A. Stewart[a], M. Avdeev[c] and K. Nishimura[d]

[a]*School of Physical, Environmental & Mathematical Sciences, The University of New South Wales, Australian Defence Force Academy, Canberra ACT 2600, Australia.*
[b]*Research School of Chemistry, The Australian National University, Canberra ACT 0200, Australia.*
[c]*Bragg Institute, Australian Nuclear Science and Technology Organisation, Lucas Heights NSW 2234, Australia.*
[d]*Faculty of Engineering, University of Toyama, Toyama 930-8555, Japan.*

Specific heat measurements on $ErNiAl_4$ show a phase transition at 5.8(1) K. Magnetisation data confirms the low temperature phase is antiferromagnetic in nature, while neutron powder diffraction data suggests an incommensurate structure similar to the intermediate magnetic phase of $TbNiAl_4$.

1. Introduction

The intermetallic series $RNiAl_4$ (R = rare earth) exhibits intriguing magnetic properties. For the compounds with R = Pr, Tb and Gd there are at least two magnetic phase transitions as a function of decreasing temperature, including an incommensurate magnetically ordered phase (e.g. [1-3] and references therein). In addition, the low temperature magnetisation of $TbNiAl_4$ exhibits two transitions as a function of applied magnetic field [4]. The choice of rare earth is crucial in determining the magnetic anisotropy. The Kramers ion Nd in $NdNiAl_4$ orders along the *b*-axis, perpendicular to that of neighbouring non-Kramers $PrNiAl_4$ which orders along the *a*-axis. Furthermore $NdNiAl_4$ does not show any sign of a second magnetic phase to the lowest temperatures.

We report here on a study aimed at improving the understanding of the systematics of the $RNiAl_4$ series. Heat capacity and magnetisation are recorded for $ErNiAl_4$ as a function of temperature. Neutron powder diffraction at approximately 5.8 K that shows magnetic order.

2. Sample preparation

The $ErNiAl_4$ compound was synthesised by repeated argon arc melting of stoichiometric amounts of 99.9% Er together with 99.99% Ni and Al. The resulting ingots were annealed for seven days at 1300 K wrapped in tantalum foil under vacuum. The resulting material was checked for impurity phases by powder x-ray diffraction (XRD). Magnetisation measurements were made using a SQUID magnetometer in applied magnetic fields up to 7 T and in the temperature range from 2 to 300 K. The specific heat was measured in zero magnetic field using the relaxation method on a Quantum design PPMS system.

The powder specimen for neutron diffraction was prepared by grinding a number of ingots. Neutron powder diffraction data were collected using the MRPD at the HIFAR reactor, Lucas Heights. Use of a closed cycle refrigerator allowed these measurements for temperatures down to a nominal base temperature of 5 K. At base temperature, the two thermometers, top and bottom of the specimen read 5.4 K and 6.1 K respectively. We have assigned an average temperature 5.8 K for this run. Data were analysed using Rietica [5] and FullProf [6], the latter allowing for refinement of magnetic structures.

3. Results

3.1 Specific heat and magnetisation

Specific heat data, collected down to 2 K, is shown Fig. 1 and feature a single significant peak corresponding to a single magnetic transition at 5.8(1) K. This result is suggestive of only two magnetic phases, much like the other Kramers ion system, $NdNiAl_4$. The magnetisation data of Fig. 2 also support the case for a transition at 5.8 K, and suggest that the lower temperature phase is likely antiferromagnetic.

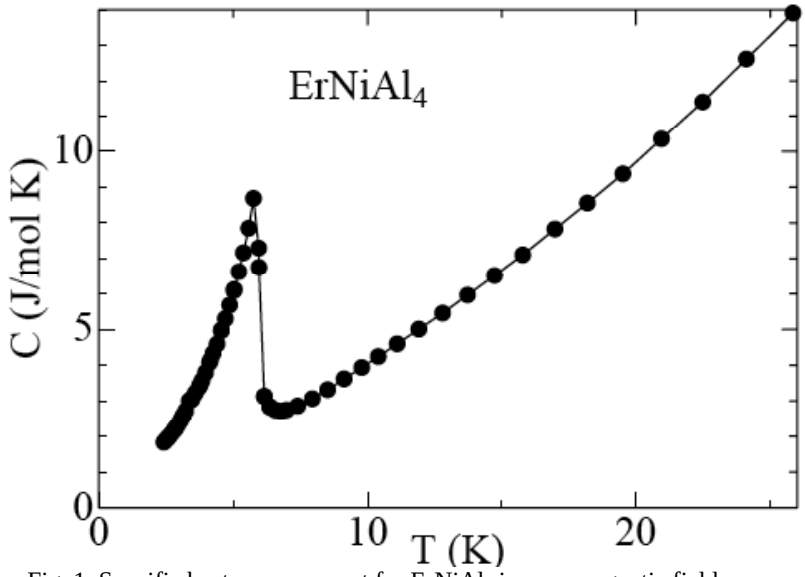

Fig. 1. Specific heat measurement for $ErNiAl_4$ in zero magnetic field.

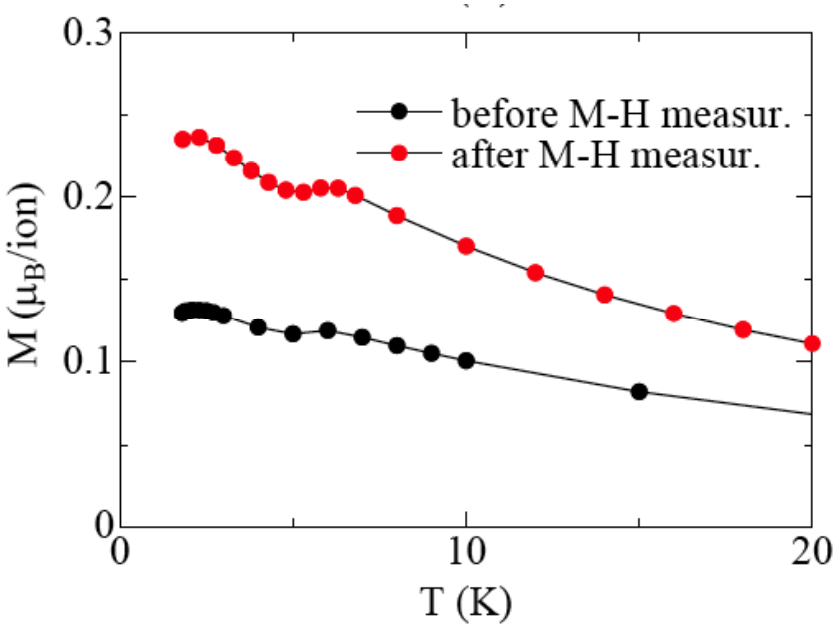

Fig. 2. Magnetisation measurements for ErNiAl4 powder, collected at 0.1 T applied magnetic field, before and after exposing the sample to a high magnetic field (7 T).

3.2 Neutron diffraction

Neutron diffraction data collected at 10 K showed structural peaks only and could be fitted with structural parameters much as for $TbNiAl_4$ [2]. However data collected at the nominal base temperature of the cryostat, average sample temperature approximately 5.8 K,

shows the onset of magnetic order. This lowest temperature data, shown in Fig 3, has been fitted using Fullprof to reveal incommensurate magnetic order. A propagation vector of $\tau = (h_\tau k_\tau l_\tau) = (0.191\ 1\ 0.015)$ is assigned with the moments in an antiferromagnetic configuration along the *b* axis. This structure is similar to the incommensurate (intermediate) phase of $TbNiAl_4$, for which $\tau = (0.171\ 1\ 0.038)$ was assigned [2].

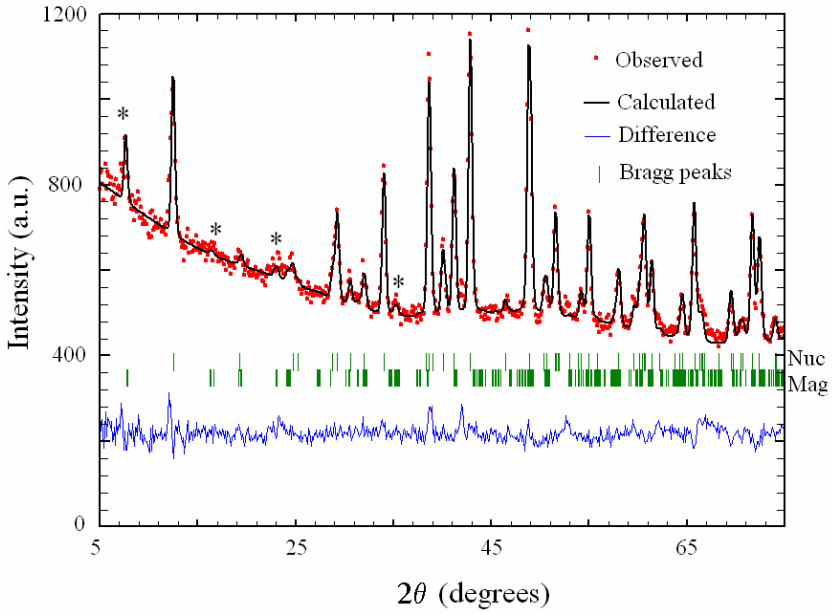

Fig. 3. Neutron diffraction data for ErNiAl4 powder, collected in zero applied magnetic field and at a sample temperature close to 5.8 K. The Fullprof refinement suggests incommensurate magnetic order (starred peaks).

In conclusion, the specific heat measurement suggests that $ErNiAl_4$ has a single phase transition, like $NdNiAl_4$, and the neutron diffraction data reveal a low temperature incommensurate magnetic order such as seen in the intermediate temperature phase for $TbNiAl_4$. Further definitive neutron powder diffraction measurements at lower temperatures will be possible with the OPAL reactor's new suite of instruments.

Acknowledgments

The Australian Institute of Nuclear Science and Engineering (AINSE) is gratefully acknowledged for a grant enabling the neutron diffraction study.

References

[1] G.A. Stewart, W.D. Hutchison, A.V.J. Edge, K. Rupprecht, G. Wortmann, K. Nishimura and Y. Isikawa, *J. Magn. Magn. Mater.* **292** 72 (2005).
[2] W.D. Hutchison, D.J. Goossens, K. Nishimura, K. Mori, Y. Isikawa and A.J. Studer, *J. Magn. Magn. Mater.* **301** 352 (2006).
[3] K. Nishimura, T. Takahiro, K. Mori, Y. Isikawa, W.D. Hutchison and D.H. Chaplin, *Jpn. J. Appl. Phys.*, **42** 5565 (2003).
[4] T. Mizushima, Y. Isikawa, A. Mitsuda, K. Kobayasi, F. Ishikawa, T. Goto and S. Kawano, *J. Magn. Magn. Mater.* **272-276** e475 (2004).
[5] B.A. Hunter and C.J. Howard, *Rietica* (available from www.ccp14.ac.uk).
[6] J. Rodriguez-Carvajal, Physica B **192** 55 (1993).

Crystallography of Biomimetic Silica Carbonate Precipitates

A.-K Larsson [a], A. M. Carnerup [b], S. T. Hyde [b] and J.D. Fitz Gerald [c]

[a] *Research School of Chemistry, Australian National University, 0200 ACT, Australia.*
[b] *Research School of Physical Sciences and Engineering, Australian National University, 0200 ACT, Australia.*
[c] *Research School of Earth Sciences, Australian National University, 0200 ACT, Australia.*

In this contribution, we describe the orientational distribution of the carbonate crystallites within some silica carbonate biomorphs. Such precipitates with biomimetic morphologies are formed in alkaline silicate solutions containing barium ions which react with carbon dioxide dissolved from ambient air. We conclude that elucidation of the detailed crystallography and crystallite patterns of a wider range of biomorphs will be vital before any models of their formation can be confirmed.

1. Introduction

Aggregates of astonishingly life-like shapes precipitate from basic silicate solutions that contain alkaline earth metal ions [1]. These biomimetic morphologies (biomorphs) can be so life-like that they may be mistaken for early fossils [2-4]. From the materials-science point of view, these structures are extremely interesting as they can serve as models for the synthesis of new ceramic materials with hierarchical structure and complex form.

It is well documented that these biomorphs comprise amorphous silica and nanocrystalline alkaline-earth carbonate (formed by trapping carbon dioxide from the air) but although structures of biomorphs have been studied [1-10] there is still only limited information about their details and the underlying chemical and physical processes for this remarkable self-assembly. In principle, two models have been put forward: [9] the "top-down" model in which the silica membrane dictates (and templates) the shape [6] and the "bottom-up" model, in which local twist constraints between adjacent nano-crystallites dictate the shape [8, 10] In this contribution, we describe the orientational distribution of the carbonate crystallites of some biomorphs.

The crystal structure of barium carbonate, witherite, consists of a hexagonally close-packed array of Ba ions (compressed along the c-axis) with the carbonate groups laying flat in all octahedra (Fig. 1a and b). In alternate rows along <100> the carbonate triangles are rotated in opposite directions (accompanied with a shift up or down along the c axis). This lowers the symmetry of the substructure ($P6_3/mmc$) and gives rise to the orthorhombic (*Pmcn*) crystal structure of witherite. The common witherite twinning relates to rows of carbonate groups within the orthorhombic structure being able to lie along one of the three possible $<100>_{hex}$ directions resulting in three possible twin orientations. For initial indexing of selected area electron diffraction patterns (SAEDP) of the nanocrystalline witherite of the biomorphs, we ignore the direction of the ordering pattern of the carbonate groups and only use the underlying $P6_3/mmc$ sublattice.

2. Sample preparation

The helical biomorphs were synthesised by mixing 1 ml of a 10 mM $BaCl_2$ solution with 1 ml of a 17 or 8.5 mM silicate solution (calculated on the basis of monomer) in a plastic cylindrical open container (∅ = 1.5 cm, h = 1.7 cm). Prior to mixing, the pH of the silicate solution was adjusted to 11.3 with 0.1M NaOH.

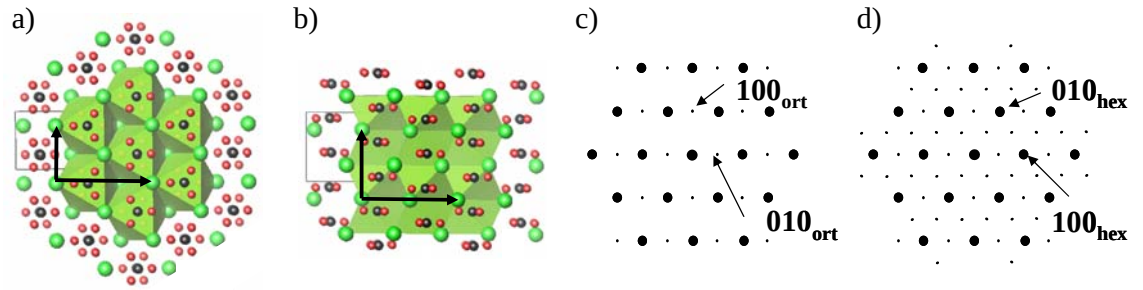

Fig. 1. The crystal structure of witherite shown along a) $[001]_{hex}$ and b) $<100>_{hex}$. The reciprocal lattice of witherite c) indexed in the conventional *Pmcn* space group and d) showing all three possible witherite twin directions and indexed using the underlying $P6_3/mmc$ subcell.

3. Results

Typical morphologies of some selected biomorphs are shown in Fig. 2. Polarised light micrographs (Fig. 3a) of a thin (ca. 10 micron) section of a worm like biomorph (such as Fig. 2a) confirm orientational order of the carbonate crystallites suggested from scanning electron micrographs [9]. The direction of the black Maltese cross in Fig. 3a relative to the biomorph shows that the crystallites tend to align perpendicular to the biomorph surface. Images from transmission electron microscopy (TEM) in Fig. 3b and c are compatible with this, as the axis of elongation of crystallites lies perpendicular to the edge of the aggregate.

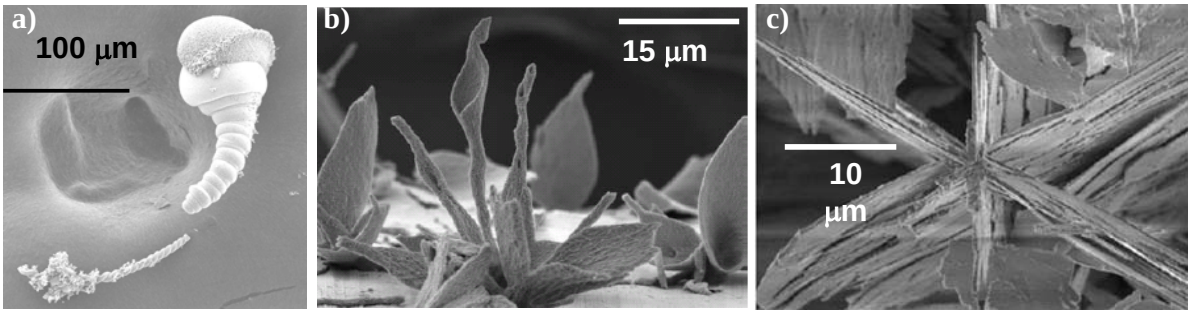

Fig. 2. Examples of biomorphs from a) a standard experiment ($BaCl_2$ = 5mM, SiO_2 = 8.5 mM, 298K) b) the standard concentrations 368K and c) low silica concentration (4.2 mM) and 378K.

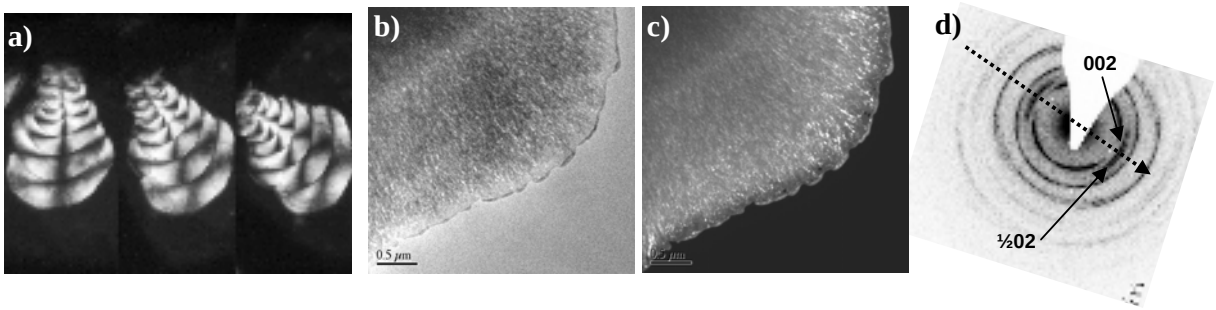

Fig. 3. a) Polarised light micrograph, b) Bright Field and c) Dark Field (from around 002) TEM images of a biomorph such as in Fig. 2. d) SAEDP of the area in b) and c) are indexed in the hexagonal sub cell.

The SAEDP in Fig. 3d confirms that the average c axis is oriented perpendicular to the edge and shows that spread in **c**-axis orientation is about 50° within the illuminated area. Note also that the reflection $^1/_2 02_{hex}$ (equivalent to 012_{ort}) is present confirming that the carbonate groups are at least partially ordered *within* twin domains. It is not trivial to extract more information from these SAEDPs as preparation of thin sections of the tiny aggregates usually destroys some or all of the biomorph external surfaces.

It was found that by increasing the temperature to 70°C, sheet and band like formations thin enough to examine by TEM could be grown directly on carbon-coated copper grids (Figs. 2a, 4a and 4b). SAEDP from the band in Fig. 4b shows a single-crystal-like $<1\bar{1}0>_{hex}$ SAEDP (Fig. 4c). Upon tilting the band either + or - 30° around the **c** axis, apparent $<100>_{hex}$ SAEDPs (Fig. 4d) indicate an average six-fold rotation axis of the sampled area. The weak superstructure reflections (originating in the orthorhombic ordering of the carbonate groups) appear in all $<100>_{hex}$ and $<1\bar{1}0>_{hex}$ zone axis SAEDPs but are always much weaker than in a $<100>_{ort}$ or $<010>_{ort}$ SAEDP of witherite. This is all compatible with these superstructure reflections in each zone axis arising from only one of the three possible twin orientations. The bands in Figs. 4a and b hence consist of small crystallites collectively oriented essentially as one single crystal with respect to the underlying hexagonal average structure, but with all three twin orientations present.

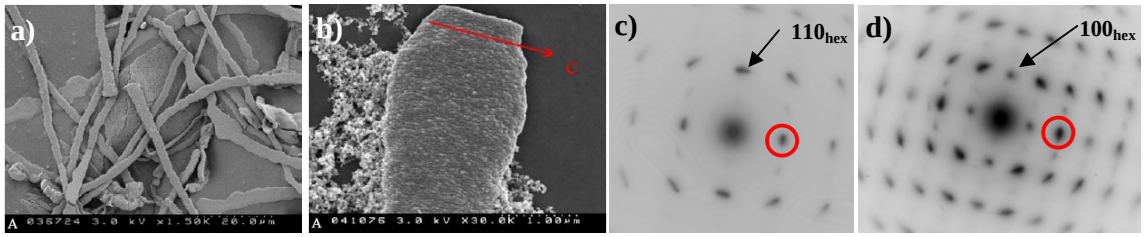

Fig. 4. a) and b) FESEM images of band-like formations from the same sample as Fig. 2b. c) and d) EDPs of the tip of the band in b) with the 002 reflection circled.

If the temperature was increased to 80°, and [SiO_2] lowered from 8.5 to 4.2 mM, further crystallographic ordering of the crystallites was documented. SAEDPs from the "leaves" of crystallites shaped as palm trees (Fig. 2c) reveals that they always consist of two out of the three possible twins.

We conclude that elucidation of the detailed crystallography of a further range of biomorphs will be vital before any models of their formation can be confirmed.

Acknowledgments

Financial support from the Australian Research Council (AKL) is gratefully acknowledged.

References

[1] J.M. Garcia-Ruiz *J. Cryst Growth* **73,** 251 (1985).
[2] J.M. Garcia-Ruiz, *Origins of Life and Evolution of the Biosphere* **24**, 451 (1994).
[3] J.M. Garcia-Ruiz. A. Carnerup, A.G. Christy, N.J. Welham and S.T. Hyde *Astrobiology* **2,** 353 (2002).
[4] A.M. Carnerup, S.T Hyde, A.G. Christy, J.M. Garcia-Ruiz, A.-K. Larsson, The Record of Early Life: In Search of Biosignatures, in *Cellular Origin, Life in Extreme Habitats and Astrobiology, vol 10 (2006)* ed. J. Seckbach (Springer, 2006).
[5] J.M. Garcia-Ruiz, *Geology* **26**, 843 (1998).
[6] J.M. Garcia-Ruiz and J.L Amoros, *J. Cryst Growth* **55,** 379 (1981).
[7] J.M. Garcia-Ruiz, S.T. Hyde, A. Carnerup, A.G. Christy, M.J. Kranendonk and N.J. Welham, *Science* **302,** 1194 (2003).
[8] T.S. Terada, S. Yamabi and H. Imai, *J. Cryst Growth* **253,** 435 (2003).
[9] S.T. Hyde, A.M. Carnerup, A.-K. Larsson, A.G. Christy and J.M. Garcia-Ruiz, *Physica* **A 339**, 24 (2004).
[10] H. Imai, T. Terada and S. Yamabi, *Chemical Communications* 484 (2003).

$La_{0.7}Sr_{0.3}MnO_3$ buffer layer and YBCO film deposited by pulsed laser deposition

A. H. Li, D. Q. Shi[1], R. Zeng, J. H. Kim, S. X. Dou

Institute for Superconducting & Electronic Materials, University of Wollongong, NSW 2522, Australia

In this report, $La_{0.7}Sr_{0.3}MnO_3$ thin films were deposited on single crystal $SrTiO_3$ (STO) substrates. The deposition conditions were analysed and pure *c*-axis film was epitaxially grown. The surface of the YBCO film on the top of $La_{0.7}Sr_{0.3}MnO_3$ /$SrTiO_3$ was examined with atomic force microscopy (AFM). Superconducting YBCO thin film was deposited by pulsed laser deposition on the $La_{0.7}Sr_{0.3}MnO_3$ /$SrTiO_3$. T_c and J_c of the samples were measured and calculated through DC magnetic measurements using a physical properties measurement system (PPMS).

1. Introduction

The second generation high temperature superconductor (HTS) tape is termed 'coated conductor', that is, an $YBa_2Cu_3O_{7-d}$ (YBCO) coating on a metallic tape substrate with a multilayer buffer in between. Rolling-assisted biaxially textured substrates (RABiTS) have been developed for this purpose, and the method has become a cost effective approach to the fabrication of coated conductor [1,2]. In general, a coated conductor architecture involves epitaxial fabrication of a thin layer ~1-2 μm in depth of HTS film, usually YBCO, on one or more biaxially textured buffer layers deposited on a thick (~80 μm) flexible metal substrate (Ni or dilute Ni alloys). These buffer layers provide a template allowing reduced lattice mismatch between the YBCO and the substrate for *c*-axis aligned epitaxial growth, while providing a barrier to Ni diffusion from the metal substrate into the superconductor during deposition or ex-situ processing of the YBCO layer. For effective implementation at cryogenic temperatures (30-77 K), stabilization against thermal runaway will be required in the event of an over current situation (exceeding the critical current I_c of the HTS coating). A solution is to electrically shunt the HTS layer, either by an intermediate conductive buffer layer to a low resistivity metal substrate or by depositing a stabilizing metallic cap layer, e.g., Cu or Ag, onto the HTS coating. The latter solution will increase the cross-sectional area, hence reducing the engineering critical current density J_e (I_c per unit total cross-sectional area). The most desirable approach from an applications perspective is to deposit conductive buffer layer on the metallic tape in order to shunt the current to the tape when the HTS layer leaves the superconducting state [3]. Coupling the HTS layer adequately to a metallic tape through a conductive buffer layer also provides an overall less complicated structure with reduced resistance and an increased thermal conductivity, providing more efficient heat transfer to either a coolant bath or through the thermal diffusivity of the system.

In recent years, the study of colossal magnetoresistance (CMR) in perovskite-structured, doped lanthanum manganese oxides has generated great interest in fabricating these materials as thin film heterostructures for various technological applications. The variant $La_{0.7}Sr_{0.3}MnO_3$ (LSMO), apart from its CMR properties, is also an electrically conductive oxide with good thermal stability. Moreover, the pseudocubic lattice parameter of 3.9 Å is a

[1] Present address: Institute for Superconducting and Electronic Materials, University of Wollongong, Australia

close match to YBCO film. Therefore, it is of interest to investigate the viability of LSMO as a conductive buffer layer on RABiTS for YBCO-coated conductors. Here, we report the fabrication of $La_{0.7}Sr_{0.3}MnO_3$ buffer layer deposited by pulsed layer deposition on single crystal $SrTiO_3$ (STO) substrate.

2. Sample preparation

LSMO targets were made by sintering a pressed mixture of La_2O_3, $SrCO_3$, and MnO_2 powder according to the element stoichiometry at 1150°C for 8 hours in air. X-ray diffraction (XRD) phase analysis showed it was a pure $La_{0.7}Sr_{0.3}MnO_3$ phase. LSMO and YBCO targets were ablated by an excimer KrF pulsed laser with 248 nm wavelength. The LSMO buffer layer was epitaxially deposited on STO substrate at 550°C under 10 mTorr O_2 pressure. The laser beam energy was fixed at 300 mJ per pulse at 3 or 5 Hz. Single crystal (00l) STO substrates of 3x3mm^2 were attached with silver paste to a sample stage (also the heater) which was directly facing the target at an on-axis position. A laser beam was directed to the target surface at an angle of 45° to the normal of the target, with the target-substrate distance 40 mm. The size of the laser spot on the target was ~ 5×2 mm^2, and the laser pulse energy density on the target was ~ 3 J/cm^2. The target was rotated at 10 rpm.

An X-ray diffraction system was used to analyse the phase and orientation of films with XRD θ -2θ scans. The temperature and field dependences of the magnetic moment were investigated by employing a Quantum Design PPMS using a superconducting quantum interference device (SQUID) magnetometer with a maximum field of 9 T and temperature 5 < T < 300T. An atomic force microscope (AFM) was used to more fully characterize the surface morphology and roughness of the buffer layers.

3. Results

The background pressure of the deposition chamber was about 1x10^{-6} Torr. After deposition of the LSMO buffer layer, the oxygen pressure was subsequently increased to 200 mTorr, and the superconducting YBCO layer was then deposited on the buffer layers. The YBCO film was deposited within a deposition temperature range of 770 - 790°C in 200 mTorr oxygen pressure. The laser conditions were: energy 300 mJ/pulse and repetition rate 5 Hz. Following deposition, the YBCO film was quickly cooled to 450°C under the deposition pressure, and then kept for 30 min under an oxygen pressure of 700 Torr. Fig. 1 is a typical XRD plot for an YBCO(500nm)/LSMO(100nm)/STO sample. In this figure, the LSMO film just has (002) and (004) peaks, but the (002) peak has overlapped with the STO (002) and the YBCO (003) peaks, while the (004) peak has overlapped with the STO (002) and the YBCO (006) peaks. The YBCO film has a pure *c*-axis orientation.

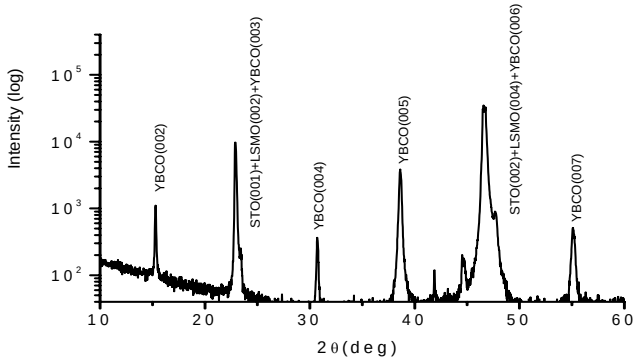

Fig. 1. XRD θ-2θ scan for a typical YBCO/LSMO/STO sample.

The T_c of the YBCO film was 90K as measured by DC magnetic measurements using PPMS. The J_c values were magnetically determined by applying the modified critical state model to the magnetic hysteresis loop via the relation $J_c = 2\Delta M/[a(1-a/3b)]$. This formula applies to a rectangular solid with field perpendicular to a face with sides b > a. Here, $\Delta M = (M^- - M^+)$, where M^- and M^+ are the magnetizations at temperature T measured in decreasing and increasing field *H* history, respectively. The curves shown in Fig. 2 are the $J_c(B,T)$ relationships for the YBCO film (500nm), which is consistent with reports that these $J_c(B,T)$ curves depend on the applied field and temperature through the mechanism of vortex trapping by dislocations over the entire field range. It can be seen that J_c can remain constant at some value of applied magnetic field for $T \leq 20K$, which means that there is a single vortex pinning regime.

AFM was used to examine the surface morphology and roughness. Fig. 3 is the AFM image of the YBCO (500 nm) surface. There are a few large outgrowths on its surface, and the surface roughness was increased compared to the roughness of LSMO film. The AFM scan on this specimen gives a root mean square roughness over a 50 μm × 50 μm area of about 43.4 nm, including the outgrowths, and 37.3 nm over the same area if outgrowths are excluded.

From the superconductivities of YBCO on the top of LSMO buffer layer it can be seen that the LSMO a suitable conductive buffer layer for YBCO coated conductor. The work of depositing LSMO film on metallic substrates, such as Ni and Ni-alloy, is in process.

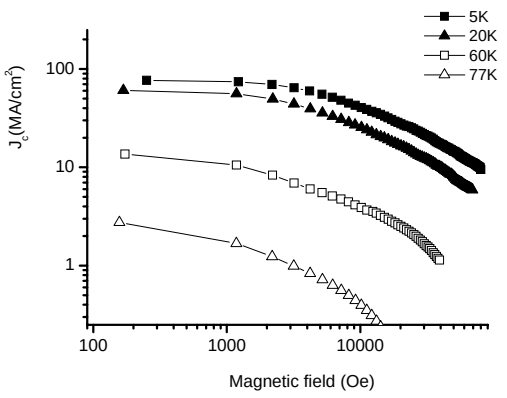

Fig. 2 Field dependence of the J_c at different temperatures for an YBCO(500nm) film on LSMO/STO.

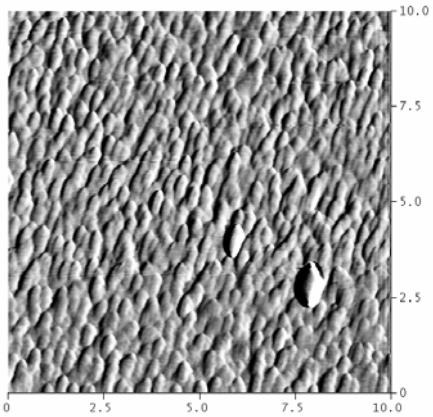

Fig 3. AFM image showing the surface morphology of the YBCO(500nm) film on LSMO/STO.

Acknowledgments

This work is financially supported by the Australian Research Council.

References

[1] D.P. Norton, A. Goyal, J.D. Budai, D.K. Christen, D.M. Kroeger, E.D. Specht, Q. He, B. Saffian, M. Paranthaman, C.E. Klabunde, D.F. Lee, B.C. Sales and F.A. List *Science* **274,** 755 (1996).

[2] A. Goyal, D.P. Norton, J.D. Budai, M. Paranthaman, E.D. Specht, D.M. Kroeger, D.K. Christen, Q. He, B. Saffian, F.A. List, D.F. Lee, P.M. Martin, C.E. Klabunde, E. Hartfield and V.K. Sikka, *Appl. Phys. Lett.* **69,** 1795 (1996).

[3] K. Kim, M. Paranthaman, D.P. Norton, T. Aytug, C. Cantoni, A.A. Gapud, A. Goyal and D.K. Christen, *Supercond. Sci. Technol.* **19**, R23 (2006).

Superstructure phase of microwave dielectric $(Bi_{1.5}Zn_{0.5})(Ti_{1.5}Nb_{0.5})O_7$ pyrochlore

Y. Liu, R.L. Withers and T.R. Welberry

Research School of Chemistry, The Australian National University, ACT 0200, Australia

The cubic $Fd\bar{3}m$ pyrochlore $(Bi_{1.5}Zn_{0.5-\alpha})(Zn_{0.5}Nb_{1.5})O_{7-\alpha}$ (BZN) and related Bi based pyrochlores are attractive candidate materials for use in future wireless communications technology as a result of their high (and tuneable) dielectric constants and low dielectric losses in the RF/microwave frequency range coupled with their relatively low sintering temperatures. In the case of $(Bi_{1.5}Zn_{0.5})(Ti_{1.5}Nb_{0.5})O_7$ (BZTN), the continuous **G** ± <10*l*>* type diffuse streaking characteristic of the BZN-related pyrochlores has virtually condensed out to give relatively sharp **G** ± <001>* "satellite reflections" and a $P4_332$, close to a superstructure, phase of average pyrochlore unit cell dimensions. Bond valence sum considerations are used to investigate the local crystal chemistry of this BZNT phase and to derive a plausible model for the superstructure phase. The additional G ± <001>* satellite reflections are due to short range ordering of Bi and Zn ions on the *A* sites of the O'A_2 sub-structure of the pyrochlore average structure type coupled with associated strain induced structural relaxations.

1. Introduction

Bi-based pyrochlore phases such as $(Bi_{1.5}Zn_{0.5-\delta})(Zn_{0.5}Nb_{1.5})O_{7-\delta}$ (BZN) have been the subject of much recent interest as a result of their relatively low sintering temperatures and often excellent dielectric properties including electric field tuneability. The inherent disorder of these Bi-based, $A_2B_2O_7$ (or B_2O_6.O'A_2) pyrochlore systems is of some interest as it is believed to be strongly correlated with their dielectric relaxation properties [1-4]. We have recently found clear evidence (in the form of highly structured, **G** ± <10*l*>* type diffuse scattering [**G** a Bragg reflection of the underlying $Fd\bar{3}m$ average structure] observed via electron diffraction) for short range ordering of Bi and Zn metal ions on the *A* site positions of the O'A_2 sub-structure of the ideal pyrochlore structure type in the case of BZN. The local Bi/Zn compositional ordering and associated displacive disorder responsible was qualitatively interpreted via Monte Carlo modelling guided by the insights provided by a bond valence sum analysis of the average crystal structure and showed that each of the constituent O'A_4 tetrahedra making up the O'A_2 sub-structure must have O'Bi_3Zn stoichiometry [5]. This paper extends the results of our previous work to a new, Bi-based pyrochlore superstructure phase *i.e.* $(Bi_{1.5}Zn_{0.5})(Ti_{1.5}Nb_{0.5})O_7$ (BZTN).

2. Sample preparation

$(Bi_{1.5}Zn_{0.5})(Ti_{1.5}Nb_{0.5})O_7$ (BZTN) was synthesized by solid state reaction from high purity oxide starting materials. The powders were homogeneously mixed and then annealed for several days at 1050°C. Samples suitable for Transmission Electron Microscope (TEM) were prepared by the dispersion of finely ground material onto a holey carbon film. Electron Diffraction Patterns (EDP's) were obtained with a Philips EM 430 TEM.

3. Results and Discussion

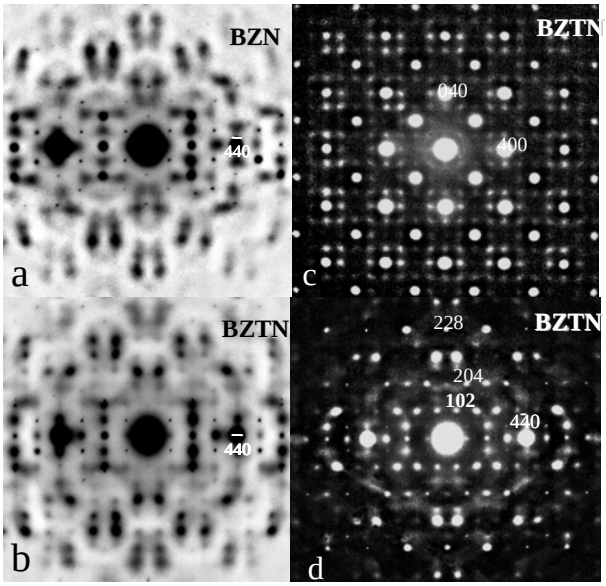

Fig.1 Typical ~ <551> zone axis EDP's of (a) BZN and (b) BZTN as well as (c) <001> and (d) <221> zone axis EDP's of BZTN.

Fig.1 shows typical ~ <551> zone axis electron diffraction patterns (EDP's) of (a) BZN and (b) BZTN as well as (c) <001> and (d) <221> zone axis EDP's of BZTN. Similar EDP's were always observed for both BZN and BZTN (*c.f.* for example Fig.1a with Fig.1b). Thus the same short range chemical ordering of the Bi and Zn ions on the ideal pyrochlore *A* site positions (along with the associated structural relaxation) must again be largely responsible for the observed structured diffuse distribution [5]. There is a difference however. The extended G ± <10*l*>* type diffuse streaking along the <001>* directions of reciprocal space in the case of BZN appear to have largely condensed into G ± <100>* 'satellite reflections' in the case of BZNT *e.g.* the 'reflection' labelled [102]* in Fig.1d = [002]* + [100]* *etc.* is not an allowed Bragg reflection of the $Fd\bar{3}m$ average pyrochlore structure type. Note that the resultant superstructure is of average pyrochlore unit cell dimensions and necessarily *P*-centred.

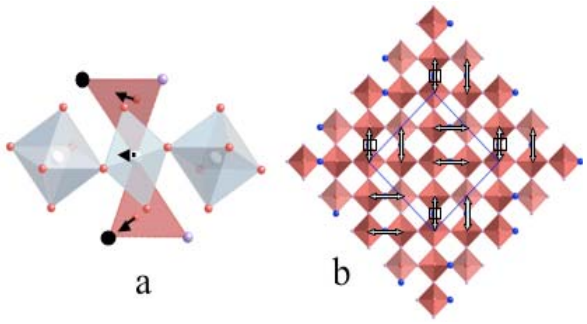

Fig.2 (a) The hexagonal prismatic environment of the *A* cations in the pyrochlore average structure type in projection along <1,-1,0> and (b) an <001> projection of the O'A_2 tetrahedral sub-structure of the ideal pyrochlore structure type. The Zn ions are represented by the larger black balls in (a) and blue balls in (b). The Bi ions are represented by the pink balls in (a) and (b). A possible Bi/Zn ordering pattern with an overall space group symmetry of $P4_332$ is shown in (b).

We begin by assuming that each O'A_4 tetrahedron of the ideal O'A_2 sub-structure (see Fig.2b) has O'Bi_3Zn stoichiometry, as is the case for BZN. Given this, here are only two possible types of inter-tetrahedral Zn-Zn separation distances. The first is of $^1/_4$ <112> type as shown in Fig.2a. Because the Zn ions are ~ 50% under-bonded in the average structure type, neighbouring O' ions centreing the O'Bi_3Zn tetrahedra must shift directly in towards the Zn ions. The Bi ions in the same tetrahedra cannot afford to lose the valence contribution from these O' ions, however, and will seek to follow the induced O' ion shifts. This induces shifts of the Bi ions perpendicular to the local O'-Bi-O' axis towards two of the six surrounding equatorial O ions (see Fig.2a). The only other possible type of inter-tetrahedral Zn-Zn separation distance is $^1/_2$ <110>. Such a Zn-Zn separation distance, however, does not allow the Bi ions to follow the O' shifts and leads to a significantly under-

bonded Bi ion. It is therefore energetically extremely unfavourable and does not occur. This provides a crystal chemical rationale for why $^1/_4$ <112> type Zn-Zn separation distances are strongly favoured and $^1/_2$ <110> type Zn-Zn separation distances completely avoided in BZN-related pyrochlores.

Applying these ordering principles and assuming a 'marker' Zn ion at $^1/_8$, $^1/_8$, $^1/_8$ (marked by the open squares in Fig.2b) there are two only Bi/Zn ordering patterns compatible with a *P*-centred resultant superstructure of average pyrochlore unit cell dimensions. The first, shown in Fig.2b above, has resultant $P4_332$ space group symmetry while the symmetry related second, has resultant $P4_132$ space group symmetry. The Zn ions are represented by the larger blue balls at the corners of the O'Bi_3Zn tetrahedra while the O'-Zn-O' "zincanyl" type units are marked by the double-headed arrows. Note that the characteristic arrangement of the O'-Zn-O' "zincanyl" type units completely destroys the original face-centreing symmetry operations of the underlying pyrochlore type average structure. Relatively extended distributions of this type must occur in the case of BZNT in order to account for the sharpness of the observed "satellite reflections" (see *e.g* Fig.1).

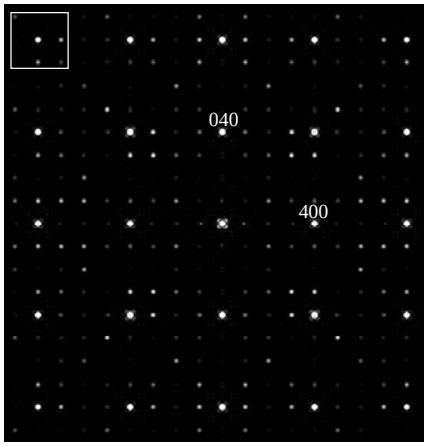

Fig.3 A Monte Carlo simulated <001> EDP based on the above model for comparison with Fig.1c.

Following the principles enunciated above, a fully ordered model structure for BZNT in space group $P4_332$, a = 10.3528 Å, has been derived. In order to confirm this, Monte Carlo simulation (see [5,6] for details) was used to produce a 'size effect' relaxed O'$Bi_{1.5}Zn_{0.5}$ distribution starting with the undistorted O'$Bi_{1.5}Zn_{0.5}$ distribution of space group symmetry $P4_332$ shown in Fig.2b. Fig.3 shows the corresponding simulated <001> type diffraction pattern using this distribution. A good qualitative agreement (*cf. e.g* the relative intensities of the satellite reflections around the [$\bar{8}$80]* pyrochlore Bragg reflection contained within the white box of Fig.3 and Fig.1c and confirms the plausibility of the proposed structural model.

Acknowledgments

YL and RLW acknowledge financial support from the Australian Research Council (ARC) in the form of an ARC Discovery Grant.

References

1. G.H. Haertling and C.E. Land, *J. Am. Ceram. Soc* **54**, 1 (1971).
2. J. Ravez and A. Simon, *Eur. Phys. J.* **AP11**, 9 (2000).
3. P. Sciau, Z. Lu, G. Galvarin, T. Roisnel and J. Ravez, *Mat. Res. Bull.* **28**, 1233 (1993).
4. H. El Alaoui-Belghiti, A. Simon, M. Elaatmani, J.M. Reau and J. Ravez, *Phys. Status Solidi B*, in press.
5. R.L. Withers, T.R. Welberry, A.-K. Larsson, Y. Liu, L. Norén, H. Rundlöf, and F.J. Brink, *J. Solid State Chem.* **177**, 231 (2004).
6. Y. Liu, R.L. Withers, T.R. Welberry, H. Wang and H. Du, *J. Solid State Chem.* **179**, 231 (2006).

Structured Diffuse Scattering and Polar Nano Regions in the $Ba(Ti_{1-x}Sn_x)O_3$ and $Ba(Ti_{1-x}Zr_x)O_3$ Relaxor Ferroelectric Systems

Yun Liu[a], Ray L. Withers[a], Xiaoyong Wei[b] and John D. Fitz Gerald[c]

[a] *Research School of Chemistry, ANU, Canberra, ACT, 0200, Australia*
[b] *Electronic Materials Research Laboratory, Xi'an Jiaotong University, Xi'an, China*
[c] *Research School of Earth Sciences, ANU, Canberra, ACT, 0200, Australia*

The observation via electron diffraction of relatively sharp, **G** ± {001}* sheets of diffuse intensity arising from the large amplitude excitation of inherently polar, transverse optical modes of distortion in $Ba(Ti_{1-x}Sn_x)O_3$ (BTS), $0.1 \leq x \leq 0.5$, and $Ba(Ti_{1-x}Zr_x)O_3$, $x = 0.3$, samples, both at room temperature as well as liquid nitrogen temperature, show that the polar nano regions (PNR's) responsible for the observed dielectric behaviour of these relaxor ferroelectric materials correspond to the same highly anisotropic <001> chain dipoles as are characteristic of the normal ferroelectric end member $BaTiO_3$ itself. The role of the dopant Sn and Zr ions is not to directly induce PNR's but rather to set up random local strain fields preventing the condensation of long wavelength homogeneous strain distortion of the unit cell thereby suppressing transverse correlations of the <001> chain dipoles and the development of long range ordered ferroelectric state/s.

1. Introduction

Early transition metal d^0 cations in octahedral environments (such as *e.g.* the Ti^{4+} ion in the TiO_6 octahedra of $BaTiO_3$, $KTiOPO_4$ *etc.* or the Nb^{5+} ion in the NbO_6 octahedra of $KNbO_3$) have a well known susceptibility to moving off-centre in a correlated fashion giving rise to inherently polar ferroelectric materials and and to paraelectric to ferroelectric phase transitions. The large peaks in dielectric constant accompanying these paraelectric to ferroelectric phase transitions are potentially very useful. A major drawback, however, is that such peaks are typically rather sharp and strongly temperature-dependent. For practical applications, it is necessary to broaden out these peaks in permittivity while still maintaining as high a magnitude as possible. The traditional way of achieving this is to chemically substitute inherently ferroelectric materials such as *e.g.* $BaTiO_3$ with appropriate dopants to give rise to so-called Relaxor Ferroelectrics (RFE's) such as $Ba(Ti_{1-x}Sn_x)O_3$ (BTS) or $Ba(Ti_{1-x}Zr_x)O_3$ (BTZ). Above a certain level of dopant ions, such relaxor systems exhibit a so-called "diffuse phase transition" (at T_m, see Fig.1 below), believed to be induced by compositional heterogeneity on the nanometer length scale, and hence maintain relatively high dielectric constants which do not vary too markedly over a much larger temperature range. The physical mechanism underlying these "diffuse phase transitions" (DPT's) has been of intense and continuing interest [1,2] ever since the pioneering work of Smolenskii [3].

2. Experimental

A series of $Ba(Ti_{1-x}Sn_x)O_3$, $x = 0.10$, 0.20, 0.25, 0.30 and 0.50 (labelled BTS10, BTS20, BTS25, BTS30, and BTS50 hereafter) powder samples as well as a $Ba(Ti_{1-x}Zr_x)O_3$, $x = 0.30$ (labelled BTZ30) powder sample were synthesized via conventional solid state reaction using reagent grade $BaCO_3$, $SrCO_3$, TiO_2 and SnO_2 or ZrO_2 as starting materials. The resultant samples were all single phase and metrically cubic. Powder samples were ground, pelleted and annealed at 1400 °C for 2h. The pellets were then polished on both sides and coated with

silver paste for dielectric measurement using a high precision LCR meter (HP4284A). Their relative density was typically > 95% while the average grain size was ~ 5-10 μm.

3. Results

3.1 Dielectric measurements

Fig.1 shows the measured temperature-dependent permittivities of the BTS10, 20, 25, 30 and 50 samples from room temperature up to 200 °C. Note the systematic lowering of T_m and the broadening of the peak in permittivity at T_m with increasing Sn content. Note also that the peak in permittivity becomes noticeably frequency dependent for x > 0.2.

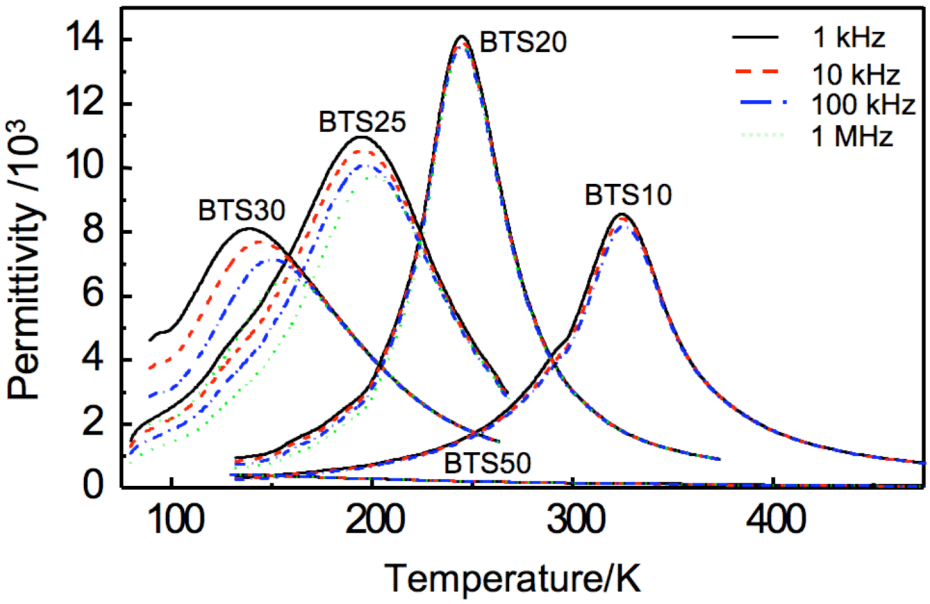

Fig. 1. Measured temperature-dependent permittivities of the BTS10, 20, 25, 30 and 50 samples from room temperature up to 200 °C.

3.2 Electron Diffraction results

Very similar structured diffuse scattering, in the form of transverse polarized, quite sharp, {001}* sheets of diffuse intensity were observed right across the BTS, x ≥ 0.1, solid solution as well as for the BTZ (x = 0.30) sample, both at room temperature as well as at low (liquid nitrogen) temperature (see Fig.2).

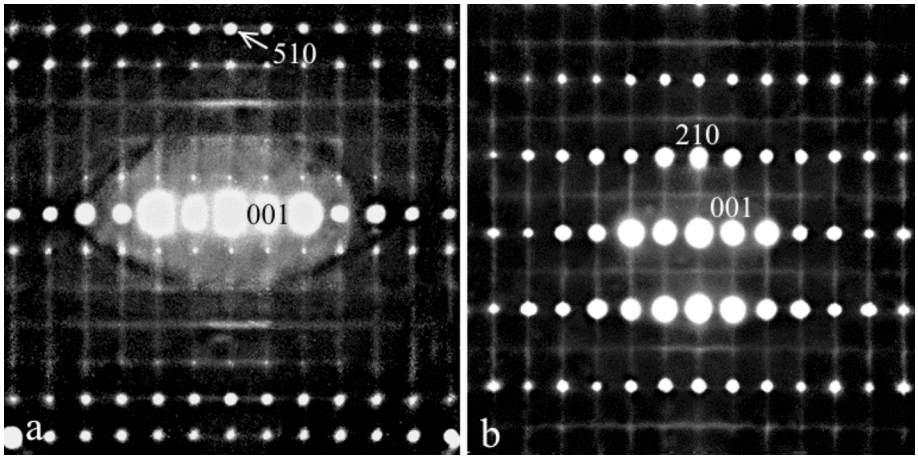

Fig. 2. (a) <-1,5,0> zone axis EDP of BTS10 at liquid nitrogen temperature.
(b) a typical <-1,2,0> zone axis EDP of BTZ30.

Note that the zero magnitude component of the individual **q** = <*hk*0>*, *h*, *k* continuous, modulation wave-vectors (constituting these {001}* sheets of diffuse intensity) along the orthogonal <001> real space directions regardless of composition, *i.e.* regardless of the Ti/Sn or Ti/Zr composition ratio rules out the possibility of Sn/Ti or Zr/Ti compositional ordering being responsible for the the observed diffuse distribution. Rather characteristic extinction conditions associated with the diffuse distribution [4,5] *e.g.* the fact that F(**G** + **q**) ~ 0 at (**G** + **q**) = [2,1, 0+□]*, [2, 1, 1+□]*, [4, 2, 0+□]* and [4, 2, 1+□]* *etc.* (see Fig.2b) require that these {001}* sheets of diffuse intensity arise from individual inherently polar, transverse optical, displacive modes of distortion giving rise to what are, in effect, 1-d PNR's (see [5] and Fig.3 below for details). Note that from the diffraction point of view, these polar displacive modes of distortion could be either static or dynamic in nature. Whether static or dynamic, however, the diffraction evidence clearly demonstrates extremely anistropic, anti-correlated behaviour of the off-centre displacements of the Ti and O ions ultimately responsible for the observed dielectric behaviour of BTS.

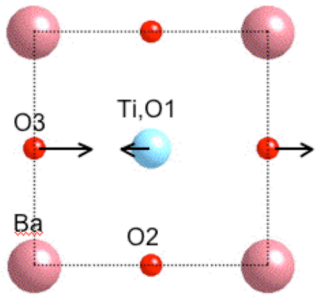

Fig. 3. Shows the 5 distinct ions per parent perovskite unit cell of BTS or BTZ: Ba at 0,0,0; $Ti_{1-x}Sn_x$ or $Ti_{1-x}Zr_x$ at $^1/_2$, $^1/_2$, $^1/_2$; O1 at $^1/_2$, $^1/_2$, 0; O2 at $^1/_2$, 0, $^1/_2$ and O3 at 0, $^1/_2$, $^1/_2$ along with the relevant inherently polar displacive shifts along <100> deduced from extinction conditions associated with the observed diffuse distribution.

The diffuse phase transitions apparent in these BTS and BTZ samples (see Fig.1) are thus clearly not a result of a DPT into a long range ordered ferroelectric state below T_m but rather are a result of a dynamic freezing or glass-like transition [1,2] involving the slowing down of the dipolar dynamics of the 1-d PNR's implied by the existence of the structured diffuse distribution. This suggests that the prime role of the dopant ions is not to introduce the PNR's. Rather the role of the dopant ions appears to be to set up random local strain fields thereby suppressing homogeneous long wavelength strain distortion of the underlying cubic lattice, the transverse correlation of the pre-existing static 1-d PNR's (below T_m) and a transition into a long range ordered ferroelectric state.

Acknowledgments

RLW and YL thank the ARC for research support in the form of an ARC Discovery Grant.

References

[1] G.Samara, *J. Phys.: Cond. Matt.* **15,** R367 (2003)
[2] A.Bokov and Z.-G.Ye, *J. Mater. Sci.* **41**, 31 (2006)
[3] G.Smolenskii, *J. Phys. Soc. Japan* **28,** 26 (1970)
[4] R.L.Withers, *Z. für Krist.* **220,** 1027 (2005)
[5] Y.Liu, Ray L.Withers, X.Wei and J.D. Fitz Gerald. *J. Solid State Chem.* **180** , 851 (2007)

Intermodulation Measurements in Electroplated Pb-Sn Superconducting Split-loop Resonators

N. R. Lobanov and D. C. Weisser

Nuclear Physics Department, Research School of Physical Sciences and Engineering, Australian National University, Canberra ACT 0200 Australia.

Measurement of the non-linear surface impedance and intermodulation distortion (IMD) was conducted on the Linac split-loop resonators (SLR). IMD measurements allow more sensitive detection of non-linearity as compared to surface impedance measurements. All cavities were electroplated with 96%Pb4%Sn film to the final thickness of 1.5 micron followed by mechanically polishing and then re-plating with a cosmetic layer of 0.3 micron. The cavities plated with this technique display a low level of intrinsic non-linearity at operating temperature of 4.3 K and nominal absorbed RF power up to 6 W. The source of the non-linearity in the resonator structure, such as magnetic flux penetration and Josephson vortex dissipation, can be located by their contribution to the non-linear IMD response above a critical RF power level.

1. Introduction

The current technologies to deposit Nb film onto copper substrate are readily applied to simple RF structures but are not feasible for complex geometries like Split Loop Resonators (SLRs) and are challenging for multistub cavities, 2- and 3-QWR and 2-, 3-HWR [1]. In contrast, Pb-Sn plating provides fast and adequate results with modest equipment and at relatively low cost. ANU used Methyl Sulfonic Acid chemistry to re-plate twelve SLRs, which were electroplated earlier with fluoboric chemistry at Oxford. This change in plating chemistry increased the energy gain by almost 100%. A detailed account of the SLR plating technology at ANU is given in ref [2].

There is renewed interest in elecroplated lead for use in a superconducting electron gun for the injector in free electron lasers [3]. This is because lead is a better electron emitter than niobium, the usually used material in superconducting RF devices.

2. Measurement surface resistance of PbSn coated SLR

The re-plating, using the hand polishing surface treatment and reverse pulse plating technique, has produced resonators with accelerating field of greater than 3.5 MV/m at 6 W during on-line test at 4.3 K. The quality factor, Q, at 6 watts is at or above 10^8 with the best resonator achieving E_{acc} about 3.9 MV/m on-line at 6 Watts.

The change in the surface resistance is given by equation $R_s+jX_s = \Gamma(Q_0^{-1} - 2j(\Delta f_0/f_0))$, where Γ = 25 Ω is the SLR's geometry factor and Δf_0 is the detuning of the cavity due to variation of surface reactance. In determination of Δf_0, the Lorentz force de-tuning of the SLR should be taken into account. In figure 1 the R_s at 4.3 K as a function of B_p is shown.

R_s was calculated from Q_0-measurement data using the equation $R_s = \Gamma Q_0^{-1}$. R_s rises up to B_p = 4 mT probably due to RF losses in the gasket. It remains constant from B_p = 4 mT up to 35 mT followed by sharp rise due to field emission (FE).

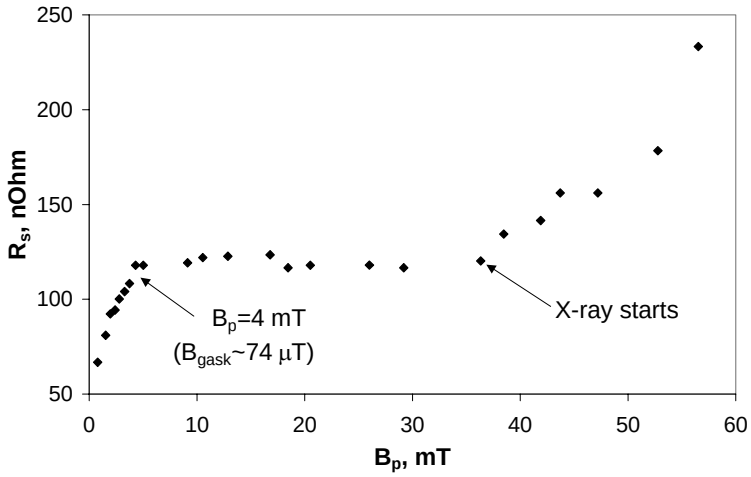

Figure 1. The surface resistance as a function of the applied microwave field at 4.3 K and 150 MHz.

3. Intermodulation distortion (IMD)

To investigate the power dependence of the non-linear microwave properties of the Pb-Sn plated SLR, the measurement of the two-tone intermodulation product as a function of the input power was performed in the same system configuration used for the single-tone experiment. Usually the IMD measurements are performed in a specialized resonator with a small sample inserted. In this work the IMD measurement is done on full-scale superconducting cavity with resonance frequency of 150 MHz.

In figure 2, the surface resistance R_s and the output power of the IMD third-order products as a function of the dissipated P_{diss} in the resonator power are presented at the reduced temperature $t = T/T_c = 0.6$. P_{diss} was calculated from the measured incident power P_{in} and the *S*-parameters S_{11} and S_{21}, $P_{diss}=P_{in}(1-S_{11}^2-S_{21}^2)$. P_{diss} and P_{in} are expressed in dBm. Dissipated power P_{diss} is proportional to the square of the peak amplitude of the RF field B_p, which is the relevant intrinsic property of superconducting coating. At very small input power the IMP signals are below the spectrum analyzer noise floor and become observable when $P_{IMD3} \geq$ -66 dBm. In figure 2, the dashed line illustrates slope 3 and solid line slope 2. The arrows indicate the threshold field $B_{ptr} \sim P^{0.5}_{diss}$ separating domains with different effects causing non-linear response in the Pb-Sn film. The B_{ptr1} and B_{ptr3} have been identified earlier from the surface resistance measurement also shown in figure 1. An operation above B_{ptr3} = 35 mT gives rise of R_s due to FE. B_{ptr1} = 4 mT probably indicates the threshold field where the RF losses in the gasket achieve their maximum value and then saturate. The RF gasket is in a region of low current density where the ratio B_{joint}/B_p does not exceed 2%. The maximum B-field in the RF joint at B_{ptr1} = 4 mT is 80 μT. An oxide layer of Pb_2O_5 is formed on the tuner plates and gasket on exposure to air. Therefore a network of Josephson junctions or weak links may form in the vicinity of the RF joints. Due to the weak links the magnetic field penetrates much more easily than into a homogeneous superconductor. At extremely low magnetic fields, the magnetic flux may penetrate into the bulk in the form of hyper-vortices [4]. The hyper-vortices movement may be responsible for low-field microwave absorption observed in numerous experiments.

As can be seen from figure 2, the frequency transformation beyond threshold field B_{ptr2} is much more dramatic than the change in R_s. IMD represents the most sensitive characterization of the intrinsic non-linear behaviour in superconducting material. At $B_p < B_{ptr2}$ the IMD products scale with respect to input power at 3:1. For B_p larger than B_{ptr2}, a sudden transition from slope 3 to slope 2 occurs. The behaviour above is similar in SLRs plated under identical conditions as described in [2].

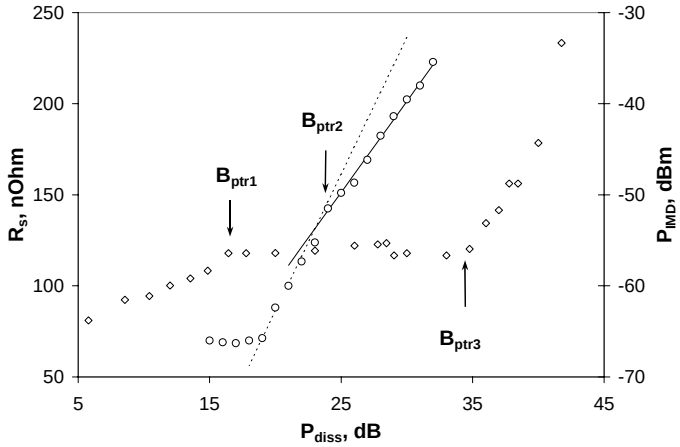

Figure 2. The surface resistance R_s (⑦) and the output power of the IMD products P_{IMD3} (⑥) as a function of the dissipated power at the reduced temperature $t=T/T_c=0.6$. Dashed line illustrates slope 3 and solid line slope 2. The arrows indicate the threshold field $B_p \sim P_{diss}^{0.5}$ separating domains with different nonlinear effects.

Using the harmonic balance algorithm, Mateu *et al* [5] have calculated the power dependence of the IMD products for the power-law nonlinearity in the different forms. These authors have found that the slope 2 of the third-order IMD may correspond to dissipation due to Abrikosov or Josephson vortex [5]. The estimated B_{ptr2} = 9 mT is significantly lower than the B_{c1} = 53 mT value estimated for 96%Pb4%Sn superconducting film. This may be explained by the fact that ANU Pb-Sn coating process involves mechanical hand polishing of the superconducting layer just before deposition of the final cosmetic layer. The mechanical polishing can damage the film and introduce voids and non-superconducting inclusions, the magnetic field can penetrate through the film at much lower field $B_{ptr2} < B_{c1}$.

4. Conclusion

The initial rise in the surface resistance of Pb-Sn films might be caused by low-field microwave absorption due to hyper-vortices movement in the Josephson medium in the vicinity of RF joints.

In low temperature superconducting materials the third-order products must increase with the third power of input main tones. In our case, the IMD slope changes to 2 above transition magnetic field B_{tr2} = 9 mT. This unconventional behaviour in our resonators upon increasing RF power might originate from a hysteresis process dominated by the creation and the irreversible motion and gradual penetration of the Josephson vortices into voids and non-superconducting inclusions introduced by mechanical polishing process.

Acknowledgments

We are grateful to technicians from Nuclear Physics Department J. Heighway, A. Muirhead, A. Cooper and H. Wallace for their important contribution of project.

References

[1] N.R. Lobanov and D.C. Weisser, *Phys. Rev. ST Accel. Beams* **9**, 042002 (2006)
[2] N.R. Lobanov and D.C. Weisser, Accomplishment of Re-plating ANU LINAC, *Proc. 11th Workshop on RF Superconductivity*, Travemunde, Germany 2003
[3] J. Smedley et al, Photoemission Properties of Lead, *Proc. European Particle Accelerators Conference*, EPAC2004, 1126 (2004)
[4] E.B. Sonin and A.K. Taganrtsev, *Supercond. Sci. Technol.* **4** 119 (1991).
[5] J. Mateu, C. Collado, O. Menendez and J. O'Callaghan, *Appl. Phys. Lett.* **82,** 97 (2003).

Control of entanglement in a closed, 3-qubit system interacting via an isotropic Heisenberg Hamiltonian

D. J. Miller

School of Physics, University of New South Wales, Sydney NSW 2052 and Centre for Time, University of Sydney NSW 2006, Australia

The time-evolution of the entanglement is studied for a closed system consisting of 3 qubits with two of the pairs of qubits interacting via an isotropic Heisenberg Hamiltonian. Even the non-interacting pair of qubits becomes entangled and can be projected onto one of the Bell states with probability one.

1. Introduction

The possibility of entanglement of physical systems is perhaps the most unexpected consequence of quantum mechanics. The advent of quantum information theory shows that entanglement is also useful [1]. Entanglement can be generated by the Heisenberg interaction between spins and this is of practical importance because the Heisenberg interaction applies to real physical systems, e.g. the controllable interaction between quantum dots, which have great potential for implementing quantum information and quantum computing schemes [1,2].

In this work we study the Heisenberg interaction between three qubits which offer advantages over two-qubit Bell states for quantum information purposes [3]. Most previous studies involving few- or many-qubits have considered thermal entanglement and imposed periodic boundary conditions. Since the aim in quantum information applications is to avoid decoherence, we consider entanglement in the ground state, rather than thermal entanglement, and avoid imposing periodic boundary conditions which are unnecessarily restrictive and physically unreasonable for few-qubit applications.

2. Isotropic Heisenberg model with inhomogeneous magnetic field

It is unnecessary to consider the anisotropic Heisenberg Hamiltonian because the anisotropy is small in practice or can be avoided [1,2]. On the other hand, inclusion of an inhomogeneous magnetic field accounts for the inhomogeneities in real sample systems as well as the likely presence of stray magnetic fields due to magnetic impurities in the sample [2]. As shown in Fig. 1, we study the case where there is no direct interaction between the spins labelled 1 and 2 and the magnetic field is non-zero on only the site labelled 3.

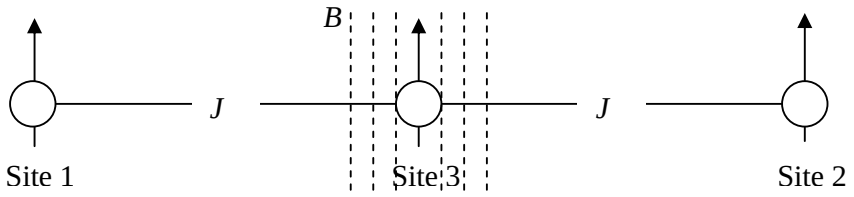

Fig. 1. Three qubits showing interaction between sites 1 and 3, and 3 and 2, and possible magnetic field at site 3.

The interaction between the 3 qubits can be described by the Hamiltonian

$$H = \frac{J}{2}(\boldsymbol{\sigma}_1 \cdot \boldsymbol{\sigma}_3 + \boldsymbol{\sigma}_3 \cdot \boldsymbol{\sigma}_2) + B\sigma_3^z \qquad (1)$$

where J and B are constants with the units of energy and the spin on site l is $\mathbf{S}_l = \boldsymbol{\sigma}_l / 2$ in units of $\hbar$. The Hamiltonian commutes with $S_1^z + S_2^z + S_3^z$ and we will be interested only in those states with total z-component of 1/2 (in units of $\hbar$). In terms of the usual notation where, for example, $|101\rangle$ represents spins on sites 1 and 3 up in the z –direction, and the spin on site 2 down in the z –direction, the relevant eigenvalues and eigenstates of the above Hamiltonian are

$$\begin{aligned} E_1 &= B & |\psi_1\rangle &= \frac{1}{\sqrt{2}}\left(|101\rangle - |011\rangle\right) \\ E_2 &= -\frac{J}{2}(y+1) & |\psi_2\rangle &= \frac{1}{\sqrt{2y\alpha}}\left[\alpha|110\rangle - 2\left(|101\rangle + |011\rangle\right)\right] \\ E_3 &= \frac{J}{2}(y-1) & |\psi_3\rangle &= \frac{1}{\sqrt{2y\beta}}\left[\beta|110\rangle + 2\left(|101\rangle + |011\rangle\right)\right] \end{aligned} \qquad (2)$$

where $y = \sqrt{4x^2 + 4x + 9}$, $x = B/J$, $\alpha = y + 2x + 1$, $\beta = y - 2x - 1$.

If the three qubits are prepared in the state $|\varphi(0)\rangle = |110\rangle$ at time t = 0, then at time t,

$$\begin{aligned} |\varphi(t)\rangle &= \frac{1}{\sqrt{2y}}\left(\sqrt{\alpha}e^{-iE_2 t/\hbar}|\psi_2\rangle + \sqrt{\beta}e^{-iE_3 t/\hbar}|\psi_3\rangle\right) \\ &= \frac{1}{2y}\left[\left(\alpha e^{-iE_2 t/\hbar} + \beta e^{-iE_3 t/\hbar}\right)|110\rangle - 2\left(e^{-iE_2 t/\hbar} - e^{-iE_3 t/\hbar}\right)\left(|101\rangle + |011\rangle\right)\right]. \end{aligned} \qquad (3)$$

3. Entanglement

The entanglement of any pair of the three qubits can be quantified by the concurrence $C(\mathrm{ij}) = \max\{\lambda_1 - \lambda_2 - \lambda_3 - \lambda_4, 0\}$ where $\{\lambda_1, \lambda_2, \lambda_3, \lambda_4\}$ are the (positive) square roots of the eigenvalues, arranged in decreasing order, of the operator $\varsigma(ij) = \rho_{ij}\left(\sigma_i^y \otimes \sigma_j^y\right)\rho^*_{ij}\left(\sigma_i^y \otimes \sigma_j^y\right)$ where $\rho_{ij} = \mathrm{Tr}_k \rho_{ijk}$ is the partial trace of the density operator of the three qubits [4]. For pure states (as considered here), the entanglement of all three qubits can be quantified by the three-tangle $\tau(ijk) = 2\left(\lambda_1^{ij}\lambda_2^{ij} + \lambda_1^{ik}\lambda_2^{ik}\right)$ where $\lambda_1^{ij}, \lambda_2^{ij}$ are the square roots of the two non-zero eigenvalues of $\varsigma(ij)$ (the other two eigenvalues being zero for pure states) [4].

The three-tangle remains zero at all times but each of the three pairs of qubits become entangled as shown by the following expressions for the concurrences

$$\begin{aligned} C(12) &= 2y^{-2}(1 - \cos\omega t) \\ C(23) &= C(12) = \sqrt{2}y^{-2}\sqrt{(1-\cos\omega t)\left(y^2 - 4(1-\cos\omega t)\right)} \\ &\text{where} \quad \omega = (E_3 - E_2)/\hbar = yJ/\hbar. \end{aligned} \qquad (4)$$

The concurrences when the magnetic field is zero are shown as a function of time in Fig. 2.

3. Production of a Bell state

It is interesting that the Bell state

$$|\Phi^+\rangle = \frac{1}{\sqrt{2}}\left(|10\rangle_{12} + |01\rangle_{12}\right) \qquad (5)$$

involving the spins on sites 1 and 2, which have no direct interaction with each other, can be produced by simply measuring the z-component of the spin on site 3 repeatedly at arbitrary time intervals until the result spin up on site 3 is obtained. This follows from Eq. (3) because

the result spin up for the spin on site 3 is obtained with probability $2y^{-2}(1-\cos\omega t)$ in which case the spins on sites 1 and 2 are projected onto the Bell state $|\Phi^+\rangle_{12}$ in Eq. (5) and they remain in that state if the controllable interaction between the qubits is turned off when the result is obtained. On the other hand if the result spin down on site 3 is obtained, the three qubits are projected onto the state $|110\rangle$ which was the original state at time $t = 0$ and so the process can be repeated until the spin at site 3 is found to be up, in which case $|\Phi^+\rangle_{13}$ is obtained as explained above.

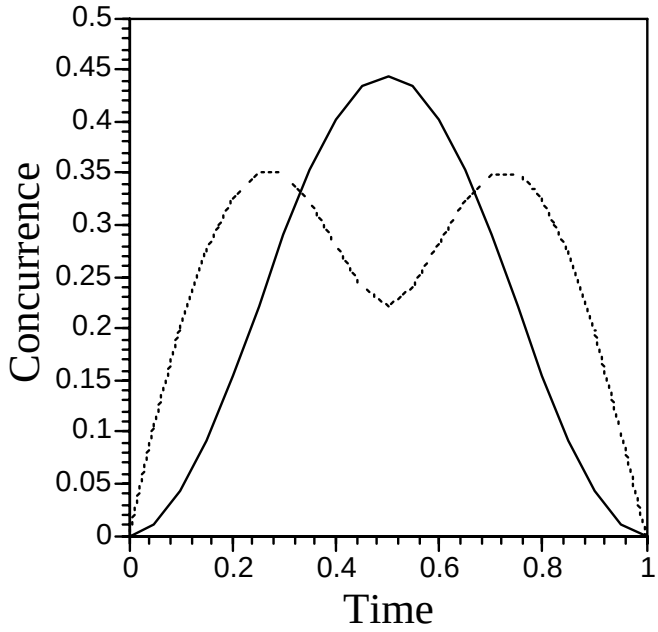

Fig. 2. The concurrence as a function of time t in units of h/yJ in the absence of the magnetic field. The full line shows the concurrence $C(12)$ of the spins on sites 1 and 2. The dotted line shows $C(13) = C(32)$.

5. Discussion and Conclusion

When two qubits (sites 1 and 2) are allowed to interact with a third qubit (site 3) via the isotropic Heisenberg interaction (Eq. (1), which includes the possibility of a magnetic field on site 3), the three qubits remain unentangled as a whole (three-tangle remains zero) but the qubits become entangled in pairs. As shown in Fig. 2 and Eq. (4), the entanglement as measured by each pairwise concurrence fluctuates in time with frequency which depends on the strength of the Heisenberg interaction J and also depends the applied magnetic field through $x = B/J$ in the term y. The magnitudes of the concurrences also depend on $x = B/J$ in the term y. The maximum concurrence for qubits 1 and 2 occurs when $B = 0$ and it is 4/9. The interaction which has been considered also provides a means of producing a Bell state involving the non-interacting qubits 1 and 2.

References

[1] D.P. DiVincenzo, D. Bacon, J. Kempe, G. Burkard and K.B. Whaley, *Nature* **408**, 339 (2000).
[2] M. Asoudeh and V. Karimipour, *Phys. Rev. A* **71**, 022308 (2005).
[3] X. Wang, H. Fu and A.I. Solomon, *J. Phys. A: Math. Gen.* **34**, 11307 (2001).
[4] V. Coffman, J. Kundu and W.K. Wooters, *Phys. Rev. A* **61**, 052306 (2000).

Te for two, II: A neutron powder diffraction study of the structure of the "Ni_3InTe_2" solid solution

L. Norén[a,1], A.K. Larsson[a] , R.L. Withers[a] and H. Rundlöf.[b]

[a] *Research School of Chemistry, the Australian National University, Canberra, ACT, 0200, Australia.*
[b] *Inst. Materialkemi, Ångströmlaboratoriet, Box 538, S-752 21 Uppsala, Sweden.*

A new phase in the Ni-In-Te ternary system that shows a gradual but systematic composition-dependent change between commensurate and incommensurate superstructures has been found. It is described in terms of a modulation of the structural motifs from the *CdI_2*, *NiAs* and *Ni_2In* structure types, all coexisting within the one compound.

1. Introduction

Many wide range non-stoichiometric $T_{1\pm x}B$ (*T* = a transition metal, *B* = a group III-VII element) solid solution phases adopt either the trigonal *P*-3*m*1, *CdI_2* or the hexagonal *$P6_3/mmc$*, *NiAs* or *Ni_2In* average structure types. All are based on a fully occupied hcp array of *B* atoms. The *T* atoms occupy equally all the octahedral sites thereof in the case of the *NiAs* or *Ni_2In* structure types while alternate octahedral *T* metal atom layers have different occupancies in the case of the *CdI_2* structure type. In the case of transition metal rich, $T_{1+x}B$ compositions, the *T* atoms also occupy an additional trigonal bipyramidal site within the hcp array of *B* atoms. In the Ni-In-Te ternary phase diagram we have previously found two solid solution ranges, SS1 and SS2 [1]. In this contribution, we report the refined crystal structures of three separate compositions within the *NiAs*-related, $T_{1\pm x}B$ SS2 solid solution phase and discuss the structures and crystal chemistry for these alloys.

2. Sample preparation

Three samples, Ni_3InTe_2 (A), $Ni_{3.12}In_{0.86}Te_{2.14}$ (B) and $Ni_{3.31}InTe_2$ (C) were made by reacting the pure elements (4N purity or better) in evacuated silica tubes at 1000 °C for 2-3 h and then quenching in water. The ingots were then pressed to pellets which were repeatedly annealed, with intermediate grinding and re-pelleting, in evacuated silica tubes at 570 °C for periods of fourteen days each. The samples were regularly checked with X-ray powder diffraction (XRPD) and were considered at equilibrium when no significant changes in their respective parent unit cells could be seen. Neutron powder diffraction patterns were recorded at Neutronforskningslaboratoriet (NFL) in Studsvik, Sweden, while electron diffraction patterns (EDPs) were recorded in-house.

3. Results

The XRPD results as well as the EDPs showed that a commensurate superstructure was present in samples B and C, with the primary modulation wave vector $\mathbf{q}^* = {}^2/_3\,\boldsymbol{c}^*$, while sample A showed an incommensurate value of $\mathbf{q}^* \sim 0.71\,\boldsymbol{c}^*$. The first order superstructure reflections were also present in the neutron powder patterns.

3.1 Samples $Ni_{3.31}InTe_2$ and $Ni_{3.12}In_{0.86}Te_2$

The refined neutron powder diffraction pattern of the 1x1x3 superstructure observed for $Ni_{3.31}InTe_2$ (*i.e.* sample **C**) is shown in Fig. 1. The refinement was done with the JANA 2000 program package.

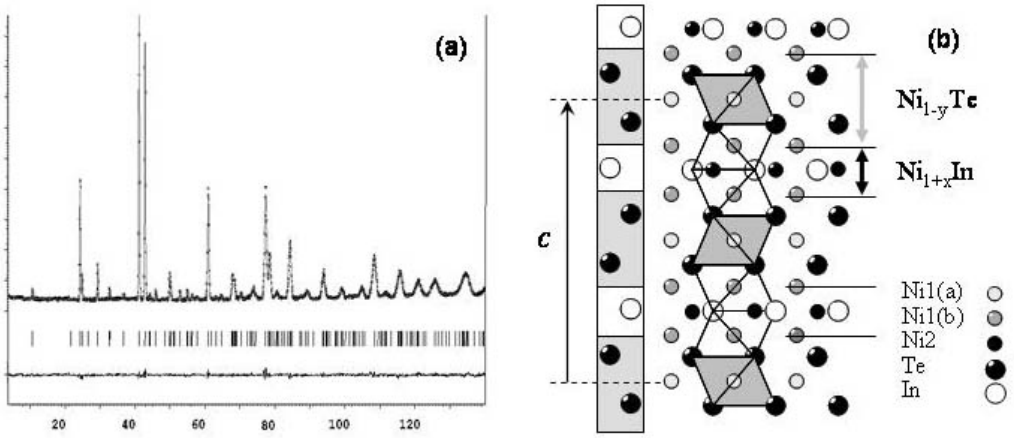

Fig. 1. (a) Refined neutron powder pattern of $.Ni_{3.31}InTe_2$ (GoF 1.21) and the obtained superstructure (b) The pure anion-motif to the far left is a simplified building block used to describe the layer stacking order in the incommensurate and the commensurate structures.

The commensurate 1x1x3 superstructures found for samples B and C can be illustrated as a regular ordering of anion layers with a "-Te/Te/In-" stacking sequence along the ***c*** direction tripling the parent ***c***-axis. Nickel atoms are inserted between these layers in two octahedral sites [Ni(1a,b)] as well as in a trigonal bipyramidal position within the In-layer [Ni(2)]. The structure can be described as composed of alternating slabs of the *Ni_2In* ($Ni_{1+x}In$) and *CdI_2* ($Ni_{1-y}Te$) structure types, the boundary between the slabs being the Ni(1b) atoms (*cf.* Fig. 1b). Note that the Ni(1a) occupancy in the Te octahedra is less than 100 % which makes this the metal-poor part of the *CdI_2* structure type. The neighbouring, fully occupied octahedra is made up of three In-atoms and three Te-atoms. Because In and Te have different sizes, it is necessary to expand the size of the In-layer in order to make it fit to the size of the adjacent Te-layer. This is achieved via the introduction of Ni(2) atoms into the trigonal bipyramidal positions within the In-layers.

3.2 Sample Ni_3InTe_2

In the incommensurately modulated Ni_3InTe_2, or sample A, the primary modulation wave vector **q*** is ~ 0.71**c*** (see Fig. 2a).

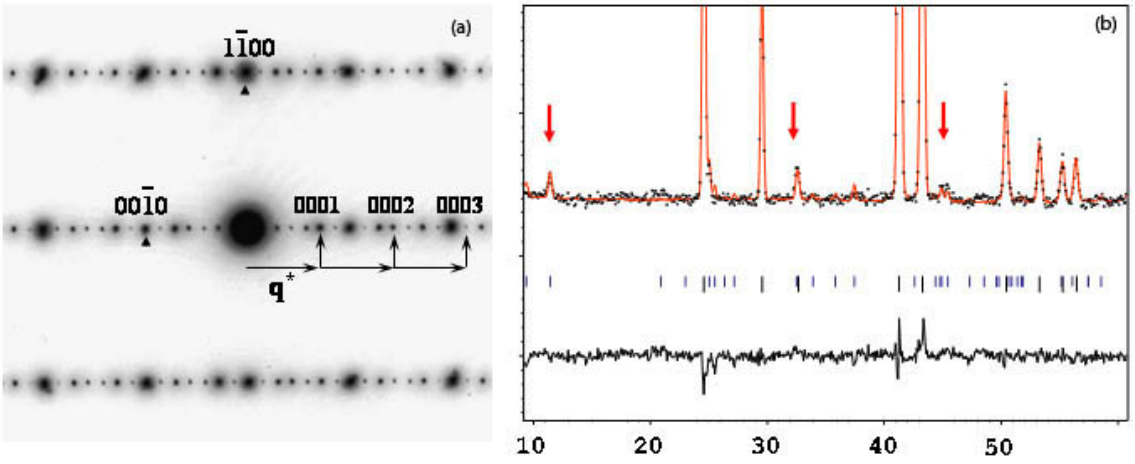

Fig. 2: <110>p zone axis EDP of Ni_3InTe_2 (a) and the Rietveld refinement using a crenel-function to describe the incommensurate modulation (b)

Satellite reflections of up to third order are clearly visible in the pattern, pointing to a 'block-like' modulation of the parent structure in real space, best described using a crenel-type modulation function [2]. In the corresponding neutron powder diffraction pattern, however, only first order harmonic satellite reflections are observed, suggesting that the modulation would be best described using a sinus function. One explanation for this apparent contradiction is that microstructural stacking faulting is present in the material, also known as "*phason wobble*". The effect of such stacking faulting is to wipe out the higher order harmonic satellite reflections in the neutron powder pattern.

The stacking sequence of the Te-rich and In-rich layers is directly related to the length of the modulation wave vector $\mathbf{q}^*$.

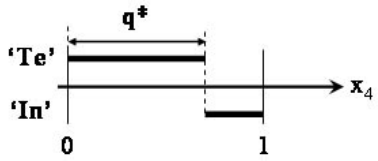

Fig. 3: An occupational crenel function drawn in hyper-space *i.e.* as a function of $x_4=\mathbf{q}^*.(\mathbf{r}+\mathbf{t})$. The width of the 'Te' occupancy domain given by $\mathbf{q}^* \sim 0.71$ and the length of the 'In' occupancy domain by $1-\mathbf{q}^*$.

In real space the repeat distance of this modulation is $\mathbf{q}$ ($= {}^1/_{\mathbf{q}^*}$) ~1.408 $\boldsymbol{c}_p$. The relative lengths of the 'Te' and 'In' parts of this repeat distance are $0.71\times1.408\ \boldsymbol{c}_p = 1\ \boldsymbol{c}_p$ and $0.29 \times 1.408\ \boldsymbol{c}_p = 0.408\ \boldsymbol{c}_p$, respectively. In the diagram below the position of the atomic layers of the parent structure is given by vertical lines, black (**thick**) for the unit cell repeat and grey (thin dashed) for the intermediate layer (*cf* Fig. 1). The "type of layer" in the stacking sequence is given by the crenel function (illustrated in grey). If a 'Te' part crosses the "layer position line" that layer is of the Te-rich CdI_2-type layers while a 'In' part means a layer of Ni_2In-type (*cf* Fig. 1b and Fig. 4).

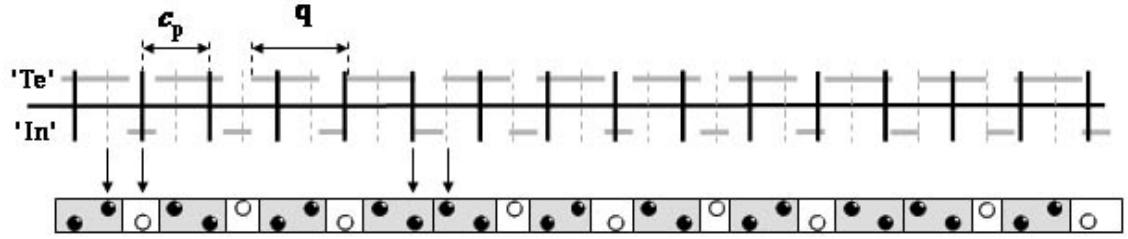

Fig. 4: As can be seen, double layers of CdI_2-type now periodically appear which did not occur in the case of the 1x1x3 superstructure (*cf.* Fig. 1b).

The result is a structure with the possibility of continuously changing the ratio of the CdI_2/ Ni_2In structural components in response to the relative composition of Ni, In and Te.

References

[1] L. Norén, R.L. Withers and F.J. Brink, *J. Alloys and Comp.* **353,** 133 (2003).
[2] V. Petříček, A. van der Lee and M. Evain, *Acta Cryst. A* **51,** 529(1995).

A Simple Ferrimagnetic Ising Model

J. Oitmaa[a] and I.G.Enting[b]

[a]*School of Physics, The University of New South Wales, Sydney, NSW 2052;*
[b]*MASCOS, The University of Melbourne, VIC 3010*

A simple mixed-spin S = (1/2,1) Ising ferrimagnet on the square lattice is studied by low and high temperature series, and by Monte Carlo simulations. The former method indicates the presence of a tricritical point and consequent region of first-order transitions, while no evidence for this is found from Monte Carlo studies. A possible explanation is that the transition is very weakly first order.

1. Introduction

Ferrimagnets are materials where different sublattices have opposing magnetic moments of unequal magnitude. Thus, unlike antiferromagnets, these materials have a net moment at low temperatures which vanishes at a critical temperature T_c. In addition, since the sublattice moments will, in general, have a different temperature dependence, there is the possibility that they may exactly cancel at some lower temperature T_{comp}, known as a **compensation point.**

Studies of ferrimagnetism in quantum models have, to date, generally used mean-field approaches, which are of questionable validity. Consequently there has been much work, in recent years, on simpler mixed-spin Ising ferrimagnets where exact or numerically accurate treatments are possible. Such a model is studied in the present work. The model, shown in Figure 1, is a bipartite square lattice with S=1/2 spins on one sublattice (A) and S=1 spins on the other (B), with nearest-neighbour interactions and a single-ion anisotropy term at the S=1 sites. The Hamiltonian is

$$H = J \sum_{<ij>} \Sigma \sigma_i \; S_j - D \sum_i \; S_i^2$$

A schematic phase diagram is also shown in Figure 1. For D/J > -4 there is a transition line separating the low-temperature ferrimagnetic phase from a high-temperature paramagnetic phase. At D/J = -4 the ferrimagnetic and S=0 ground states are degenerate, and for D/J < -4 the ground state is infinitely degenerate with no magnetic order.

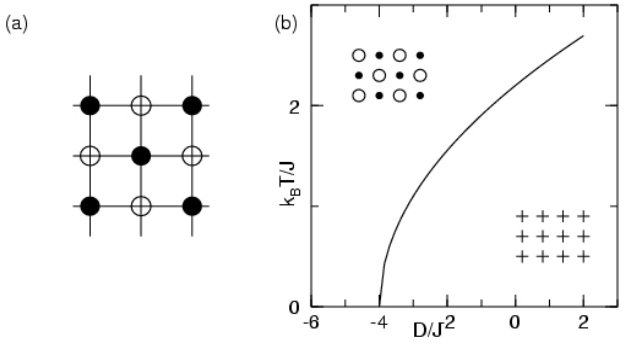

Fig. 1. The ferrimagnetic model(a), and a schematic phase diagram(b).

The mean-field phase diagram was obtained by Kaneyoshi and Chen [1], who found a compensation point for -4 < D/J < -2 ln 6 (-3.3535...). In addition they found a **tricritical point** at D/J = -3.720, and thus a first-order transition for -4 < D/J < -3.720. A more recent,

and more reliable study, using Monte Carlo and transfer matrix methods, found neither a compensation point nor a tricritical point [2].

Because of this disagreement it seemed worthwhile to study the model by another systematic approach, that of high- and low-temperature series expansions. Our result [3], to be discussed below, found no compensation point, in agreement with [2], but did find a signature of a tricritical point near D/J = -3.1. We have subsequently carried out Monte Carlo studies at D/J = -3.6, where the series clearly indicate a first-order transition. These results are presented here for the first time. Surprisingly, no indication of a first-order transition is found.

2. Series Expansions

Series expansions have, in the past, been used successfully to identify and locate first-order transitions, by matching the free energies obtained from expansions in the high- and low-temperature phases. For a second-order transition the curves should meet smoothly, while a discontinuity in slope is an indication of a first-order transition.

Our series [3] are expressed in the form

$$-\beta f_{HT} = \tfrac{1}{2} \ln 2/(1-p) + \sum_{r=2}^{\infty} A_r(p) K^r$$

$$-\beta f_{LT} = 4\beta J + \beta D + \sum_{r=2}^{\infty} \Psi_r(y) u^r$$

where $K = J/k_BT$ and $u = e^{-2K}$ are the usual high- and low-temperature expansion variables, $A_r(p)$ and $\Psi_r(y)$ are polynomials, which have been computed to orders 16 and 19 respectively, and $y = e^{-\beta D}$, $p = 2/(2+y)$.

Figure 2 shows the free energy matching procedure for various D/J. It is apparent that for D/J > -3.0 the curves meet smoothly, whereas for D/J < -3.0 there is a clear discontinuity in slope, indicating a first-order transition.

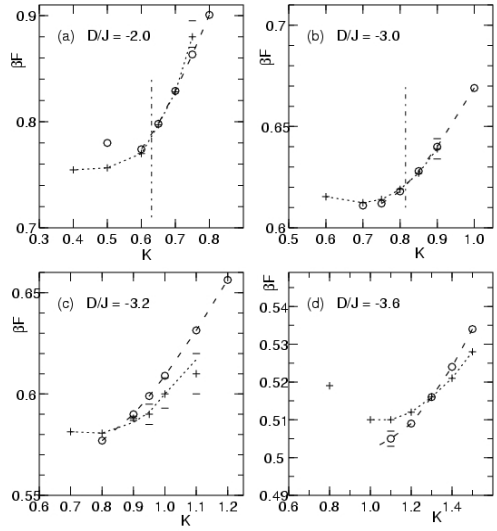

*Fig. 2. Matching of high- and low-temperature free energies for various **D/J**.*

3. Monte Carlo Simulation

In view of the discrepancy between the Monte Carlo results of [2] and our series results [3], we have carried out further Monte Carlo studies, but using the Wang-Landau method [4]. This new method is not based on Metropolis importance sampling at particular temperatures, but obtains the density of states ρ(E) directly. The canonical distribution

$P(E) = \rho(E)\exp(-E/k_BT)$ can then be obtained at any temperature, and used to compute all of the thermodynamic quantities.

We have adapted the algorithm to the present problem, and obtained the density of states for L x L lattices with L=16,24,32,48. Figure 3 shows the specific heat as a function of temperature for the four lattices for the case D/J = -3.6.

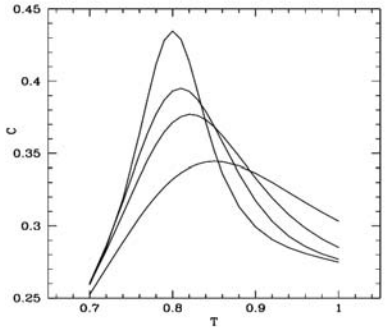

Fig. 3. Specific heat versus temperature for L x L lattices with L=16,24,32,48.

As is apparent, the specific heat peak sharpens, increases in height, and moves to lower temperatures for increasing L. This is, however, characteristic of both second- and first-order transitions, noting that a weak first-order transition can be difficult to distinguish from a true second-order transition.

The canonical probability P(E) is potentially a better discriminator of the order of the transition. For strongly first-order transitions P(E) should be double peaked at and near the transition temperature. In Figure 4 we show P(E) for the largest lattice studied, 48 x 48, at T=0.795, the temperature of the specific heat peak. There is clearly no double peak.

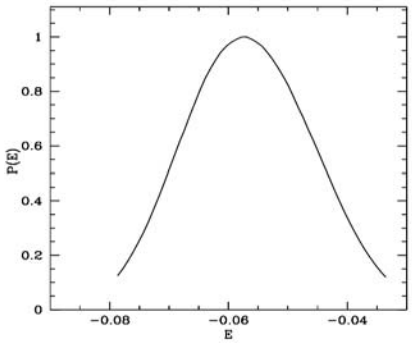

Fig. 4. Canonical probability versus energy for L = 48 at the temperature of the specific heat peak.

4. Conclusions

The series work and early and subsequent Monte Carlo studies continue to give conflicting results for the existence of a tricritical point and consequent region of first-order transitions in this simple model. A possible explanation is that the transition is very weakly first-order, and thus difficult to distinguish from a continuous transition. The puzzle remains!

Acknowledgments

Support from the Australian Research Council and from CSIRO is gratefully acknowledged.

References

[1] T. Kaneyoshi and J.C. Chen, *J. Magn. Magn. Mater*. **98**, 201 (1991).
[2] G.M. Buendia and M.A. Novotny, *J. Phys. Condens. Matter* **9**, 5951 (1997).
[3] J. Oitmaa and I.G. Enting, *J. Phys. Condens. Matter* **18**, 10932 (2006).
[4] F. Wang and D.P Landau, *Phys. Rev. E* **64**, 056101 (2001).

The Spin-1 Heisenberg Magnet with Uniaxial $(S^z)^2$ Anisotropy

J. Oitmaa, W-H. Zheng and C.J. Hamer

School of Physics, The University of New South Wales, Sydney, NSW 2052

We revisit an old problem – the phase diagram of an S = 1 Heisenberg ferromagnet or antiferromagnet with an easy axis or easy plane crystal field anisotropy. Long series expansions at T = 0 and at high temperatures are used to compute the ground state energy, sublattice magnetization and critical temperature for the easy axis antiferromagnet on the square lattice.

1. Introduction

The physics of many magnetic materials depends not only on exchange but on single ion terms arising from crystal fields. The simplest generic Hamiltonian is

$$H = -J \sum_{<ij>} \mathbf{S_i} \cdot \mathbf{S_j} - D \sum_i (S_i^z)^2$$

which, depending on the signs of J,D describes ferromagnetic or antiferromagnetic exchange, with an **easy axis** or an **easy plane**. Figure 1 represents, schematically, the types of order expected.

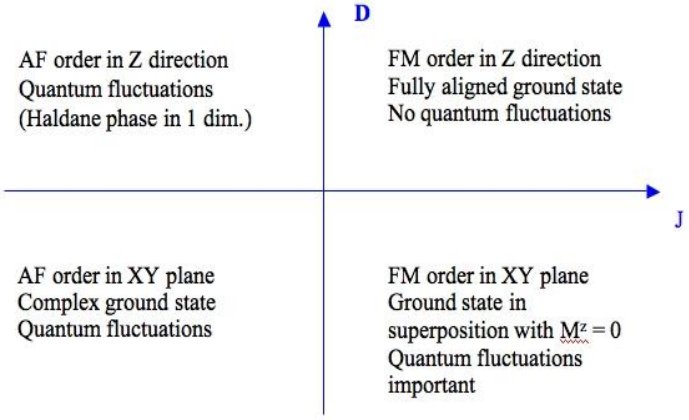

Fig. 1. Possible ground state scenarios for the J-D model.

Early studies of this kind of system were largely based on mean-field approximations [1] or Green's function decoupling schemes [2], which are of doubtful accuracy.

There has been renewed interest in such models, with S = 1, in connection with experiments on solid molecular oxygen (O_2) either in bulk or monolayers adsorbed on graphite [3]. In view of this, and in view of the availability now of accurate series expansion methods [4], we have decided to revisit this problem. In the initial study reported here, we consider the S = 1 easy axis antiferromagnet on the two-dimensional square (SQ) lattice.

2. Ground State Properties

It has been proven rigorously [5] that the S =1 antiferromagnet on the SQ lattice has long range Néel order, reduced by quantum fluctuations.

We compute 'Ising expansions' [4] to order λ^{10} by writing the Hamiltonian as $H = H_0 + \lambda V$, with

$$H_0 = J \sum_{<ij>} S^z_i S^z_j - D \sum_i (S_i^z)^2,$$

$$V = J/2 \sum_{<ij>} (S^+_i S^-_j + S^-_i S^+_j)$$

Series are computed for the ground state energy and sublattice magnetization, and evaluated at $\lambda = 1$ by standard methods.

In Figures 2 and 3 we show these quantities versus the anisotropy parameter D. For comparison we also show the same quantities as obtained from linear spin wave theory (LSWT)

$$E_0 = -2(2J+D) + 1/N \sum_k \Omega_k$$

$$M = 3/2 - 2/N \sum_k (2J+D)/\Omega_k$$

where

$$\Omega_k = 4[(J+D/2)^2 - J^2 \gamma_k^2]$$
$$\gamma_k = 1/2(\cos k_x + \cos k_y)$$

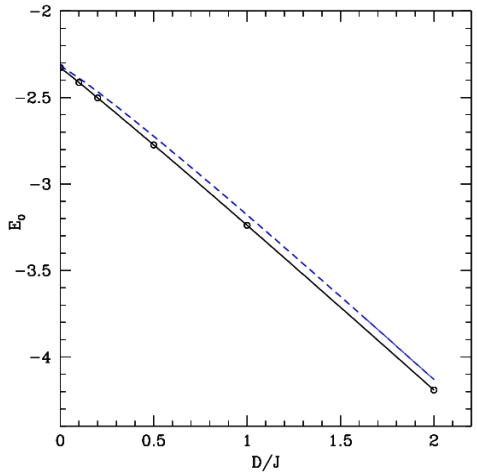

Fig.2. Ground state energy for the easy-axis antiferromagnet on the square lattice. The full line with points is the series result and the dashed line is LSWT.

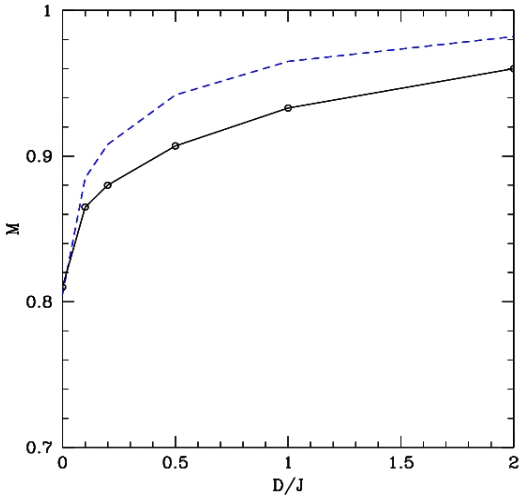

Fig. 3. Sublattice magnetization for the easy-axis antiferromagnet on the square lattice. The points and lines have the same meaning as in Fig. 2.

For D = 0 the quantum reduction in magnetization is about 20% and, as expected, this decreases with increasing D. As D $\rightarrow \infty$ the quantities approach the known Ising limits. It is evident that linear spin wave theory gives results in good agreement with these series data for the energy but overestimate the magnetization.

3. Finite Temperature Phase Transition

For D = 0 the isotropic antiferromagnet in 2 dimensions has no long range order at finite temperature (Mermin-Wagner theorem). However in the D > 0 easy-axis case the continuous symmetry of the order parameter is broken, and we expect a finite temperature transition lying in the Ising universality class.

To locate the transition line we have computed high-temperature expansions to order $(1/t)^{11}$ for the staggered susceptibility, for various values of D/J. The resulting critical line is shown in Figure 4. The critical exponent is consistent with the Ising value $\gamma = 7/4$. For comparison we show the mean-field result [1].

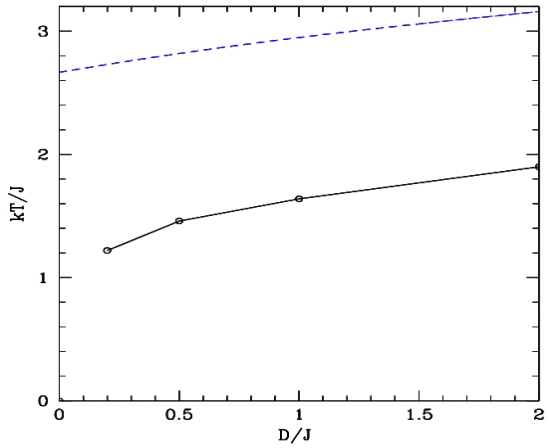

Fig. 4. Critical temperature versus anisotropy D, for the easy-axis S = 1 antiferromagnet on the square lattice. The dashed line is the mean-field result.

4. Further Work

This project is in its initial stages. We plan to continue in the following directions:

- compute the magnon excitation spectra
- consider other lattices including the frustrated triangular lattice
- investigate the more interesting (and more complex) easy-plane cases for both ferromagnetic and antiferromagnetic exchanges.

Acknowledgments

This work forms part of a research program supported by the Australian Research Council.

References

[1] M.R.H. Khajepour *et al.*, *Phys. Rev.* B**12**, 1849 (1975).
[2] J.F. Devlin, *Phys. Rev.* B**4**, 136 (1971).
[3] Y. Murakami and H. Suematsu, *Phys. Rev*. B**54**, 4146 (1996).
[4] J. Oitmaa, C.J. Hamer and W.H. Zheng, *Series Expansion Methods for Strongly Interacting Lattice Models* (Cambridge, 2006).
[5] E.J. Neves and J.F.Perez, *Phys. Lett.* A**114**, 331 (1986).

Electronic surface band structure of Cu(111) by the 2D Green's function (KKR) method

M. N. Read

School of Physics, University of New South Wales, Sydney NSW 2052, Australia.

Previous surface band calculations for Cu(111) have not produced all experimentally determined surface states for $\overline{\Gamma}$ to $\overline{M}$. Our present method produces all three states below the Fermi energy and the two between it and the vacuum level. States below the Fermi energy are qualitatively in the correct positions with respect to bulk bands. Further improvements can be made using a more accurate bulk-band potential and selvedge-layer potential.

1. Introduction

In Very Low Energy Electron Diffraction (VLEED) and other spectroscopies, features occur which have been difficult to explain but are thought to be due to a different potential at the top layer of atoms (selvedge layer) from that for atom layers in the bulk (substrate layers).

Features in the surface band structure below the vacuum level would show greatest sensitivity to surface potentials. We wish to use the 2D layer-by-layer Green's function or KKR scattering method to calculate the surface band structure below the vacuum level. This method has not been used previously.

As well as explaining surface band features below the vacuum level in terms of a scattering picture, information obtained concerning surface potentials could then be carried over to the above-vacuum energy range that is probed in VLEED.

2. Method

The layer KKR method uses a scattering picture with a muffin-tin crystal potential to map the 2D bulk band states and surface energy states/resonances. Further details are in Ref. 1. Within each atomic layer the wave function is expanded into spherical waves. Between layers where the potentials are constant, the wave function is expanded into plane waves. The scattering properties of a semi-infinite number of layers can then be combined to represent the crystal. The essential features are that each layer of scattering potential may be different and a semi-infinite number of layers are used.

When the phase change of plane waves on scattering at the surface barrier and bulk substrate is such that a standing wave can form between these regions then a long-lived energy state or resonance exists at the surface. This mechanism produces a Shockley or Rydberg surface state or resonance. A standing wave may also form between the selvedge and substrate layers. This produces a Tamm-type surface state or resonance.

3. Results

Our calculated surface band structure is shown in Fig. 1.

At $\overline{\Gamma}$ near the Fermi level E_f at 8.09 eV, and above, we produce a Shockley surface state at 0.4 eV below E_f (labelled S_0) and a Rydberg surface state at 0.822 eV below E_v (labelled S_1). S_1 is the first Rydberg state arising from scattering at the image tail of the surface barrier potential. These two surface states arise from the penetration of the 00 propagating plane wave into the vacuum region and scattering ~5 eV from the top of the surface barrier. Both S_0 and S_1 exactly coincide with the experimental value[2,3] using our surface barrier model and bulk Cu potential.[4]

At $\overline{\Gamma}$ below E_f, an s-d hybridised bulk band gap is produced centred near 4.2 eV

below E_f. A surface state is located in this gap at 4.5 eV below E_f and coincident with the lower continuum band edge. Two other surface resonances appear above this gap and 2.45 eV and 1.25 eV below E_f. All three of these surface states/resonances arise, in this scattering picture from interaction of the 00 propagating wave and six *evanescent* plane waves, which are the two sets of degenerate plane waves $(01, \bar{1}0, 1\bar{1})$ and $(10, 0\bar{1}, \bar{1}1)$. These evanescent plane waves are attenuated in real space and do not penetrate far into the bulk. The bulk termination allows for their penetration into the vacuum region to produce Shockley-type surface bands in the present model. However they are more localised at the surface than the S_0 surface state.

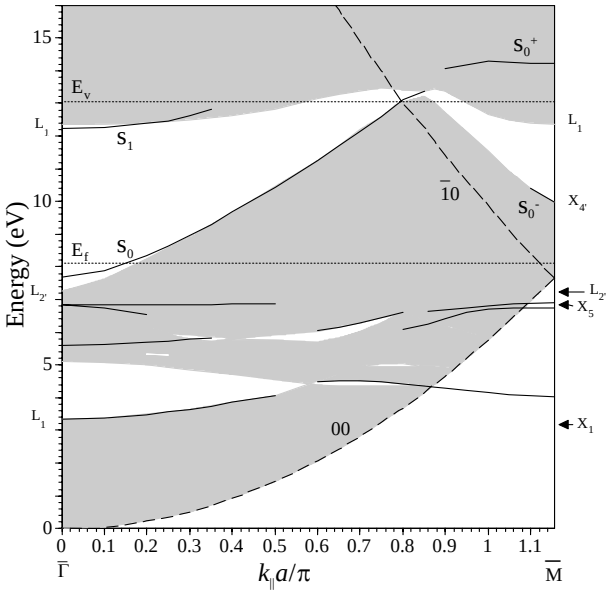

Fig. 1. Plot of the calculation of 2D band structure for Cu(111) surface from $\bar{\Gamma}$ to $\bar{M}$ using the Moruzzi et al Cu potential[4] and bulk termination with a surface barrier at image-plane position z_0 = -2.2 a.u. and cubic polynomial saturation[3]. Unshaded regions indicate surface–projected bulk-band gaps from this calculation. Full lines are the energies of surface bands from this calculation. E_f is the Fermi level and E_v is the vacuum level. Other symbols on the energy axis indicate various relevant bulk bands and their energy positions as given in Ref. 4. The dashed lines show the energies at which the indicated plane waves become propagating in the crystal surface for different parallel wave vectors, $k_\parallel$. The lattice constant is *a*.

Experimentally a surface state has been detected at 5.25 ± 0.03 eV below E_f at $\bar{\Gamma}$ and coincident with the lower edge of the s-d gap using high-resolution ARPES (angle-resolved photoemission spectroscopy)[5].

A calculation for Pd(111) surface using a mixed-basis pseudopotential method[6] and a more recent calculation using a nonlocal density-functional calculation[7] also produce a surface state in the s-d gap at $\bar{\Gamma}$ and two resonances at high energies in the bulk band continuum. There are only two comprehensive band calculations for Cu(111)[8,9] and neither have produced the d-like surface state in the s-d gap at $\bar{\Gamma}$. It has been suggested[10] that this is because they are finite slab calculations, and because of its proximity to the bulk band edge, it cannot be distinguished in these cases. S_0 is predicted in Ref. 9 only.

At $\bar{M}$ above E_f, we produce two Shockley surface bands S_0^-, near 2 eV above E_f and S_0^+, near 6.1 eV above E_f. These bands arise from interaction of the propagating 00 and $\bar{1}0$ plane waves scattering at the mid-point energy of the surface barrier. These waves become propagating at 7.6 eV. The S_0^- band energy agrees with experiment from inverse photoemission[2,3] for our surface barrier model and bulk Cu potential.[4] S_0^+ has not been identified from experiment as yet and has not been previously predicted from theory.

At $\bar{M}$ below E_f, the energy location of the d-band continuum is not directly produced in our calculation due to it involving evanescent waves that do not satisfy flux conservation. Inspection of the bulk calculation[4] puts the edges at X_5 = 6.77 and X_1 = 3.13 eV with a band gap between X_5 and $L_{2'}$ at 7.25 eV. We produce a surface state at 6.91 eV in the small s-p band gap and 0.14 eV above the d-band continuum and dispersing downwards towards $\bar{\Gamma}$. Two surface resonances at 4.03 and 6.74 eV are within the d-band continuum. All of these

surface bands arise from interaction of eight evanescent plane waves. Again these evanescent waves leak into the vacuum region to produce very localised surface bands of the Shockley type in the present model.

Experimentally a surface state has been detected at ~1.95 eV below E_f at $\overline{\mathrm{M}}$, ~0.2 eV above the d-band continuum and dispersing downward towards $\overline{\Gamma}$.[11,12]

The two calculations for Pd(111)[6,7] do not reproduce the experimentally determined surface state at $\overline{\mathrm{M}}$ about 1 eV below E_f. Of the two other comprehensive calculations of surface band structure for Cu(111)[8,9], one[8] produces the surface state at $\overline{\mathrm{M}}$ at 0.3 eV above the d-band continuum and neither produces the S_0^- state.

4. Conclusion

We have been able to reproduce all three surface states of Cu(111) below the Fermi energy that have been found experimentally[5, 11,12] and those above it[2,3]. The other two previous comprehensive calculations[8,9] have not produced all these surface states.

Two of the surface states that are highly localised at the surface are only produced in our calculation from the inclusion of evanescent plane waves.

Our surface states below the Fermi level are qualitatively in the correct position with respect to bulk bands but are not at the correct absolute energies.

One reason is that the Moruzzi potential places the bulk d-band manifold at 0.6 eV higher than the experimental determination.[4] In particular the position of the X_5 bulk d-band is critical for determining the position of the surface state at $\overline{\mathrm{M}}$ below E_f. We find that the bulk band calculation of Burdick[13] places the X_5 d-band in agreement with experiment[14]. Thus we intend to repeat the calculation with this Cu bulk potential.

Another reason for quantitative difference with experiment is that we have abruptly terminated the bulk potential whereas one would expect the top layer to be different. This layer is expected to have approximately 10% d-band narrowing (due to reduced atomic co-ordination) and d-band shifts of 0.4 to 0.6 eV with respect to bulk bands.[15,8] We intend to incorporate this selvedge potential into further calculations.

The fact that the method used here reproduces all the experimentally identified surface states at least qualitatively demonstrates that the method has use in studying the formation of surface bands and details of the surface potentials.

References

1. M.N. Read and A.S. Christopoulos, *Phys Rev B* **45**, 13729 (1992).
2. N.V. Smith, C.T. Chen and M. Weinert, *Phys Rev B* **40**, 7565 (1989).
3. M. Grass, J. Braun, G. Borstel, R. Schneider, H. Durr, Th. Fauster and V. Dose, *J. Phys.: Condens. Matter* **5**, 599 (1993).
4. V.L. Moruzzi, J.F. Janak and A.R. Williams, *Calculated Electronic Properties of Metals*, (Pergamon Press, New York, 1978) p 96.
5. S.G. Louie, P. Thiry, R. Pinchaux, Y. Petroff, D. Chandesris and J. Lecante, *Phys Rev Lett.* **44**, 1782 (1980).
6. S.G. Louie, *Phys Rev Lett.* **40**, 1525 (1978).
7. M. Heinrichsmeier, A. Fleszar, W. Hanke and A.G. Eguiluz, *Phys Rev B* **57**, 14974 (1998).
8. A. Euceda, D.M. Bylander and L. Kleinman *Phys Rev B* **27**, 659 (1983).
9. D.G. Dempsey and L. Kleinman, *Phys Rev B* **16**, 5356 (1977).
10. S.D. Kevan, N.G. Stoffel and N.V. Smith, *Phys Rev B* **31**, 3348 (1985).
11. P. Heimann, J. Hermanson and H. Miosaga, *Phys Rev B* **20**, 3059 (1979).
12. R. Matzdorf and A. Goldmann, *Surf. Science* **359**, 77 (1996).
13. G.A. Burdick, *Phys Rev* **129**, 138 (1963).
14. R. Courths and S. Hufner, *Physics Reports* **112**, 53 (1984).
15. J.A. Appelbaum and D.R. Hamann, *Solid State Commun*. **27**, 881 (1978).

The magnetic environment of the rare earth site in RT_2Si_2 compounds (R = rare earth, T = Cr & Mn)

B. Saensunon[a], K. Nishimura[b] and G.A. Stewart[a,]

[a] *School of Physical, Environmental and Mathematical Sciences, University of New South Wales, Canberra 2600, Australia.*
[b] *Faculties of Engineering and Science, Toyama University, Toyama, Japan.*

Specific heat measurements and ^{169}Tm Mössbauer spectroscopy demonstrate that the R sub-lattice in $ErMn_2Si_2$, $ErCr_2Si_2$, $TmMn_2Si_2$ and $TmCr_2Si_2$ is not influenced by the Mn or Cr sub-lattice magnetisation and orders independently close to liquid helium temperature with T_C = 4.6 K, 1.9 K, 6.8 K and <2.7 K respectively.

1. Introduction

The intermetallic compounds RT_2Si_2 (R = rare earth, T = extensive set of 3d transition metal elements) form with the body centred tetragonal, $ThCr_2Si_2$ prototype structure (space group #139, I4/mmm). A systematic study of the crystal field (CF) acting at the R sites in this series has so far been directed at T = Cu, Ni, Co and Fe ([1] and references therein). It was planned to extend the study to include T = Cr and Mn. However, for these compounds the T sub-lattice is reported to order antiferromagnetically well above room temperature [2, 3] and the R sub-lattice ordering temperatures are not well known. It is important that the CF study is not confused by any magnetic fields acting at the R site. In this work specific heat measurements, which are very sensitive to low temperature magnetic transitions, and ^{169}Tm Mössbauer spectroscopy have been employed to verify that the R sub-lattice orders independently close to liquid helium temperature and that the R-site is not perturbed by the Mn or Cr sub-lattice magnetisation.

2. Specimen preparation

Polycrystalline specimens of $ErMn_2Si_2$, $ErCr_2Si_2$, $TmMn_2Si_2$ and $TmCr_2Si_2$ were prepared from the elements by argon arc melting at least 6 times to achieve homogeneity. The starting metal impurities were 99.99 % for Mn, Cr and Si and 99.9 % for Tm and Er. The specimens with T = Cr were also vacuum-annealed in Ta foil at 800 °C for 6 days.

The x-ray powder diffraction patterns were recorded using Cu K_α radiation and

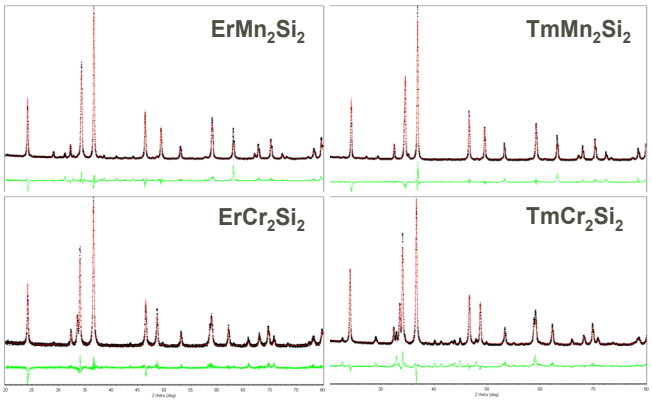

Fig. 1. X-ray diffraction patterns for $ErMn_2Si_2$, $ErCr_2Si_2$, $TmMn_2Si_2$ and $TmCr_2Si_2$

calibrated against silicon powder. Rietveld analyses were performed using *Rietica* [4]. All four specimens were predominantly single phase with lattice parameters in good agreement with literature values (see Table 1). Small concentrations of R_2O_3 were found in all specimens and $TmSi_2$ was identified only in $TmMn_2Si_2$. Some further unidentified diffraction lines were present in the pattern for $TmCr_2Si_2$. The presence of these impurities in such small amounts (e.g. < 0.5 wt% Tm associated with $TmSi_2$ in $TmCr_2Si_2$) is unlikely to contribute noticeably to the specific heat signal or the Mössbauer spectra.

3. Results

3.1 Specific heat

The specific heat measurements (Fig. 2) were carried out at Toyoma University, Japan using the relaxation method on a Quantum Design PPMS. The Curie temperatures shown in Fig. 2 have been taken as the points of greatest rate of change in specific heat. The more complex nature of the data for the Tm-based intermetallics may be associated with low-lying singlet states of the CF scheme for the non-Kramers Tm^{3+} ion. It is not clear if the broad low temperature feature observed for $TmCr_2Si_2$ corresponds to a magnetic transition. For this reason, preliminary ^{169}Tm Mössbauer spectra were recorded for this compound.

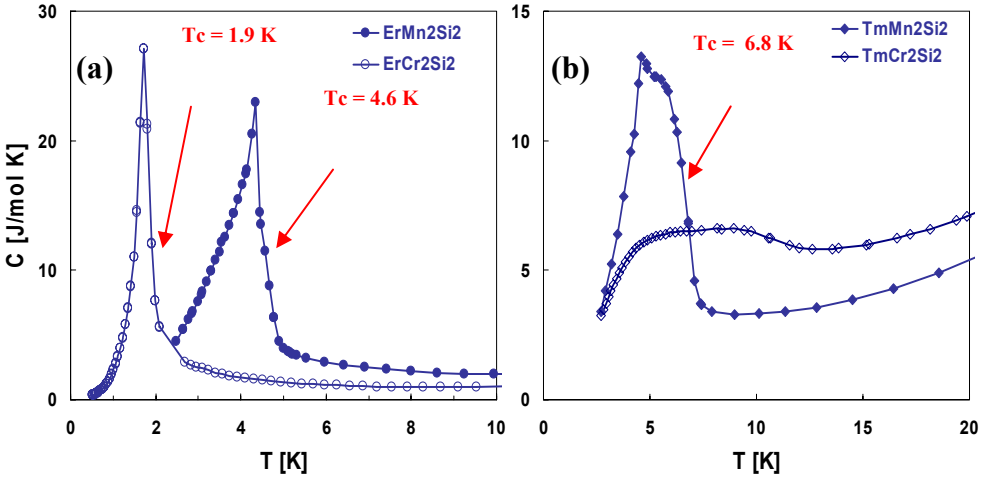

Fig. 2. Specific heat data for (a) $ErMn_2Si2$ & $ErCr_2Si_2$ and (b) $TmMn_2Si_2$ & $TmCr_2Si_2$.

3.2 ^{169}Tm Mössbauer spectroscopy

The ^{169}Tm Mössbauer spectra (Fig. 3) were recorded with the $TmCr_2Si_2$ absorber (≈ 8 mg cm^{-2} specimen material) mounted in a transmission geometry cryostat. The source was a

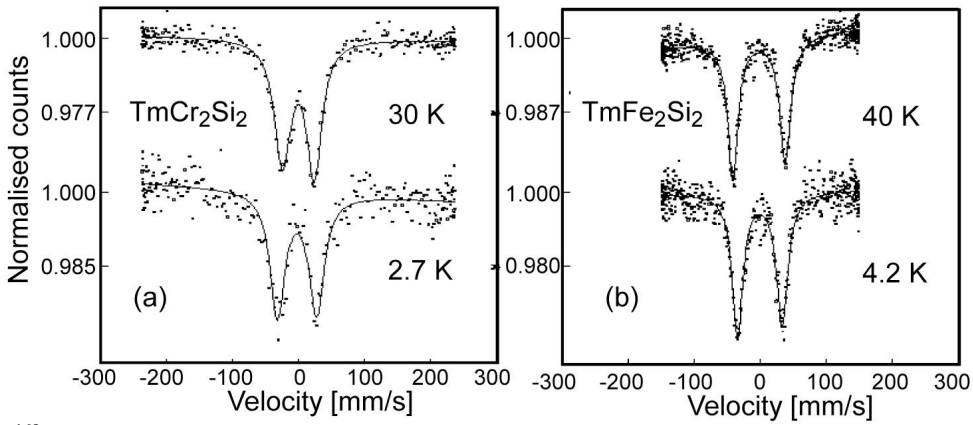

Fig. 3. ^{169}Tm Mössbauer spectra for (a) $TmCr_2Si_2$ at 2.7 K and 30 K and (b) $TmFe_2Si_2$ at 4.2 K and 40 K

neutron activated foil of ^{169}Er:$^{168}ErAl_9$ mounted outside the cryostat on a transducer which was moved with sinusoidal motion and calibrated against a standard TmF_3 absorber at 4.2 K. The spectra for $TmCr_2Si_2$ exhibit no magnetic splitting down to 2.7 K and the line half-widths at 2.7 K (≈ 14.0 mm/s) and 30 K (≈ 13.9 mm/s) are comparable. This indicates that $T_C < 2.7$ K and rules out magnetic line broadening at these temperatures. The line-widths for the $TmCr_2Si_2$ spectra are also comparable to those for $TmFe_2Si_2$ spectra where the Fe sub-lattice is known not to order magnetically, at least down to liquid helium temperature.

Table 1. Lattice parameters and T_C for Er Mn_2Si_2, $ErCr_2Si_2$, $TmMn_2Si_2$ and $TmCr_2Si_2$

Compound	a [nm]	c [nm]	Ref	T_N [K]	Method	Ref
$ErMn_2Si_2$	0.3895(1)	1.0410(1)	This work	4.6	Specific heat	This work
	0.3920(3)	1.0456(1)	[5]	5	Magnetic susceptibility	[6]
$ErCr_2Si_2$	0.3888(3)	1.0617(5)	This work	1.9	Specific heat	This work
	0.3889(1)	1.0614(1)	[7]	2.4	Neutron diffraction	[3]
$TmMn_2Si_2$	0.3886(1)	1.0404(1)	This work	6.8	Specific heat	This work
	0.3887(1)	1.0398(1)	[6]	6.5	Magnetic susceptibility	[6]
$TmCr_2Si_2$	0.3871(1)	1.0617(5)	This work	<2.7	^{169}Tm Mössbauer	This work

Conclusion

For three of the compounds, the R sub-lattice orders magnetically close to liquid helium temperature. Preliminary Mössbauer spectroscopy measurements for the fourth compound, $TmCr_2Si_2$, demonstrate that the ^{169}Tm nucleus is not subject to significant magnetic broadening or transferred hyperfine fields down to 2.7 K. On the basis of these results, we will proceed with the planned ^{169}Tm Mössbauer spectroscopy and inelastic neutron scattering studies of the CF interaction at the R site in RT_2Si_2 (T = Mn, Cr).

Acknowledgements

This project was supported by AINSE Grant 06/165. Banchachit Saensunon gratefully acknowledges the Royal Thai Army for his scholarship. Vernon Edge and Wayne Hutchison are thanked for their assistance with specimen preparation.

References

[1] S.J. Harker et al., *J. Alloys Compd.* **402**, 17 (2005).
[2] M. Hofmann et al., *J. Magn. Magn. Mater.* **176**, 279 (1997).
[3] O. Moze et al., *Eur. Phys. J. B* **36,** 511 (2003).
[4] B.A. Hunter and C.J. Howard, *Rietica*. 2000 [available from: www.ccp14.ac.uk.]
[5] J. Leciejewicz, S. Siek and A. Szytula, *J. Magn. Magn. Mater.* **40,** 265 (1984).
[6] S. Okada et al., *J. Crystal Growth* **244**, 267 (2002).
[7] A. Dommann, F. Hulliger and C. Baerlocher, *J. Less-Common Met.* **138**, 113 (1988).

Preparation of orthorhombic phase $YbMnO_3$ and $Yb_{2/3}Ca_{1/3}MnO_3$

H. A. Salama[a], D. Scott[b] , J. B. Taboada[c], N. Strickland[d] , H. O'Neill[b] & G. A. Stewart[a]

[a] School of PEMS, UNSW@ADFA Canberra, Australia 2600
[b] Research School of Earth Sciences, ANU Canberra, Australia 0200
[c] DelftChemTech, T. U. Delft, 2628 BL Delft, The Netherlands,
[d]Industrial Research Ltd, Lower Hutt 5040, New Zealand

The orthorhombic manganite phases o-$YbMnO_3$ and o-$Yb_{2/3}Ca_{1/3}MnO_3$ are obtained through reconstructive transformation at high pressure (3.5 GPa) from material prepared by conventional solid reaction. ^{57}Fe-Mössbauer spectra for o-$YbMnO_3$ are compared with those recorded earlier for the hexagonal phase h-$YbMnO_3$.

1. Introduction

The discovery of colossal magnetic resistance for the generic $La_{2/3}Ca_{1/3}MnO_3$ has led to renewed interest in the magnetic properties of all orthorhombic manganites. With decreasing average ionic radius $\langle r_{R\text{-}Ca} \rangle$ the Curie temperature for $R_{2/3}Ca_{1/3}MnO_3$ (R = rare earth) decreases and eventually the low temperature ferromagnetic-metallic phase is replaced by an insulating phase. For the undoped manganites $RMnO_3$, the Néel temperature undergoes a similar decrease with decreasing $\langle r_R \rangle$ and the low temperature magnetic structures often involve complex multiferroic behaviour.

We plan to use ^{57}Fe-Mössbauer spectroscopy to probe the low temperature magnetic structure in both o-$YbMnO_3$ and o-$Yb_{2/3}Ca_{1/3}MnO_3$. For this purpose 0.5 at % ^{57}Fe will be introduced into the Mn sub-lattices. However, at ambient pressure, both of these manganites form with the hexagonal $P6_3cm$ structure (rather than orthorhombic *Pnma*) in accordance with our proposed structural phase diagram (Figure 1). This contribution will first describe our efforts to produce o-$YbMnO_3$ and o-$Yb_{2/3}Ca_{1/3}MnO_3$ using three different approaches. Preliminary ^{57}Fe-Mössbauer spectra will then be presented for the orthorhombic phase specimen o-$YbMnO_3$ and compared with those recorded earlier for hexagonal h-$YbMnO_3$.

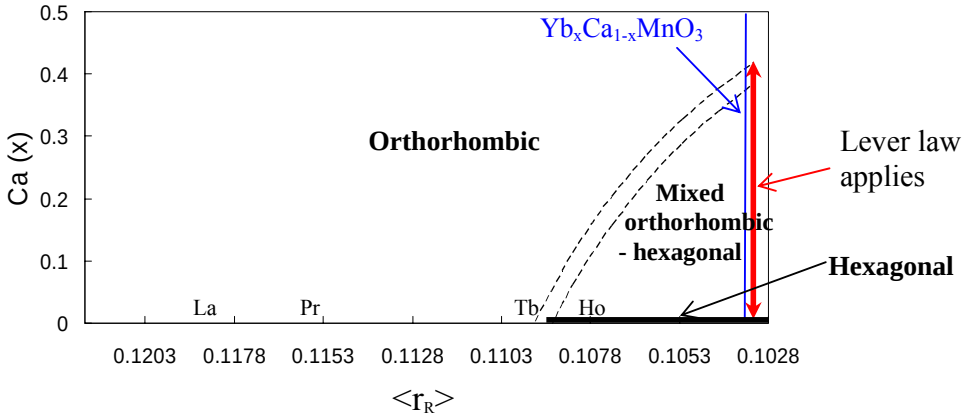

Fig. 1: Structural phase diagram for $R_{1-x}Ca_xMnO_3$. The broken lines indicate the likely orthorhombic phase -mixed phase boundary region based on average radii $\langle r_{R\text{-}Ca} \rangle$.

2. Sample preparation

2.1 Conventional solid state reaction with 6 MPa (60 bar) O_2

The specimen with nominal stoichiometry $Yb_{2/3}Ca_{1/3}MnO_3$ was prepared in air by conventional solid state reaction and observed to form as a mix of 16.3 wt% h-$YbMnO_3$ and 83.6 wt% o-$Yb_{0.6}Ca_{0.4}MnO_3$. This material was then annealed under 6 MPa O_2 at 1000°C for a further 12 hours. However, this treatment did not result in any significant conversion of the phase mixture to o-$Yb_{2/3}Ca_{1/3}MnO_3$.

2.1 Hydrothermal synthesis at approximately 3.9 MPa (39 bar)

The undoped o-$HoMnO_3$ and o-$DyMnO_3$ manganites have been prepared elsewhere by Wang *et al*. using this method [1] so we decided to test this method for the two Yb-based compounds. Our syntheses were performed in 50 mℓ, Teflon-lined, stainless steel, rotating autoclaves which were filled to 70% of their capacity. First the Yb_2O_3 (together with $CaCO_3$ when appropriate) was dissolved in 0.1 M HNO_3 at 50°C with constant stirring to form a clear solution. Next $KMnO_4$ and $MnCl_2$-$4H_2O$ were mixed in distilled water and sufficient KOH was added to maintain alkalinity. Finally the two solutions were placed in the sealed autoclave and reacted at 250°C under autogenous pressure. Efforts to prepare o-$YbMnO_3$ (at ADFA over 1 d) and o-$Yb_{2/3}Ca_{1/3}MnO_3$ (at DelftChemTech over 4 d) failed to produce orthorhombic phase specimens, most likely because the pressure was not high enough. The pressure of water vapour in equilibrium with water at 250 °C is estimated at 3.9 MPa (39 bar). The earlier preparations of o-$HoMnO_3$ and o-$DyMnO_3$ were probably accomplished at this lower pressure because they are positioned much closer to the phase boundary of Fig.1. Nevertheless, a positive outcome from this work was that the hydrothermal reaction proved to be an efficient approach for the preparation of h-$YbMnO_3$ when compared with conventional solid state reaction.

2.3 High pressure synthesis at 3.5 GPa (35 kbar)

Undoped o-$YbMnO_3$ has recently been prepared elsewhere by Huang *et al.* [2, 3] using this approach. In our case, samples of nominal stoichiometry $Yb_{2/3}Ca_{1/3}MnO_3$ and $YbMnO_3$ were first prepared by conventional solid state reaction. Up to 250 mg of a powdered specimen was then sealed (by welding) in a platinum capsule and assembled into a hydraulic press. The specimen material was maintained at 3.5 GPa (35 kbar) and 1100°C for 10 h. While still at maximum pressure, the heating current was switched off, with the specimen temperature falling 400°C within 5 seconds. X-ray powder diffraction patterns for the resultant o-$YbMnO_3$ and o-$Yb_{2/3}Ca_{1/3}MnO_3$ are shown in Fig. 2. In each case the line positions are compatible with those of a single-phase, orthorhombic perovskite specimen. The mismatch of some of the individual line intensities may be associated with effects resulting from the rapid quench, such as strain, preferred alignment or stacking faulting.

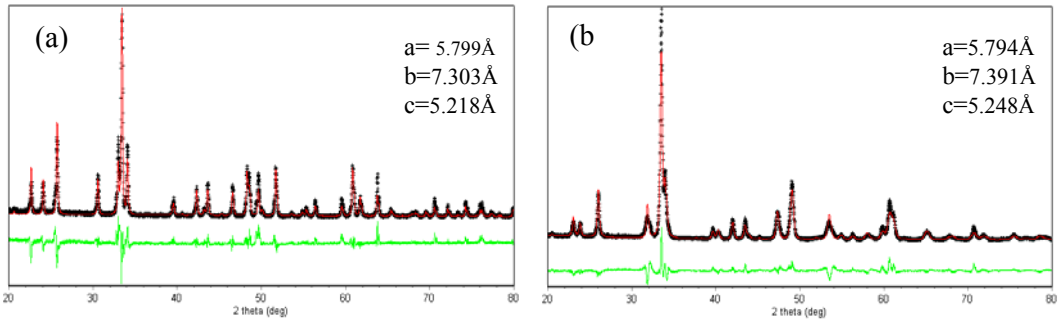

Fig.2: X-ray diffraction patterns for (a) o-$YbMnO_3$ and (b) o-$Yb_{2/3}Ca_{1/3}MnO_3$ prepared at 3.5 GPa.

3. ^{57}Fe Mössbauer spectroscopy results

Preliminary ^{57}Fe Mössbauer spectra were recorded for an o-$YbMnO_3$ specimen in which the Mn sub-lattice had been doped with 0.5% ^{57}Fe. These spectra are presented in Fig. 3 together with those recorded earlier for h-$YbMnO_3$. Compared with h-$YbMnO_3$, the isomer shift for o-$YbMnO_3$ is more positive, implying a slightly smaller electron density at the ^{57}Fe probe nucleus. The quadrupole interaction is of similar magnitude but opposite sign. The saturation magnetic hyperfine field, B_{hf}, is about 6% smaller. Most significantly, B_{hf} is inclined at an angle of ≈42° (rather than 90°) with respect to the principal z-axis of the electric field gradient (Table 1).

Table 1: Parameters fitted to the ^{57}Fe Mössbauer spectra recorded for h-$YbMnO_3$ and o-$YbMnO_3$

T [K]	Phase	$\delta_{\alpha\text{-Fe}}$ [mm/s]	Γ [mm/s]	$eQV_{zz}/2$ [mm/s]	B_{hf} [T]	θ [°]
300	h	0.292	0.339	-1.68		
	o	0.357	0.341	+1.56		
4.2	h	0.420	0.389	-1.60	47.1	90
	o	0.487	0.445	+1.79	44.3	41.8

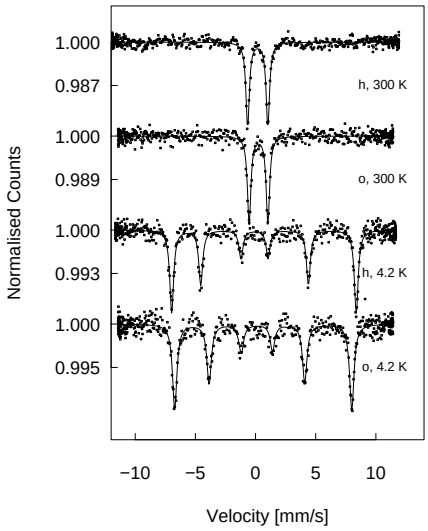

Fig.3: ^{57}Fe Mössbauer spectra recorded for h-$YbMnO_3$ and o-$YbMnO_3$

Conclusion

Following the example of Huang *et al* [2], the orthorhombic specimens have been successfully prepared at the high pressure of 3.5 GPa. The solid state reaction under 6 MPa O_2 and the hydrothermal syntheses were not successful, presumably because the pressures achieved were too small. However, the hydrothermal reaction proved much more efficient for the preparation of ambient pressure phases (compared with the tedious conventional solid state reaction). In future work, the ^{57}Fe Mössbauer investigation of o-$YbMnO_3$ will be continued as a function of temperature and then extended to o-$Yb_{2/3}Ca_{1/3}MnO_3$.

Acknowledgments

We are grateful for Vernon Edge's assistance with the initial stages of the conventional solid state reactions. Hazar Salama acknowledges UNSW and UNSW@ADFA for her Endeavour International Postgraduate Research Scholarship (EIPRS) and University International Postgraduate Award (UIPA).

References

[1] Y. Wang, X. Lu, Y. Chen, F. Chi, S. Feng and X. Liu, *J. Solid State Chem.* **178** 1317 (2005).

[2] Y.H. Huang, H. Fjellvåg, M. Karppinen, B.C. Hauback, H. Yamauchi and J.B. Goodenough, *Chem. Mater.* **18**, 2130 (2006).

[3] J.-S. Zhou, J.B. Goodenough, J.M. Gallardo-Amores, E. Morán, M.A. Alario-Franco and R. Caudillo, *Phys. Rev. B* **74** 014422 (2006).

Vibration Characterisation of a Joule-Thomson Cryocooler for a SQUID-based Metal Detection System

Marcio A. Santin[a,b] and Gerard J.J.B. de Groot[a]

[a] *CSIRO Industrial Physics, Lindfield 2070, NSW, Australia.*
[b] *Federal University of Santa Catarina, Brazil.*

A commercial Joule-Thompson cryocooler – the Cryotiger® - is used to cool a SQUID-based metal detector. Compared to our previous liquid nitrogen cooled system the performance of the detector is reduced due to spurious magnetic signals introduced by mechanical vibration. In order to design vibration reducing measures, the vibration characteristics of several parts of the cryocooler cold head were determined. The characterisation was experimentally performed with a laser vibrometer and modelled with analytical and finite element methods. We observed good agreement between the measured and modelled natural resonant frequencies.

1. Introduction

Very sensitive high-temperature SQUID (Superconducting QUantum Interference Device) magnetometers are used for the detection of small metal contaminants in food and other products. When the SQUIDs are cooled with liquid nitrogen, good detection performance is obtained. However, when a commercial Joule-Thomson cryocooler – the Cryotiger® - was used, the performance was reduced due to spurious magnetic signals introduced by mechanical vibration, as can be seen in Figure 1[1]. Similar sensitivity issues were reported by Rijpma et al., [1].

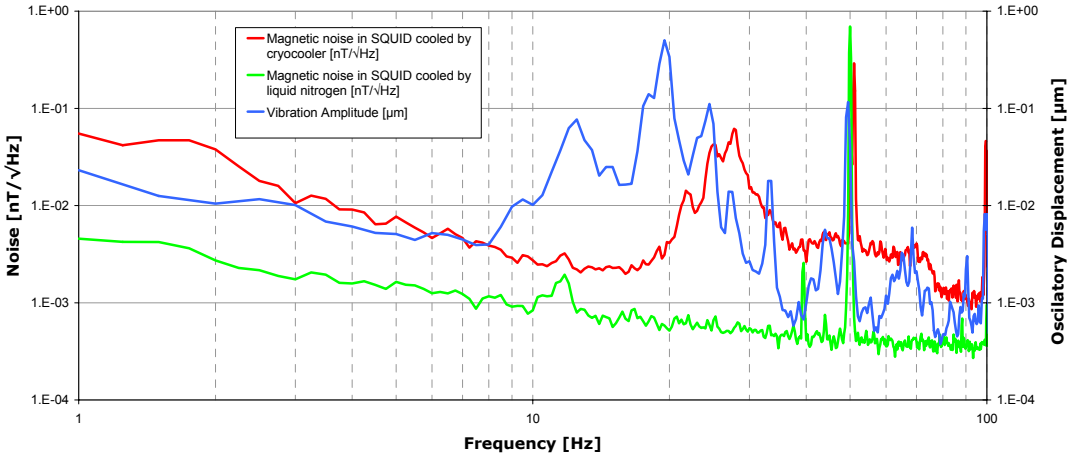

Figure 1. Comparison between vibration measured on the top of the titanium enclosure (blue trace), the noise of the SQUID magnetometer mounted on the cryocooled system (red trace) and mounted on the LN_2 cooled system (green trace).

It is assumed that that noise can be generated in two ways: the translation or rotation of the SQUIDs in a magnetic field and the movement of magnetised components of the cold head

[1] The vibration measurement corresponds to one translational orientation of the selected point on the component. The amplitude supplied by the vibrometer should be taken as approximate due to operation at, or below, the manufacturer's minimum specified amplitude range.

inside the shielding, [1]. Preliminary calculations indicate that the latter is the most likely source of noise. This aspect is still being investigated.

These movements may come from four sources of vibration: compressor; refrigerant movement in the cold head; excitations from the floor; and direct excitations to the cold head, i.e. shocks.

In order to design and implement measures to reduce the effect of vibrations, we aim to provide an improved understanding of the dynamic characteristics of the system components.

2. System description

The cold head is shown in Figure 2 and the experimental system components are shown in the Figure 3.

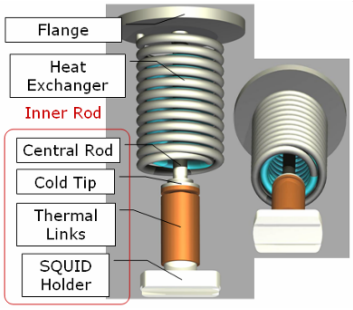

Figure 2. Simplified[2] model of the cold head. The inner part of the Heat Exchanger, also a helical tube, is shown in blue.

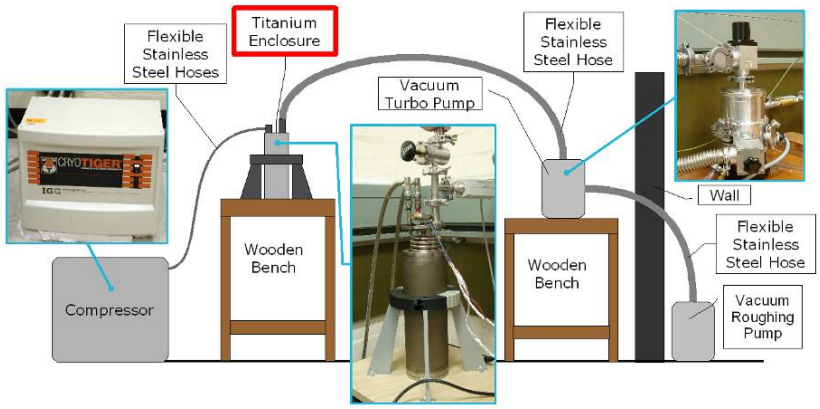

Figure 3. Previous experimental setup.

3. Vibration Characterization

The vibration characterisation was conducted by measurement and analysis of the response to excitation and by simulations of natural frequencies and resonant modes of the cold head.

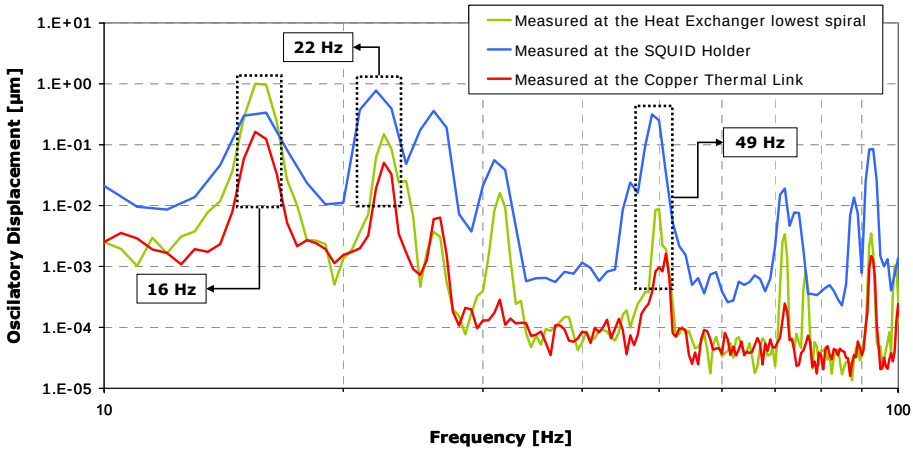

Figure 4. Impulse response of the cold head.

The vibration measurements were performed using a Polytec Laser Doppler Vibrometer. To determine the natural frequencies, the cold head was suspended by strings and excited with a rubber hammer. The impulse response is shown in Figure 4[3].

[2] In the modelling, it was decided not to include the boiler, throttle valve and the internal helical tube of the heat exchanger (which is inside the visible part and is part of the counter-flow assembly).

[3] See footnote 1.

The vibration frequency spectrum during system operation is shown in Figure 1 and the finite element (FE) and analytical models were used to determine which cold head components correspond to the measured resonant frequencies.

The main modes and frequencies found in the simulations are shown in Figure 5 and are in good agreement with the measured values, see Table 1.

Compo-nent / Method	Heat Exchanger – Outer Coil	Heat Exchanger – Inner Coil	Inner Rod
FEA	16.5 Hz(1)	21.4 Hz(2)	49 Hz(3)
Measurement	16 Hz(1)	22 Hz(2)	49 Hz(3)
1–See Figure 5(b); **2**–See Figure 2; **3** –See Figure 5(a).			

Table 1 - Natural frequencies obtained from FE analysis and measurements.

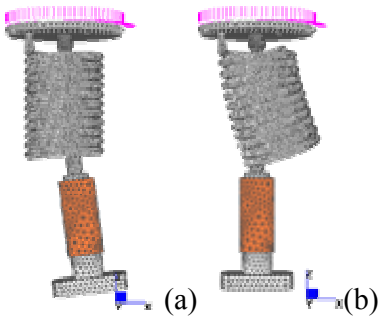

Figure 5. FE Simulations – (a) Inner rod resonance frequency, ≈ 50Hz. (b) Outer part of the Heat Exchanger resonance, ≈ 16,5Hz.

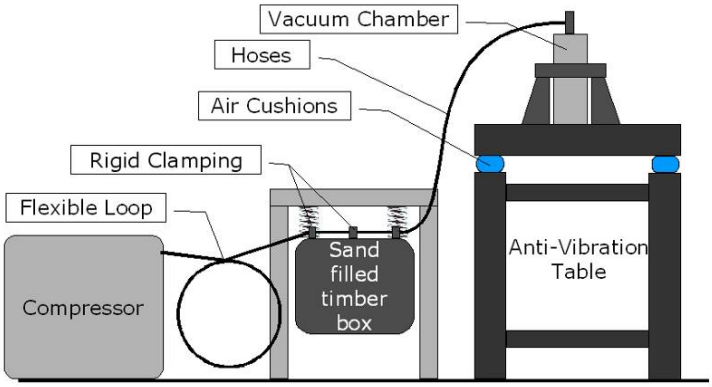

Figure 6. Diagram representing one of the proposed solutions.

4. Conclusions

We have measured and modelled resonance frequencies in the cold head which are in the same 'spurious' noise frequency range – 10 to 30 Hz - as measured with the SQUID when the cryocooler is operational. The measured and modelled 50 Hz resonance frequency of the cold head inner rod was also visible in the SQUID signal. This knowledge may be used to reduce signal deterioration due to the vibration. To reduce the effect of vibration, the external excitation should be reduced, the resonance frequencies should be altered and/or damping inside the cold head should be considered. A range of anti-vibration measures are proposed and are being implemented.

- Clamp the compressor hoses rigidly to a vibration absorber. For isolation from the ground a spring suspended timber box (filled with sand) was used, see Figure 6.
- Add damping elements, such as rubber disks, between the coils of the heat exchanger.
- Isolate the system from external (i.e. floor) excitations (anti-vibration table).
- Change the resonance frequency of the cold head components - aiming at higher frequencies - and hence avoiding resonance during excitation.

References

[1] A.P. Rijpma, H.J.M. ter Brake, E. de Vries, H.J. Holland and H. Rogalla. *Cryogenics* ***45,*** 317 (2005).

Niobium Step Josephson Junctions

N. Savvides and S. A. G. Vrouwe

CSIRO Industrial Physics, Lindfield, NSW 2070, Australia.

The characteristics of superconducting Josephson junctions are strongly dependent on geometric factors. Novel junctions were fabricated using Nb thin film microbridges (thickness d = 25–200 nm) onto substrate steps of height h = 25–200 nm. We report current-voltage (I-V) and Josephson critical current I_c measurements over a temperature range T = 1.5–K. By varying the ratio d/h it was possible to alter the junctions from non-hysteretic to ones with strong hysteretic I-V behaviour. A step-like structure in the temperature dependence of I_c indicates complex vortex dynamics.

1. Introduction

The current-voltage (I-V) characteristics of a Josephson junction are characterized by a Josephson current for $V = 0$, a current plateau at the Josephson critical current I_c where the voltage suddenly increases to the gap voltage, and a linear region where the material is in a normal state [1]. At I_c thermally activated Josephson vortices enter the junction from both ends and flow to the centre at a fixed velocity thus giving rise to the observed rise in voltage.

The characteristics of Josephson junctions and their use in various devices are strongly affected by geometric factors. The Josephson penetration length, λ_J, gives a measure of the distance in which d.c. Josephson currents are confined to the edges of the junction, and can be used to classify junctions into "small" ($L < \lambda_J$) and "large" ($L > \lambda_J$) where L is the length of the junction [2]. Here, we report the characteristics of Nb thin-film junctions where the superconducting weak link is caused by a step milled onto the substrate.

2. Specimens and measurements

The thin film junctions consisted of niobium microbridges (width W = 1.5–20 μm, length L = 600 μm, thickness d = 25–200 μm) deposited by magnetron sputtering over a vertical step of height h = 25–250 nm which was previously ion-beam milled in the SiO_2 layer (1–2 μm) of thermally oxidized silicon wafers. Figure 1 shows two of the possible junctions geometries, and Fig. 2 shows the corresponding SEM images of the fabricated devices. It is important to note that magnetron sputtering does not produce conformal coverage on the step and hence $W \leq 0.1d$; also, $L >> W$, and thus all junctions belong to the "large" junction configuration [2]. For junctions with $d/h \leq 1$ the very thin film on the step forms a transverse "overlap" weak-link junction. As d/h becomes greater than unity the overlap becomes *in-line*; here, the junction barrier is due to a very thin defect layer which originates from the step. This in-line defect layer results in increased junction capacitance and is expected to lead to significant hysteretic behavior in the I-V which can be tuned by means of the ratio d/h.

The transport measurements were performed in a double-dewar glass helium system which was magnetically screened by two concentric μ-metal shields to allow zero-field cooling. The specimens were immersed in liquid helium and temperatures to 1.5 K were achieved by pumping on the liquid. Measurements above 4.2 K were done in cold helium gas. The temperature was monitored using a calibrated carbon-glass resistance thermometer (Lakeshore CGR-1-500-1.4L), and during measurements it was held fixed to ± 0.01 K.

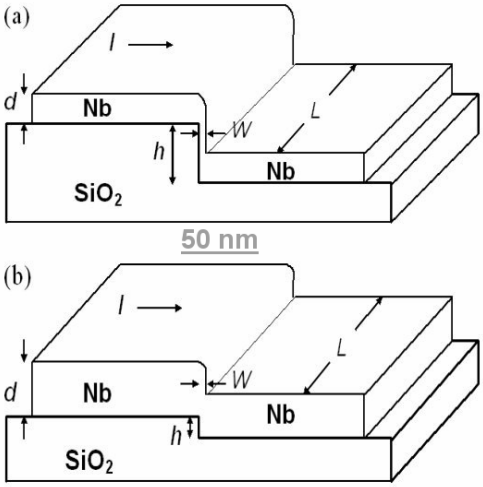

Fig. 1. Schematic of Nb junction formed over a step milled on the substrate: (a) $d/h < 1$ and (b) $d/h > 1$.

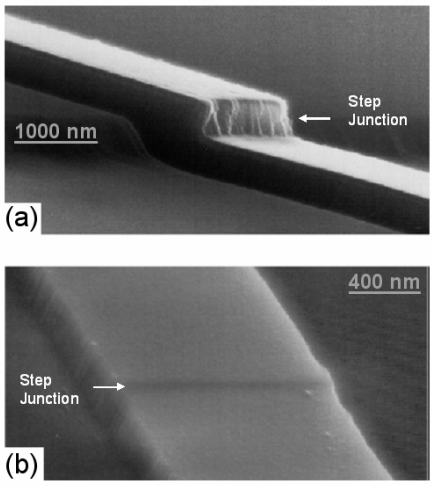

Fig. 2. SEM images of niobium step junctions corresponding to the schematic layout of Fig. 1.

3. Results

Typical *I-V* characteristics representing four different types of step junctions are shown in Fig. 3. All the measured junctions showed symmetric *I-V* curves with the normal resistance extrapolating to the origin. The film thickness to step-height ratio, *d/h*, varied from 0.24 to 5.3 for junctions A to D. For *d/h* less than or near unity the junctions showed standard *I-V* characteristics with a small degree of hysteresis (A, C).

For $d/h >> 1$ the in-line overlap forming the junction leads to significant hysteresis (e.g., junction D). Figure 4 shows results for a group of junctions on the same chip (d = 125 nm, h = 25 nm, L= 20–1.5 μm). These junctions have reproducible hysteretic behaviour, similar to that of planar or layered superconductor-insulator-superconductor (SIS) junctions.

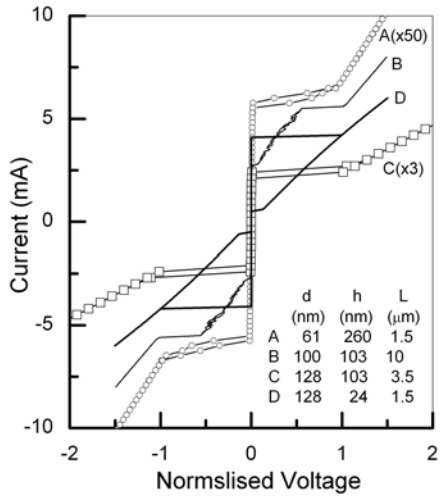

Fig. 3. *I-V* characteristics at 4.2 K of junctions with different ratio of film thickness to step height, *d/h*.

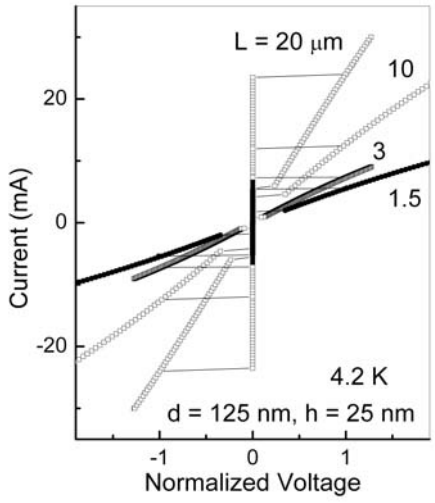

Fig. 4. Junctions with d/h = 5 showing highly hysteretic *I-V* characteristics.

To establish the temperature dependence of the Josephson critical current, $I_c(T)$, selected specimens were zero-field cooled to 1.5 K, then the *I-V* characteristics were recorded as a

function of increasing temperature (1 K per hour). Figure 5 shows typical results for a junction with $d/h < 1$ and $L = 1.5$ μm. It is seen that I_c decreases in a series of irregular steps whereas one would expect a smooth decrease in accordance with the Ambegaoker and Baratoff model [3]. This behavior suggests that Josephson vortices are pinned at the edges of the junction and significant thermal activation is required to cause them to flow to the centre of the junction where they annihilate, thus producing an observable voltage. A similar behavior was observed in $YBa_2Cu_3O_7$ bi-crystal grain-boundary junctions [4] where individual Josephson vortices were activated by injecting low-power microwave signals (4.4 and 8.7 GHz) into the junction. (Note that this behavior of Josephson vortices is quite different to the avalanche-type or collective flow of Abrikosov vortices observed in Nb films [5].) Some junctions, formed on high substrate steps ($d/h < 0.5$), showed anomalous *I-V* behaviour such as two or more voltage steps in the *I-V* characteristics (Fig. 6). This behaviour is indicative of multiple weak link acting in parallel but with a common resistive shunt.

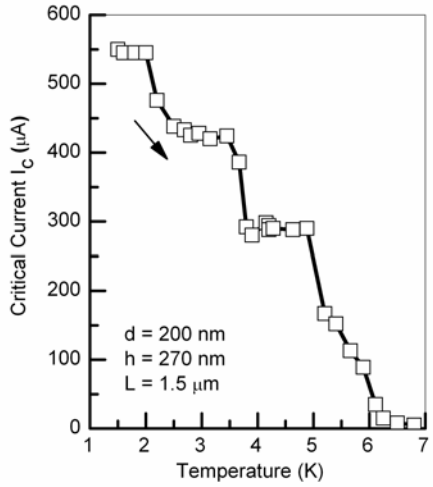

Fig. 5. Temperature dependence of the Josephson I_c..

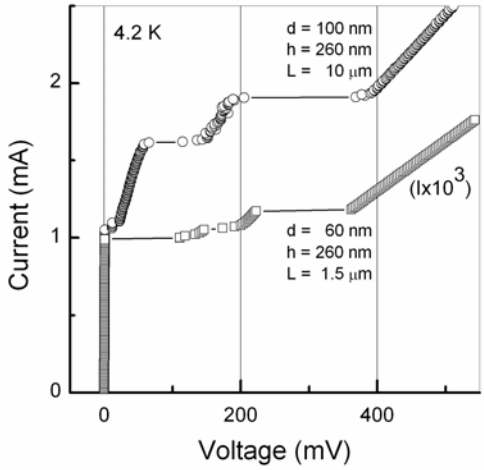

Fig. 6. Voltage steps in *I–V* of a junctions with $d/h < 1$

4. Conclusion

Josephson junctions, belonging to the "large" junction classification, were fabricated by patterning Nb films that were deposited over a step on SiO_2/Si substrates. By controlling the ratio of film thickness to step height, *d/h*, from about 0.25 to 5.3 it was demonstrated that the *I-V* characteristics could be varied from non-hysteretic to highly hysteretic. Other interesting observations include strong pinning of Josephson vortices at the edges of the junction, and voltage steps in the *I-V* characteristics due to multiple weak links acting in parallel.

References

[1] B. D. Josephson, *Rev. Mod. Phys.* **36**, 216 (1964).
[2] A. Barone and G. Paterno, *Physics and applications of the Josephson effect (*John Wiley & Sons, New York, 1982).
[3] V. Ambegaokar and A. Baratoff, *Phys. Rev. Lett.*, **10** 486 (1963).
[4] H. Xin, D.E. Oates, S. Sridhar, G. Dresselhaus and M.S. Dresselhaus, *Phys. Rev. B* **61**, R14952 (2000).
[5] M.S. Welling, R.J. Westerwaal, W. Lohstroh and R.J. Wijngaarden, *Physica C* **411**, 11 (2004).

Neutron Diffraction Results for Three-layer Aurivillius Phases Containing Magnetic Transition Metal Cations: Ru (IV), Ir (IV) and Mn (IV)

Neeraj Sharmaa, Brendan J. Kennedy[a], Margaret M. Elcombe[b], Maxim Avdeev[b] and Chris D. Ling[a,c]

[a]*School of Chemistry, University of Sydney, NSW 2006, Australia.*
[b]*Bragg Institute, ANSTO, NSW 2234, Australia.*

The synthesis and characterisation of three-layer Aurivillius-type phases containing magnetic cations M^{4+} (M = Ru, Ir, Mn), based on the substitution M^{4+} for Ti^{4+} in $Bi_2Sr_2(Nb,Ta)_2TiO_{12}$ has recently been reported [1]. These structures show the partial substitution of Sr^{2+} for Bi^{3+} in the $[Bi_2O_2]^{2+}$ layers that results in the decrease of M^{4+} content; the compositions prepared were $Bi_{2-x}Sr_{2+x}(Nb,Ta)_{2+x}M_{1-x}O_{12}$, $x \approx 0.5$. This work looks at the neutron diffraction of these samples and shows the existence of a symmetry-lowering mode.

1. Introduction

Aurivillius phases $[Bi_2O_2]\cdot[A_{n-1}B_nO_{3n+1}]$ are layered oxides composed of α-PbO-type layers $[Bi_2O_2]^{2+}$ alternating with n perovskite-type layers [2, 3]. Interest in Aurivillius phases has focused on their catalytic properties and oxygen ion conductivity, as well as their strong ferroelectricity [4, 5] which arises due to the rotation of BO_6 octahedra, lowering the symmetry from tetragonal to monoclinic, and allowing the perovskite *A*- and *B*-site cations to be displaced relative to the oxygen anion array.

Substituting magnetic transition metal cations into the central octahedral layer of the perovskite-type block, while maintaining ferroelectric displacements in the outer octahedral layers, presents a possible route to multiferroic (magnetoelectric) materials. The crystallographically ordered layering of magnetic and non-magnetic transition metal MO_6 octahedra is shown to be the case in $Bi_{2-x}Sr_{2+x}(Nb,Ta)_{2+x}(Ru/Ir/Mn)_{1-x}O_{12}$, $x \approx 0.5$ [1]. The ordering is likely to be due to the contrast between the coordination environments of the *B*-site cations in the central and outer octahedral layers of the perovskite-type block. However, considerable *B*-site disorder is still observed in some cases, *e.g.* between Nb and Ti in $Bi_2Sr_2Nb_2TiO_{12}$ [6]. Previous reports of magnetic $n = 3$ Aurivillius phases are contradictory. Yu *et al*.[7] reported the synthesis of $Bi_2Sr_2Nb_2MnO_{12}$, *i.e.*, the complete substitution of Mn^{4+} for Ti^{4+} in $Bi_2Sr_2Nb_2TiO_{12}$, presenting (but not refining) X-ray powder diffraction (XRD) data. McCabe and Greaves [8] could not reproduce this phase in the manner reported, observing an impurity phase in neutron powder diffraction (NPD) data, and proposing a single-phase sample of composition $Bi_2La_{0.6}Sr_{1.4}Nb_2MnO_{12}$.. Recently we reported the synthesis and structural properties of a series of phases $Bi_{2-x}Sr_{2+x}(Nb,Ta)_{2+x}(Ru,Ir,Mn)_{1-x}O_{12}$. In order to determine the *B* site ordering variable wavelength synchrotron X-ray diffraction data was used. Here we report the existence of a symmetry-lowering mode in the same system as observed by neutron diffraction data.

2. Experimental

Polycrystalline samples of $Bi_{2-x}Sr_{2+x}B_{2+x}M_{1-x}O_{12}$, where B = Nb, Ta and M = Ru, Ir, Mn were prepared over a range of x by conventional solid state synthesis using stoichiometric quantities of Bi_2O_3 (Aithaca, 99.999%), RuO_2 (Aithaca, 99.99%), IrO_2 (Aithaca, 99.99%), $SrCO_3$ (Aithaca, 99.995%), Mn_2O_3 (Aldrich, 99.999%), Nb_2O_5 (Aldrich, 99.99%), and Ta_2O_5 (Aldrich, 99.99%). Reagents were mixed, ground and pre-heated for 1 hour at 850°C. For

each composition, approximately half of the sample volume was then pressed into a pellet and heated in cycles of 950°C for 100 hours, 1000°C for 50 hours, and 1050°C for 50 hours, with intermediate regrinding, until a single phase was produced. The remaining half of the sample used as a 'sacrificial' powder to bury the pellets, in order to minimize the loss of Bi_2O_3 through volatilization.

Neutron powder diffraction data (NPD) were collected at 5K and 293K on the High Resolution Powder Diffractometer at the High-Flux Australian Reactor (HIFAR) facility, Australian Nuclear Science and Technology Organisation (ANSTO). Rietveld-refinements were carried out using the GSAS [9] suite of programs with EXPGUI [10] front-end.

3. Results and Discussion

Low temperature NPD data shows no signs of new peaks from magnetic origin in all the samples (Fig.1). However, the refinement of anisotropic displacement parameters shows displacements of the oxygens on the central layer of the perovskite block (O1, Fig. 2). The central layer of the three-layer Aurivillius phase contains the majority (>99%) of the magnetic cations [1]. In the $Bi_{2-x}Sr_{2+x}Nb_{2+x}Ru_{1-x}O_{12}$, $x = 0.5$ sample this cationic site would have mixed charge ($4^+/5^+$) as only 50% of the site is occupied by Ru^{4+} and the reminder by Nb^{5+}. The nearby O1 site may be expected to show signs of this charge difference. However, a larger effect is visible on these O1 sites. The O1 sites have the largest displacement perpendicular to the direction of the central cation. The largest displacement is in the *ab* plane, suggesting a rotation of the octahedra around the mixed cationic site. If these displacements corresponding to the O1 site were due to thermal motions then they would increase with temperature. However, the displacements increase with decreasing temperature. Thus the displacements are probably related to a symmetry-lowering mode. Symmetry-lowering modes have recently been investigated in three-layer Aurivillius phases by Zhou et al [11].

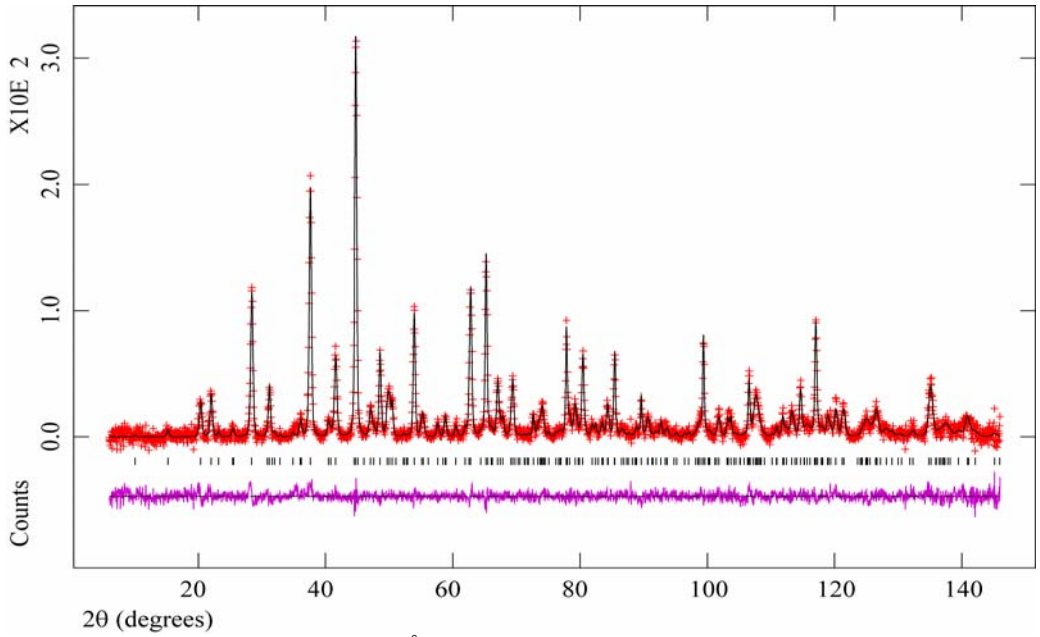

Fig. 1. Final fit to Rietveld-refined λ = 1.49 Å NPD data for $Bi_{2-x}Sr_{2+x}Nb_{2+x}Ru_{1-x}O_{12}$, $x = 0.5$. Observed data are shown as crosses (+), calculated data as a solid line, and the differences as a solid line below. Goodness-of-fit = 4.301 for 54 refined parameters. Overall powder *R*-factors: $R_p = 0.0850$ $wR_p = 0.0574$.

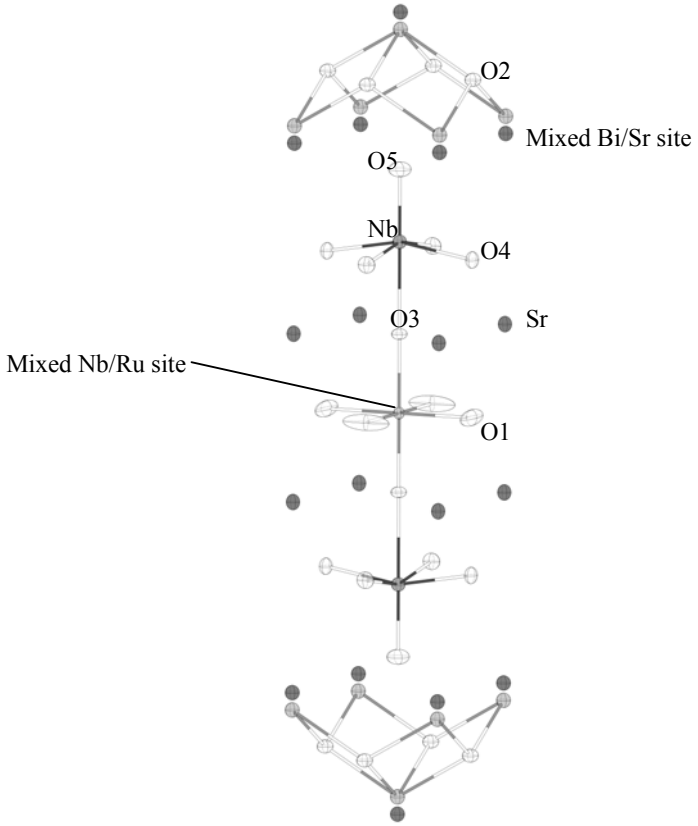

Fig. 2. ORTEP diagram of the structure of $_{-x}Sr_{2+x}Nb_{2+x}Ru_{1-x}O_{12}$, $x = 0.5$ obtained from Rietveld refinement against low temperature NPD.

The symmetry-lowering mode and substitution of the central perovskite layer with ~50% magnetic cations highlights the potential for multiferroic behaviour in these systems.

Acknowledgments

The NPD work was supported by Australian Institute of Nuclear Science and Engineering (AINSE) and the PGRA scheme.

References

[1] N. Sharma, P.Y. Chen, G.E. Wrighter, B.J. Kennedy, P.L. Lee and C.D. Ling, *J. Solid Chem.* **180**, 370 (2007)
[2] B. Aurivillius, *Ark. Kemi.* **1**, 463 (1949).
[3] B. Aurivillius, *Ark. Kemi.* **2**, 519 (1950).
[4] E.C. Subbarao, *J. Phys. Chem. Solids.* **23**, 665 (1962).
[5] G.A. Smolenski, V.A. Isupov and A.I. Agranovskaya, *Sov. Phys. Solid State (Engl. Transl.).* **3**, 651 (1953).
[6] C.H. Hervoches and P. Lightfoot, *J. Solid State Chem.* **153**, 66 (2000).
[7] W.J. Yu, Y.I. Kim, D.H. Ha, J.H. Lee, Y.K. Park, S. Seong, and N.H. Hur, *Solid State Comm.* **111**, 705 (1999).
[8] E.E. McCabe and C. Greaves, *J. Mater. Chem.* **15**, 177 (2005).
[9] A.C. Larson and R.B. Von Dreele, Los Alamos National Laboratory Report LAUR 86-748, 1994.
[10] B.H. Toby, *J. Appl. Cryst.* **34**, 210 (2001).
[11] Q. Zhou, B.J. Kennedy, and M.M. Elcombe, *J. Solid State Chem.* **179**, 3744 (2006).

Scattering Potentials in Condensed Matter for Low Energy Electrons

A.E. Smith

School of Physics and Materials Engineering, Monash University, Victoria 3800, Australia.

Necessary Kramers Kronig conditions link the electron energy loss function with its virtual part and consequentially the imaginary part of the scattering potential with its real part. Results are explored for analytic fits of the loss function employing Drude (i.e. Lorentzian) and "derived" Drude forms. Quadrature evaluates the imaginary and real parts of the scattering potential.

1. Introduction

The scattering potential felt by low energy electrons is dependent on the incident energy. For Low Energy Electron Diffraction (LEED), the energy dependence of the real part, commonly called the inner potential and seen in the position of diffraction peaks, changes by several eV for incident energies in the range up to 120 eV. The corresponding imaginary component of the scattering potential, manifested in the width of spectral features, varies by a similar amount in the same incident energy range [1]. Similar energy dependencies need to be incorporated in the full analysis of results from other methods such as, for instance, photo-electron spectroscopy [2].

Previously we have shown how first principle quantum calculations can be used to determine the incident energy dependence of the scattering potential due to electron – electron interactions [3,4]. However, in order to carry out efficient calculations analytic fits were introduced. The present work explores the nature of these fits and shows how necessary Kramers-Krönig (KK) conditions link the real and imaginary parts of the scattering potential. In particular useful approximations are supported by Drude (i.e. Lorentzian) together with "derived" Drude expressions for the real and imaginary part of the dielectric function extended to finite momentum transfers [5,6].

2. Kramers Kronig relations and scattering potential results

Within classical electromagnetic theory, non-locality in time with causal connection between polarization and the electric field is treated through the introduction of a frequency dependent dielectric constant which results in the Kramers Kronig relations:

$$\mathrm{Re}\,\varepsilon(\omega)/\varepsilon_0 = 1 + \frac{1}{\pi} P \int_{-\infty}^{\infty} \frac{\mathrm{Im}\,\varepsilon(\omega)/\varepsilon_0}{\omega' - \omega} d\omega' \qquad \mathrm{Im}\,\varepsilon(\omega)/\varepsilon_0 = -\frac{1}{\pi} P \int_{-\infty}^{\infty} \frac{[\mathrm{Re}\,\varepsilon(\omega)/\varepsilon_0 - 1]}{\omega' - \omega} d\omega'$$

Non-locality in space can be treated through the generalisation of dispersion by the introduction of a dielectric constant dependent not only on frequency but also on wave vector[7]. Linear response theory produces similar expressions for the reciprocals [8]:

$$\mathrm{Re}\,\frac{1}{\varepsilon(k,\omega)} - 1 = \frac{1}{\pi} P \int_{-\infty}^{\infty} \frac{\mathrm{Im}[1/\varepsilon(k,\omega')]}{\omega' - \omega} d\omega' \qquad \mathrm{Im}\,\frac{1}{\varepsilon(k,\omega)} = -\frac{1}{\pi} P \int_{-\infty}^{\infty} \frac{\{\mathrm{Re}[1/\varepsilon(k,\omega')] - 1\}}{\omega' - \omega} d\omega'$$

Within quantum mechanics perturbation theory allows the inelastic mean inner potential and the corresponding (KK related) virtual real inner potential to be found in terms of the reciprocal dielectric function (loss function), e.g. within the isotropic approximation [3]:

$$U^i = \frac{e^2}{\pi V}\int_0^{E^0/\hbar} d\omega \int_{|q(\omega_{\min})|}^{|q(\omega)|} \frac{d|q|}{|q|}\,\mathrm{Im}\{\varepsilon_{0,0}^{-1}(|q|,\omega)\}\,; U^r = \frac{e^2}{\pi V}\int_0^{E^0/\hbar} d\omega \int_{|q(\omega_{\min})|}^{|q(\omega)|} \frac{d|q|}{|q|}\,\mathrm{Re}\{\varepsilon_{0,0}^{-1}(|q|,\omega)+1\}$$

Whilst the loss function for the zero q (optical) case has been both measured and calculated for many materials, its q dependency is less well known [5]. Fig. 1 shows the result of fitting loss functions determined from first principle quantum calculations for the particular case of silicon with momentum transfer along the 100 direction [9]. Rather than employing just a single Lorentzian as in previous considerations (Fig. 2 [9]), the loss functions was fitted by a three term sum of Lorentzian functions (plasmon-pole or Drude functions) with quadratic q dependency (satisfying the necessary KK sum rules)[5]:

$$\mathrm{Im}\{\frac{-1}{\varepsilon_{0,0}(q,\omega)}\} = \sum_{j=1}^{n} A_j D_j[\Omega_j(q),\Gamma_j(q),\omega] \qquad \text{with}$$

$$D_j[\Omega_j(q),\Gamma_j(q),\omega] = \frac{\Gamma_j(q)\omega}{(\Omega_j^2-\omega^2)^2+\Gamma_j^2(q)\omega^2}$$

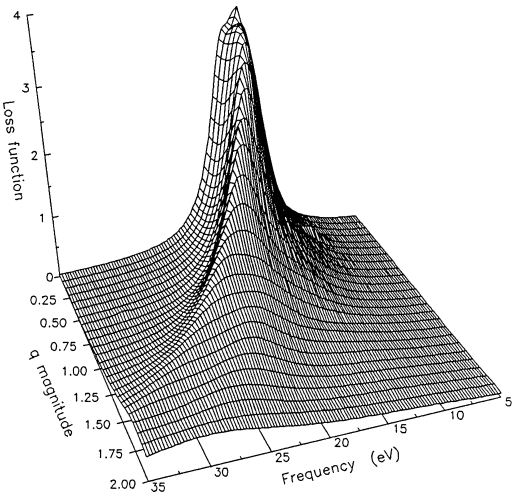

Fig. 1: Loss function $\mathrm{Im}\{\frac{-1}{\varepsilon_{0,0}(q,\omega)}\}$ as function of wave vector and frequency modelling loss with momentum transfer along [100] in silicon.

Analytically it necessarily follows that for each of these Lorentzians there is a corresponding real term. Consequentially the sum corresponding to the KK related virtual loss function, as shown in Fig. 2, must be of the form: $\mathrm{Re}\{\varepsilon_{0,0}^{-1}(q,\omega)-1\} = \sum_{j=1}^{n} A_j E_j[\Omega_j(q),\Gamma_j(q),\omega]$ with the same weight A_j and where each of the virtual Drude loss functions are:

$$E_j[\Omega_j(q),\Gamma_j(q),\omega] = \frac{\Omega_j^2-\omega^2}{(\Omega_j^2-\omega^2)^2+\Gamma_j^2(q)\omega^2}$$

In general other related model functions might be used, for example, the so-called "derived Drude" function which exhibits a more intense peak around the resonance energy [6]. For this, the KK related pair is each again a sum, but this time over functions of the form:

$$F_j[\omega_j(q),\Gamma_j(q),\omega] = \frac{2[\omega_j(q)\omega]^3}{(\omega_j^2-\omega^2)^2+\Gamma_j^2(q)\omega^2}$$

$$G_j[\omega_j(q),\Gamma_j(q),\omega] = \frac{(\omega_j(q)^2-\omega^2)[(\omega_j(q)^2-\omega^2)^2+3(\Gamma_j(q)\omega)^2]}{[(\omega_j^2-\omega^2)^2+\Gamma_j^2(q)\omega^2]^2}$$

Results for scattering potentials can then be found by numerically integrating these analytic loss functions over wave number and frequency. For silicon integration of the loss functions shown in Figs. 1 and 2 results in both real and imaginary potentials indistinguishable from the results for previously found using the full dielectric matrix method for the incident energy range 10 to 10,000 eV (see Fig. 2 (a) and (b), reference [10] and also in particular Fig. 2 reference [11]). They in turn are consistent with empirical so-called 'universal curve' values. Of particular interest, they predict observed energy variations of the virtual real inner potential (see for instance, reference [1]). In this way it can be understood that the onset of the 'plasmon threshold' corresponding to the peak of the loss function not only results in an increase in spectral line width but also necessarily a spectral position shift.

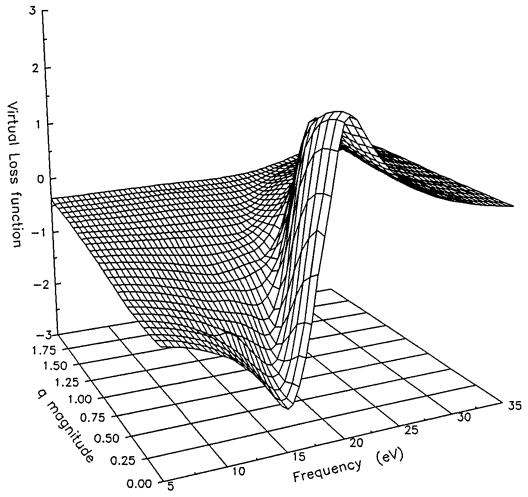

Fig. 2: Virtual loss function $\mathrm{Re}\{\varepsilon^{-1}_{0,0}(q,\omega)-1\}$ as function of wave vector and frequency modelling loss with momentum transfer along [100] in silicon.

References

[1] L.J. Clarke, S*urface Crystallography, An Introduction to Low Energy Electron Diffraction* (Wiley 1985) p 144.

[2] S. Hüfner, *Photoelectron spectroscopy: principles and applications, 2nd ed.* (Springer, 1996).

[3] A.J. Forsyth, A.E. Smith and T.W. Josefsson, *Phys. Rev.* **B56,** 6400 (1997).

[4] A.J. Forsyth, A.E. Smith and T.W. Josefsson, *Acta Cryst.* **A53,** 523 (1997).

[5] R.H. Ritchie and A. Howie, *Philos. Mag.* **36,** 463 (1977).

[6] D. Emfietzoglou and H. Nikjoo, *Radiat. Res.* **163,** 98 (2005).

[7] P.M. Platzman and P.A. Wolff, *Waves and Interactions in Solid State Plasmas*, (Academic Press, New York 1972).

[8] D. Pines, *Elementary Excitations in Solids*, (Benjamin, New York 1964).

[9] T.W. Josefsson and A.E. Smith, *Phys. Lett.* **A180,** 174 (1993).

[10] T.W. Josefsson and A.E. Smith, *Phys. Rev.* **B50,** 67322 (1994).

[11] A.E. Smith, in *Condensed Matter Theories, Vol. 17,* ed. M.P. Das and F. Green, (Nova Science, New York 2003), p 353.

A Novel Probehead for an Electron Spin Echo Study of an Australian Coal

N. Suwuntanasarn[a], W.D. Hutchison[a], G. Milford[b] and R. Bramley[c]

[a] *Centre for Quantum Computer Technology, School of Physical, Environmental and Mathematical Sciences, UNSW@ADFA, Canberra ACT 2600.*
[b] *Centre for Quantum Computer Technology, School of Information Technology and Electrical Engineering, UNSW@ADFA, Canberra ACT 2600.*
[c] *Research School of Chemistry, The Australian National University, Canberra ACT 0200.*

An X-band pulsed electron spin echo (ESE) probe head, which can be fitted with a CW-ESR cryostat, has been designed and tested. The three dimensional electromagnetic field aspects of the structure have been fully assessed and optimised. The theoretical simulations and experimental results agree well. The pulsed ESE system is used to perform detailed ESE studies of a "Queensland coal" sample.

1. Introduction

Pulsed electron spin echo (ESE) is a very powerful tool for studying relaxation phenomena. Here an X-band ESE probe head has been designed specially for a study of phosphorus doped silicon (Si:P) with quantum computing applications in mind [1]. The probe head is designed to fit a conventional CW-ESR cryostat and allow quick sample access at low temperature (to 4 K). The probe head resonator design is based on a loop gap resonator (LGR) structure [2, 3]. In the design, the three dimensional electromagnetic field was simulated numerically using a 3D electromagnetic simulator (CST Microwave Studio [4]). The whole probe head structure was also tested experimentally, and the results are in agreement with the simulations. ESE was then performed on a "Queensland coal" sample in order to test the probe design and our home built pulse spectrometer ahead of Si:P work. A coal sample is a convenient single line sample for testing an ESE system since pulsed ESE studies on various types of coals exist for comparison [5]. Interestingly there appears to be no reported ESE study of Australian coal.

2. Probe head design

A conventional ESR-900 Oxford instrument cryostat shield is replaced by the probe head. The probe head consists of a resonator, microwave and cryostat shield, tuning and matching structure. The shield was designed so that its cut-off frequency is a few gigahertz higher than the resonant frequency to prevent microwave radiation leakage. The structure also incorporates the top vacuum seal for the cryostat. The probe head is adjustable both up-down and in rotation to allow the tuning of the resonator. Microwave coupling into the resonator is via a rectangular iris and Gordon coupler [6], which is rigidly attached to the shield. Matching is achieved by adjusting a movable Teflon insert in the Gordon coupler. Optimisation of the entire probe head structure was carried out using the simulation tool to achieve a good impedance match at the resonant frequency (low S_{11} magnitude, $|S_{11}|$) and high conversion factor ($\Lambda = B_1/(PQ)^{0.5}$, where B_1 is the magnetic induction in the rotating frame at a given microwave frequency, P is the microwave incident power and Q is the quality factor of the resonator).

The resonator is a rectangular LGR shape which is particularly suitable for flat samples (wafers). Samples up to 5 mm width (x-axis), 1.7 mm thick (y-axis) and 5 mm height (z-axis) can be inserted into the resonator. The resonator structure and the simulated magnetic field are shown in Fig.1. A relatively large magnetic field with reasonable

homogeneity is produced over the sample area. Measurement was performed with a network analyser and close agreement was obtained between the resonant frequencies and coupling figures (simulated: 10.006 GHz and measured: 10.0568 GHz from the $|S_{11}|$ values) (see the fig.1 (c)). The Q (calculated from the relationship $Q=f/\Delta f$, where Δf is the width of the resonance curve at -3 dB level) of the real structure is approximately 230. The large magnetic field and low Q values produced by the probe head allow a good conversion factor to be obtained and make it particular suitable for a pulsed ESE experiment. With the flat coal sample, the resonator performance was also assessed against other types of the resonator such as folded-half wave and TE_{102} rectangular cavity, and it was found that this resonator gave the best results.

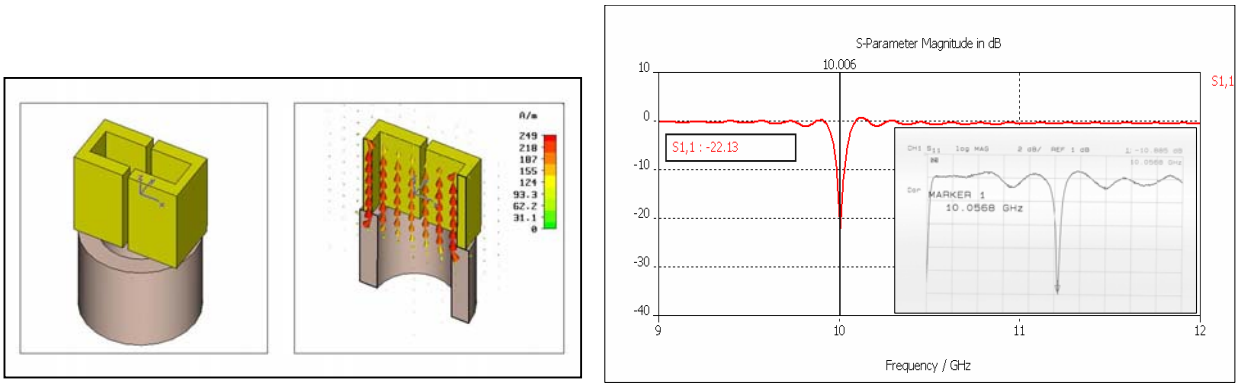

(a) (b) (c)

Fig. 1. The resonator simulated results (colour online): (a) the resonator structure; upper part (yellow) is copper while lower part (grey) is quartz, (b) the corresponding microwave magnetic field (arrows) at the sample position (MWS views) and (c) the simulated and measured (insert) $|S_{11}|$ values.

3. Electron spin echo results

An ESE experiment was performed on "South Blackwater" coal from Queensland with our homemade ESE spectrometer and the resonator described above. The coal sample consists of 85.8% C, 5.07% H, 6.3% ash. The g-factor of the sample, representing electrons bound to free radicals, was found from CW-ESR to be 2.0029, compared to the free electron g-factor (= 2.0023).

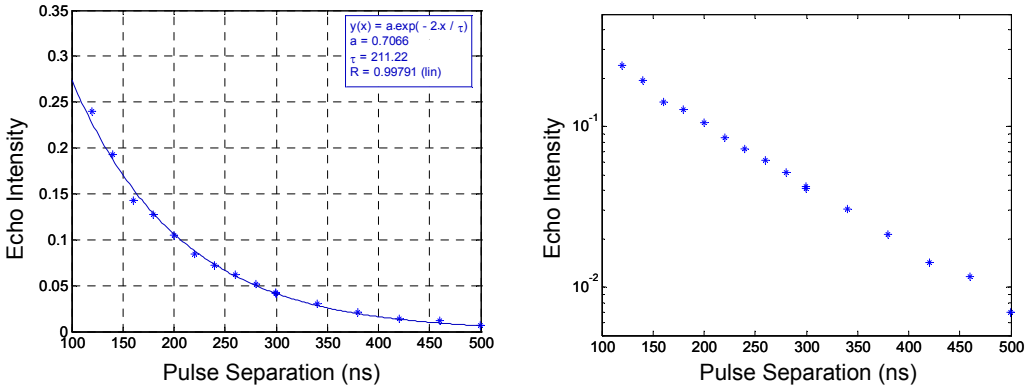

Fig. 2. The echo intensity at various pulse separations, τ, with (left) its corresponding semi-log plot.

A Hahn two-pulse ESE (π/2-τ-π-echo) was performed initially at varying pulse widths (π/2 and π) in order to find the optimum pulse width for the experiment. The optimum π/2 pulse was found to be 22 ns. The spin-spin relaxation time, T_2, of the sample is found from the plot of ESE intensity versus the variation of pulse separation time, τ. The plot of echo intensity versus the pulse separation, both linear and semi-log scale, is in Fig.2.

A fit of the echo decay data in Fig. 2 produced a T_2 for the coal sample of 211±12 ns. However, it is known that instantaneous diffusion can have an impact on the ESE measurement [7]. Further ESE experiments, where the second pulse width was varied, were performed to check for an effect from instantaneous diffusion. The plot of T_2 as a function of $sin^2(\theta/2)$, where θ is the spin turn angle of the second pulse is shown in Fig.3.

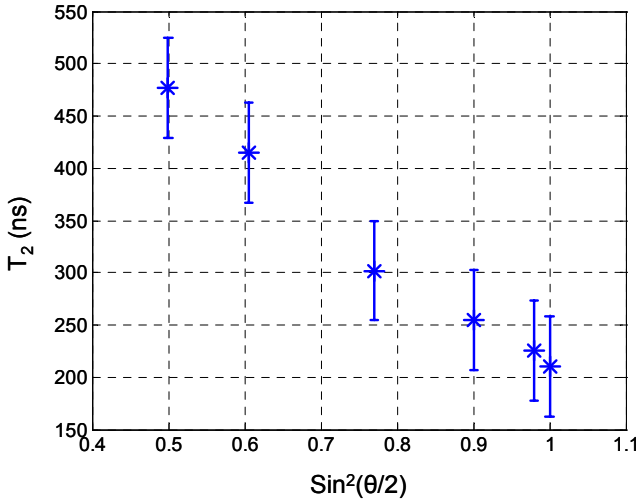

Fig. 3. The T_2 versus $\sin^2(\theta/2)$ of the coal sample.

The linear trend of the plot in Fig.3 indicates that instantaneous diffusion has a significant impact on the sample T_2 measurement. When extrapolated to $\theta = 0$ degrees the linear plot suggests an estimate of the T_2 value, in the instantaneous-diffusion free situation, of 800±80 ns. This T_2 result for the "South Blackwater" coal is within the range 356 ns to 1450 ns seen previously for various coal samples [1].

Acknowledgement

We gratefully acknowledge ARC funding support via the Centre for Quantum Computer Technology (CQCT) and staff of the PEMS mechanical and electronics workshops for their contributions to the construction of the probe head and the pulsed ESE spectrometer respectively.

References

[1] B.E. Kane, *Nature* **393**, 133 (1998).
[2] W. Froncisz and J.S. Hyde, *J. Magn. Reson.* **47**, 525 (1982).
[3] W. Piasecki, W. Froncisz and W.L. Hubbell, *J. Magn. Reson.* **134**, 36 (1998).
[4] CST Microwave Studio, http//:www.cst.com
[5] D.C. Doetschman and D.W. Dwyer, *Energy Fuels* **6**, 783 (1992).
[6] J.P. Gordon, *Rev. Sci. Instrum.* **32**, 658 (1961).
[7] A.M. Raitsimring, K.M. Salikhov, B.A. Umanskii and Y.D. Tsvetkov, *Soviet Physics Solid State*, **16**, 492 (1974).

Investigating the Photonic Behaviors of ZnO Nanocrystals

Y.Y. Tay[a, b], S. Li[b] and M.H. Liang[a]

[a] *School of Materials Science and Engineering, Nanyang Technological University, Singapore.*

[b] *School of Materials Science and Engineering, NSW 2033, Australia.*

The photonic behavior of size dependent ZnO is recently rigorously investigated. In this work, we examine ZnO nanocrystals of size less than 5 nm by correlating this photonic behavior to the material's crystal structure as well as the effect of relevant defects present in the material. There is a red shifting of their luminescence property that is different from quantum size effect which expects a blue shifting instead.

1. Introduction

Zinc Oxide (ZnO) is a wide band gap semiconductor and has an efficient near UV (~ 3.29eV, 370nm) emission, and commonly yield to have green (~510nm, 2.43eV) emission and sometimes yellow (~597nm, 2.08eV) or orange (~640nm 1.94eV) emission. However, the origins of these visible emissions remain controversial, particularly the green emission [1].

On the other hand, nanotechnology is an emerging interesting field. Particularly when particles size of pure ZnO reaches nanoscale e.g. smaller than 5nm in diameter, quantum size effect will occur causing blue shifting of the emission as a result of bandgap widening [2]. In this work, the crystal size of ZnO was physically reduced from 202 nm to 3.0 nm to investigate size effect on photoluminescence behavior of ZnO.

2. Experiment

ZnO (99.5% pure Analyticals Carlo Erba) powder was first annealed at 1200^{o}C in ambient condition with ramping rate of 5^{o}C/min and a dwelling time of 1hr. To reduce the crystal size physically in a control fashion, high energy ball milling was carried out with different duration.

The prepared ZnO materials were characterized using X-ray Diffractometer (XRD). Data were recorded using a Theta/Theta Bruker Diffractometer with a Cu Kα radiation with a divergence slit of 2^{o} and a 0.2mm width receiving slit. The crystal sizes of the as prepared ZnO powders were verified using JEOL 3010 HRTEM. Photoluminescence (PL) measurement was performed using Accent Rapid Photoluminescence Mapping System (RPM 2000) with a He-Cd laser source with an excitation wavelength of 325nm.

[a] corresponding author; email: s3197272@unsw.edu.au

3. Result and Discussions

The XRD line profile of the size reduced ZnO is shown in Figure 1. This characteristic peak which corresponds to the plane (012) of ZnO reveals substantial broadening with reduced crystal size. Complemented by the TEM images in Figure 1 (b), it is possible to reduce the crystal size of ZnO from 202 nm to 3.0 nm in the nanoscale region.

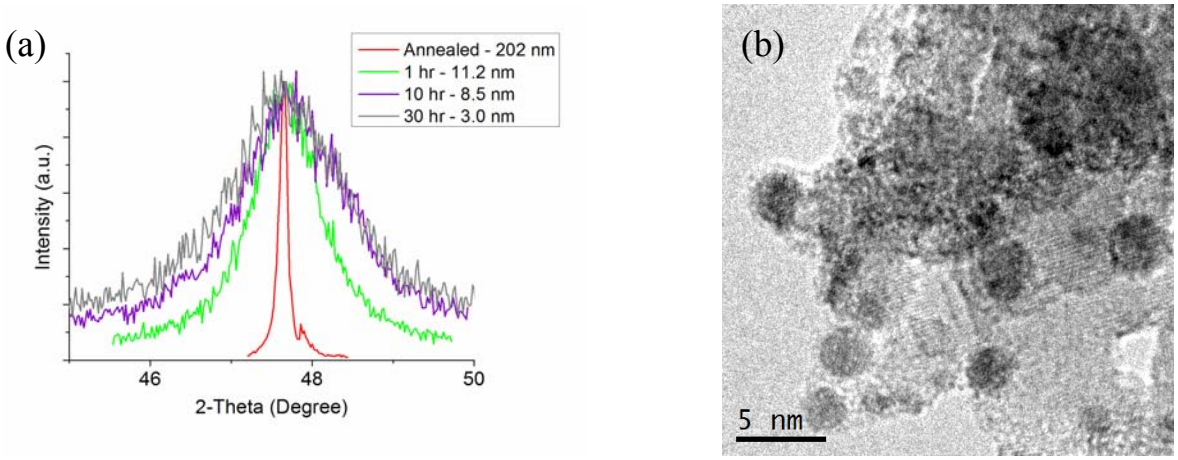

Fig. 1. (a) XRD line profile of ZnO plane (012) (b) TEM image of ZnO with average crystal size of 3.0 nm

In Figure 2, the peak emission of as-received ZnO shifts from 617nm to 677nm for annealed ZnO. The annealed ZnO at 1200°C has a peak emission at 677 nm. Annealing at extremely high temperature has possibility of causing an outward diffusion of Zinc [4]. Therefore, it is likely that this emission has a strong relationship with the presence of zinc vacancies. Less oxygen vacancies will be formed as the atmosphere has a substantial amount of oxygen that suppresses the latter's formation.

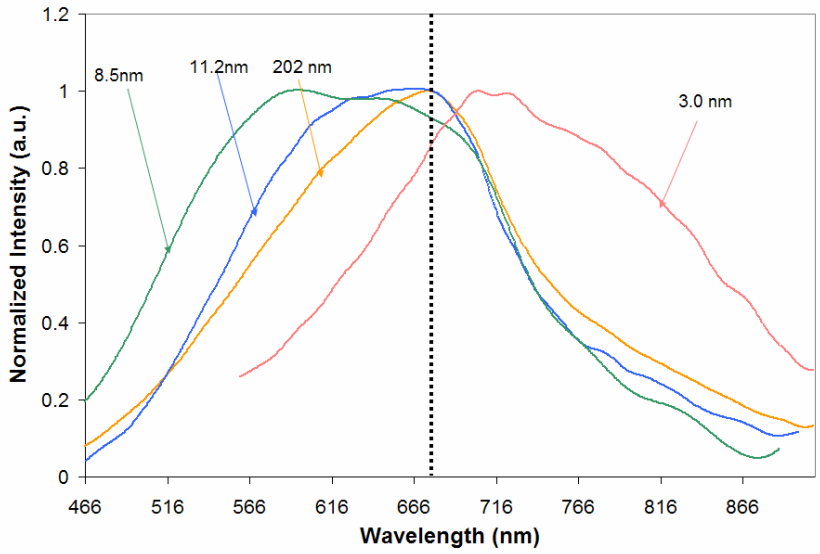

Fig. 2. Photoluminescence of ZnO of various crystal sizes. Annealed ZnO has a crystal size of 202 nm.

When the crystalline size reduces to 11.2nm its peak emission remains at 677nm, however, the emission spectrum for each individual begins to broaden in the direction of shorter wavelength (higher energy) towards the green region. Since the size shrinks, the materials surface area begins to increase. This might induce tension between the binding atoms which has a higher probability of inducing oxygen vacancies which cause the broadening of the PL towards the green region. With much surprise while we are expecting the green emission band of the 3 nm ZnO nanocrystal to enhance, the emission peak red-shifts to ~701 nm instead, forming a red emission band. It is not clear why there is a dramatic red shift although a shifting of the emission band towards shorter wavelength would be expected as a result of quantum size effect. It is likely that when the crystalline size is reduced tremendously, the surface area would be expected to increase and this causes distortion on the surface structure which induces vacancies on the surface. On the other hand the occurrence of the quantum size effect is coupled with the aforementioned situation and drastic change may occur. For example the band structure/electronic structure is drastically altered since it is dependent on the lattice structure via arrangement of the atoms and important contributions from the vacancies as well as the interaction between atoms [5]. In this manner, the red emission might form due to changes in the bandgap. Its emission mechanism is currently investigated and will be available in the future.

5. Conclusions

In conclusion, ZnO can be physically reduced to nanoscale of less than 5 nm. While the size is reduced, oxygen vacancies are formed causing broadening of the PL emission towards the green region. The PL emission however red shifted when the size reaches less than 5 nm. Such shift could probably be attributed to the coupling of the lattice distortion and oxygen vacancies that induces changes to the electronic band structure.

6. Acknowledgement

The author would like to thanks Dr Chen Peng from Institute of Materials Research and Engineering (IMRE, A*Star, Singapore) and Dr Jacques Plevert for their kind assistance.

References

[1] X.L. Wu, G.G. Siu, C.L. Fu and H.C. Ong, *Appl. Phys. Lett.* **78**, 2285 (2001).
[2] A.V. Dijken, E.A. Meulenkamp, D. Vanmaekelbergh and A. Meijerink, *J. Phys. Chem B.* **104**, 1715 (2000).
[3] S.A., Studenikin, N. Golego and M. Cocivera, *J. Appl. Phys.* **84**, 2287 (1998).
[4] Z.Q. Chen, S. Yamamoto, M. Maekawa, A. Kawasuso, X.L. Yuan and T. Sekiguchi, *J. Appl. Phys*. **94**, 4807-4812. (2003).
[5] M.J. Carey, T. Block and B.A. Gurney, *Appl. Phys. Lett.* **85**, 4442 (2004).

Mössbauer Analysis of Iron Sites in Four Na- and Ca-Saturated Ferruginous Smectites

A. Thomson[a], J.D. Cashion[a] and W.P. Gates[b]

[a] *School of Physics, Monash University, Victoria 3800, Australia.*
[b] *Department of Civil Engineering, Monash University, Victoria 3800, Australia.*

^{57}Fe Mössbauer spectra of the Na- and Ca-saturated forms of four ferruginous smectites, having a range in composition, have been fitted with Voigtian profiles to represent, principally two, correlated distributions of isomer shifts and quadrupole splittings. Correlation between the areas and hyperfine parameters of the distributions determined from Mössbauer spectroscopy and those from chemical analyses and infrared spectroscopy enable interpretations in terms of near neighbour cations in the octahedral sheet.

1. Introduction

Many techniques have been used to determine the distribution of cations in smectites [1-5], but the results are debatable because different techniques sample clay chemistry differently. Smectites are 2:1 layer (tetrahedral:octahedral) clay minerals: within the octahedral sheet, some Al^{3+} is substituted by Fe^{3+} and Mg^{2+}. Two of three octahedral sites within the $AlO_4(OH)_2$ (gibbsite-like) sheet are occupied. The metal ions within these sites form a trigonal array so each atom has three neighbours. The distribution may be statistical, but there is a tendency for Mg^{2+} ions to avoid being neighbours and thus some clustering of other ions may occur [2, 3, 5]. The tetrahedral sheets are predominantly SiO_2, but some Al^{3+} for Si^{4+} substitution can occur there as well.

Mössbauer spectroscopy has in the past been used to identify different iron sites in minerals, but this has often been subject to heated discussion [6]. For several decades, Lorentzian fitting of two quadrupole split doublets have been commonly attributed to *cis*- and *trans*-coordinated Fe^{3+} [7-8]. However, it has recently been pointed out [9] that the effect of the different neighbours on the quadrupole splitting is probably larger than that caused by *cis*- or *trans*-coordination. Rancourt [6, 9] has strongly advocated that Mössbauer spectra of inhomogeneous materials should be fitted with Voigtian lineshapes. Since the Voigtian is essentially a Gaussian distribution of Lorentzians, the Gaussian component allows the incorporation of the broadening caused by variation in the identity of neighbours.

2. Sample preparation

We have applied a Voigtian curve fitting procedure to the room temperature Mössbauer spectra of four ferruginous smectites (Table 1), prepared in their Na^+- and Ca^{2+}-forms, in order to study the octahedral occupancy. The Ca^{2+}-form of the same samples have been studied by infrared and chemical analysis [4].

Table 1. Useful site data of the smectites studied.

Clay	Oct Fe	Oct Al	Oct Mg	Oct charge
	per unit cell			%
Stebno	1.79	1.87	0.50	3
Drayton	1.02	2.18	1.06	27
Nibost	0.90	2.26	1.03	37
Redhill	0.77	2.50	0.74	87

3. Results

A representative fit of the Mössbauer spectrum for Na-Nibost smectite is shown in Fig. 1 and full tabulation of the major parameters from the quadrupole splitting distribution fits for all smectites is shown in Table 2. Note that two main quadrupole splitting groups were

observed, one with a narrow splitting distribution (ND) and one with a broad splitting distribution (BD). Perusal of Table 2 shows that the results of fitting are not systematic as a function of iron content.

Table 2. Hyperfine parameters obtained from the Voigtian fitting of the Mössbauer spectra.

Clay	Ca form									
	Narrow distribution					Broad distribution				
	IS	QS	SD	Skew	Area	IS	QS	SD	Skew	Area
	mm/s	mm/s	mm/s		%	mm/s	mm/s	mm/s		%
Stebno	0.35	0.45	0.18	0.08	81	0.33	0.72	0.39	0.29	19
Drayton	0.36	0.48	0.04	~0	55 (57)	0.34	0.86	0.32	0.04	42 (43)
Nibost	0.35	0.50	0.13	~0	57 (63)	0.36	0.94	0.38	0.08	33 (37)
Redhill	0.34	0.45	0.06	~0	61 (62)	0.34	0.90	0.47	0.28	37 (38)

Clay	Na form									
	Narrow distribution					Broad distribution				
	IS	QS	SD	Skew	Area	IS	QS	SD	Skew	Area
	mm/s	mm/s	mm/s		%	mm/s	mm/s	mm/s		%
Stebno	0.35	0.45	0.19	0.11	77	0.34	0.78	0.46	0.42	23
Drayton	0.35	0.51	0.04	~0	74 (77)	0.37	1.06	0.17	~0	22 (23)
Nibost	0.35	0.51	0.06	~0	62 (65)	0.35	0.98	0.38	~0	34 (35)
Redhill	0.35	0.45	0.15	0.02	38 (47)	0.32	0.80	0.47	0.40	43 (53)

Area values in parentheses are corrected to show the proportions of the Fe^{3+} components only.
Skew = (mean – mode) / standard deviation

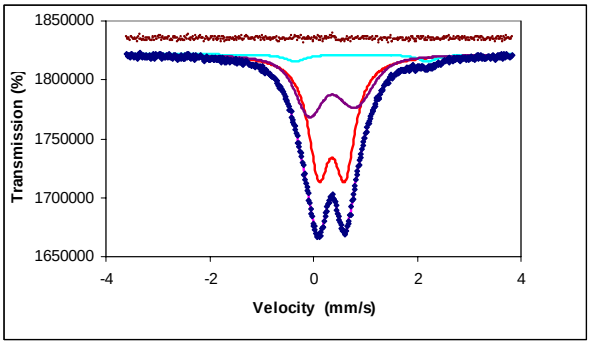

Figure 1. Best fit of the Mössbauer spectrum of Na-Nibost smectite using Voigtian profiles.

3.1. Mössbauer-based Interpretations.

The quadrupole splitting (QS) is principally determined by the charge distribution of the nearest neighbours which produces an electric field gradient (EFG) at the Fe^{3+} site. A comparison of the three ions shows that Al^{3+} has the same charge as Fe^{3+} but a smaller diameter (0.051 nm c.f. 0.064 nm) while Mg^{2+} has almost the same radius (0.066 nm) but a different charge. The larger intensity of the ND distribution in the Stebno samples strongly suggests that it is associated with an absence of Mg^{2+} neighbours. Including Mg^{2+} as nearest neighbours may correspond to the BD distribution and increases in its standard deviation (SD) correspond to an increased number of Mg^{2+} neighbours. The smaller charge of Mg^{2+} causes an increase in the EFG and hence the QS. However, it is unclear how lattice relaxation due to the smaller Al^{3+} would affect the EFG. Also unexplained are the changes in peak areas invoked by changing exchange cations.

3.2. A Combined Mössbauer – Infrared Interpretation

The distribution of the OH-sharing octahedral cation pairs, based on infrared absorption spectra [2, 4, 5], enables us to simulate an octahedral layer for each smectite. The distribution of the three neighbours about an Fe^{3+} centre, as shown in Fig. 2 for Redhill, can be estimated and compared with the number expected from simple Poisson statistics. The main reason for the observed difference is the avoidance of OH-sharing Mg–Mg neighbours, as MgMg-OH absorption bands are not observed in the IR. The net effect then is to increase the population

in the 111 centre of the plot, corresponding to a central Fe having $1Fe^{3+}$, $1Al^{3+}$, $1Mg^{2+}$ as neighbouring cations.

The ND feature is therefore probably attributable to Fe^{3+} centres having no Mg^{2+} neighbours. These are principally of 210 and 120 coordination for the four smectites studied here. The larger SD for Stebno may be due to an appreciable number of 300 coordination, which the other smectites lack. It is expected that in the Ca^{2+}- form, Ca^{2+} ions are located in the interlayer as close as possible to sites of substitution (Mg for Al in the octahedral sheet and Al for Si in the tetrahedral sheet) to achieve charge neutrality over a smaller distance.

Changing from Ca^{2+}- to Na^{+}- form creates twice as many ions in the interlayer space in preserving charge neutrality. For Stebno, Drayton and Nibost, there is a decrease in BD QS in the Na^{+}-form compared to the Ca^{2+}-form. A large proportion of Na^{+} ions are neutralising layer charge not associated with Mg^{2+}, but rather with tetrahedral Al^{3+}. For Redhill nearly 90% of exchangeable Na^{+} neutralises charge associated with octahedral Mg^{2+}. In the Ca^{2+}-forms of Nibost, Drayton and Stebno, the Ca^{2+} is potentially "close" to all the Mg, and acts to reduce the EFG effect caused by Mg^{2+}. However, Ca^{2+} can only be "close" to about half the Mg in Ca^{2+}-Redhill. Exchanging with Na^{+} improves the charge neutralisation effect on the EFG for Redhill, but introduces more disorder for the other three Na^{+}-form smectites.

The main mystery remaining is why the QS of Redhill is markedly less than Drayton and Nibost. This could be due to the larger number of symmetrical 030 coordination or lower Mg^{2+} concentration. It may also be possible that Fe^{3+} is even more clustered within the octahedral sheet of this smectite than can be discerned by IR, as has been shown recently for other montmorillonites [5, 6, 7].

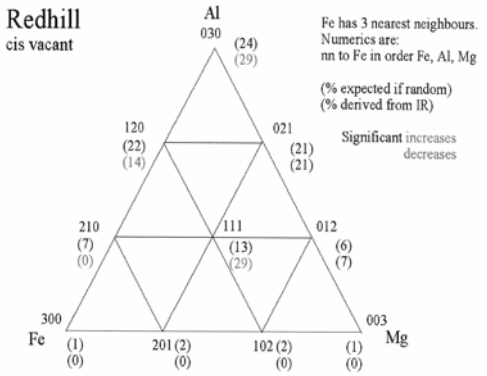

Figure 2. Distribution of Al, Mg and Fe about an Fe centre in the octahedral sheet of Redhill smectite.

In conclusion, our results provide strong evidence that aspects of Mössbauer spectra for 2:1 layer silicates can be largely explained by the identity of neighbouring cations. We emphasise here that Mössbauer spectroscopy should be used in combination with other spectroscopic tools such as infrared and X-ray absorption spectroscopy.

Acknowledgments

We are grateful for the support of the Australian Research Council and Monash University for this work.

References

[1] W.P. Gates, P.G. Slade, A. Manceau and B. Lanson, *Clays Clay Min.* **50,** 223 (2002).
[2] D. Vantelon, M. Pelletier, L.J. Michot, O. Barres and F. Thomas. *Clay Min.* **36,** 369 (2001).
[3] D. Vantelon, E. Montarges-Pelletier, L.J. Michot, V. Brios, M. Pelletier and F. Thomas. *Phys. Chem. Min.* **30**, 44 (2003).
[4] W.P. Gates, in *Vibrational Spectroscopy of Layer Silicates and Hydroxides*, ed. T. Kloprogge (The Clay Minerals Society, Eurora, 2005) CMS Workshop Lecture Series Vol 13, p 125.
[5] W.P. Gates, in *Handbook of Clay Science*, eds. F. Bergaya, B.K.G. Theng and G. Lagaly (Elsevier, Amsterdam, 2006) Developments in Clay Science, Vol. 1. p 789.
[6] D.G. Rancourt, *Phys. Chem. Min.* **21,** 250 (1994).
[7] G. Besson, A.S. Bookin, L.G. Daynyak, M Rautureau, S.I. Tsipursky, C. Tchoubar and V.A. Drits, *J. of Appl. Crystal.* **16,** 374 (1983).
[8] G. Besson, V.A. Drits, L.G. Daynyak and B.B. Smoliar, *Clay Min.* **22,** 465 (1987).
[9] D.G. Rancourt and J.Y. Ping, *Nucl. Instr. Meth.Phys. Res.* **B58,** 85 (1991).

EPR and Antioxidant Efficiency studies of Resveratrol, Quercitin and Fisetin

G.J. Troup, [a], D.R. Hutton[a], L. O'Dea [b] and S.J. Langford[b]

[a] *School of Physics and* [b] *School of Chemistry, Monash University, Victoria 3800, Australia*

Resveratrol (a stilbene), Quercitin and Fisetin (flavonols) are polyphenols found in red wine, the last to a small extent. They behave differently physiologically in humans. Can EPR and antioxidant efficiency tests distinguish between them? The antioxidant efficiency was effectively 100% in all: both the flavonoids showed a similar free radical signal, but the Fisetin sample was clearly contaminated by transition metal ions. The Quercitin free-radical signal was markedly different.

1. Introduction

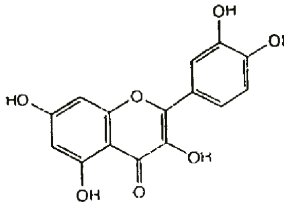

Quercitin

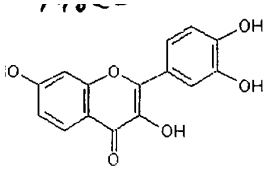

Fisetin

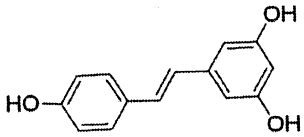

trans-resveratrol

EPR (**E**lectron **P**aramagnetic **R**esonance: also ESR, E **S**pin R) is a well established spectroscopic technique exploiting the precession of electron spins about a constant magnetic field [1]. It can reveal free radicals and certain paramagnetic ions. Its use in the wine industry has been established by this group[2]. Stable free radicals in wines occur mainly on polyphenols, [2], known to be antioxidants. The most potent antioxidant in red wine is the stilbene Resveratrol [3]. Quercitin is the most abundant flavonol found in red wine [4]. Both these compounds now appear in 'dietary supplements'. The flavonol Fisetin is also in red wine but to a much lesser extent. It has recently been shown to improve the memory of laboratory mice, which Quercetin does not do. Is this a matter of different free radical behaviour, or of the stereochemistry? How different are the antioxidant efficiencies? These were the problems we set out to investigate in these three molecules.

2. Sample preparation

Resveratrol powder (99% pure) was obtained from China. Both Quercetin and Fisetin were purchased in solid powder form (99% pure) from Sigma. A specimen of each was placed in a standard EPR quartz tube (Wilmad), and the EPR measurements done at room temperature on all 3, and at 77k for Resveratrol. A Bruker X-band (~ 9.4 GHz) spectrometer was used.

The sample preparation and the antioxidant efficiency test are described in [5]. Briefly, free radicals are created in a solution at a constant rate, giving an increasing absorption in the UV. An antioxidant will decrease the absorption, so an efficiency can be calculated. Since Resveratrol not attached to a sugar is almost insoluble in water, the antioxidant efficiency tests were carried out in methanol instead of aqueous solution.

3. Results

3.1 EPR measurements

The EPR spectrum of Resveratrol over a 100 Gauss sweep was a single structureless line ~8 Gauss wide, which at room temperature did not reach maximum amplitude (saturate) until the power was 100mW. To test for temperature broadening of the line, the measurements were repeated at 77k, but the linewidth stayed the same. This is quite different to the flavonol behaviour described below.

The EPR spectrum of Quercitin over a 100 Gauss sweep was a single structureless line, ~ 4 Gauss wide, which reached maximum signal strength at 2 mW power, and then decreased with power increase (saturation.). The 1mW power spectrum of the Fisetin sample is shown in Fig. 1: the free radical line is marked.

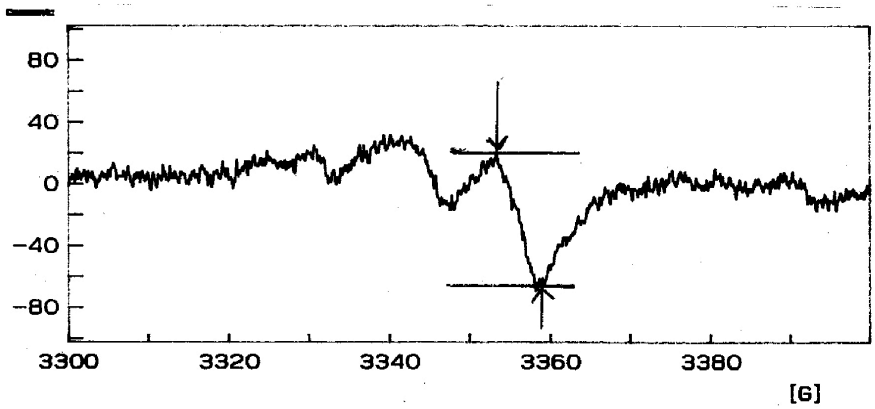

Figure. 1 EPR spectrum of 'fisetin', power 1mW. Axes: horizontal, magnetic induction, Gauss; vertical, signal strength, arbitrary units.

How was this line identified? - by its behaviour in the 15 mW spectrum (Fig. 2). The marked line has decreased in size, while the other lines have increased. The other lines therefore are not from the phenolic radical, and are due to transition metal ion impurities.

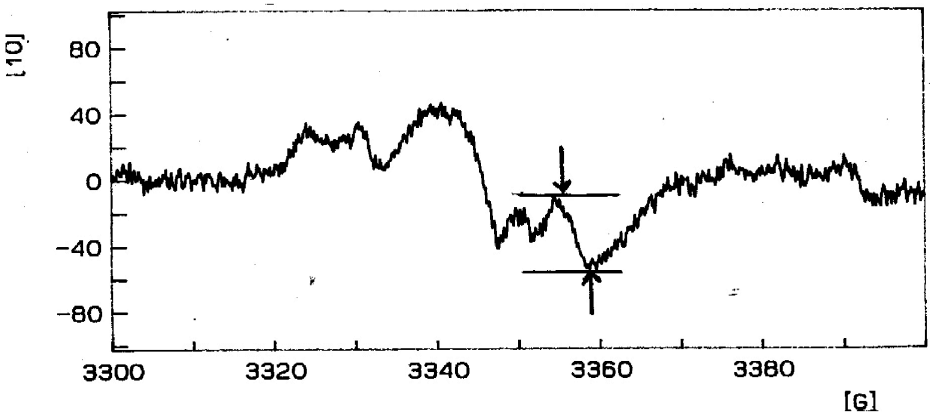

Figure.2. Same as for Fig.1, but power 15mW.

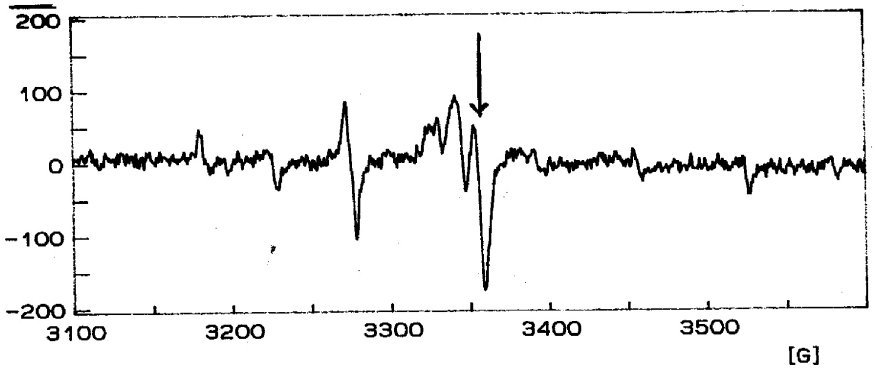

Figure.3 Broader magnetic induction range for fisetin, power 2mW. Axes as for Fig.1.

Fig. 3 shows a broader sweep spectrum at 2mW. Some of the smaller lines (regularly spaced) can be attributed to Mn(2+): the larger line left of centre can be assigned to Cu(2+), and the large line next to the free radical to Fe(3+), by g-values (See details for individual ions in [1]).

3.2 Antioxidant efficiency.

The antioxidant efficiency results for both flavonoid specimens were 100 +/- 5%. That for vitamin E was its usual 95 +/- 5%. The Result for Resveratrol in methanol was 96%, while for vitamin E was 91%, both +/- 5%.

4. Discussion.

The EPR behaviour of Resveratrol is very different from that of the flavonoids. The high antioxidant efficiency is to be expected from previous studies [2]. It may well be that the EPR behaviour, as well as the structure of this molecule, are responsible for its antioxidant and other properties.

The Quercetin and Fisetin EPR behaviours are very similar, perhaps to be expected from their structural similarity. The powerful antioxidant behaviour of Quercetin is well known. The problem is, how much of the measured antioxidant efficiency of the Fisetin sample was due to the metal antioxidant impurities? We need a pure sample to know.

However, to our knowledge, the purity of commercially available samples is measured via Thin Layer Chromatograpy or High Performance Liquid Chromatography, which previous experience has shown DO NOT DETECT PARAMAGNETIC IONS!

Note added during Conference

Professor G. Scollary, Wine Science and Agriculture, Charles Sturt University, informed us that the performance of the well known antioxidant, ascorbic acid, which is used in the wine industry, is affected by the presence of transition metal ions!

References

[1] D.J.E. Ingram *Biological and Biochemical Applications of E.S.R.* (1969), Adam Hilger, London UK
[2] G.J. Troup and C. Hunter *Ann.N.Y.Acad.Sci.* **957**, 345 (2002)
[3] W. Bors and C. Michel, *Ann.N.Y.Acad. Sci.* **957**, 57 (2002)
[4] A.L. Waterhouse, *Ann.N.Y.Acad.Sci.* **957,** 21 (2002)
[5] I. Cheah, J. Kelly, S.J. Langford and G.J. Troup, *Proc. 27th Ann. Cond. Matter Mater. Meeting,* http://aip.org.au/content/publications (2003)

EPR and Antioxidant Studies of Dark Chocolate, a Red Wine Vinegar and a Cider Vinegar

G.J. Troup[a], D.R. Hutton[a], L. O'Dea[b] and S.J. Langford[b]

[a] *School of Physics, and* [b] *School of Chemistry, Monash University, Victoria 3800, Australia*

Dark chocolate (>70% cocoa) contains Cu and polyphenols. The EPR has not been reported before. From both Swiss and Australian samples, it shows Cu++ and a very strong free radical signal, as well as unreported Mn++. Cider vinegar has a strong reputation in alternative medicine for healthgiving effects. Some might be due to antioxidants? Red wine vinegar must have some antioxidants. So both were examined by EPR and antioxidant efficiency tests. From a 'reputable' sample of each, the EPR spectrum was due to Mn++, and there was no free radical signal. The Antioxidant efficiency for cider vinegar was 63%, and that for red wine vinegar, 85%: errors +/- 5%.

1. Introduction

EPR (Electron Paramagnetic Resonance, also ESR, E Spin R) is a well established spectroscopic technique [1] using electron spin precession in a constant magnetic field. It can detect free radicals and certain paramagnetic ions in appropriate valence states: eg, Cu+ is not detected, Cu++ is. EPR therefore has many uses, including chemical analysis. Properties of the detected spectra can help to understand ionic surroundings, and the activity of free radicals.

Dark chocolate (>70% cocoa) contains Cu and polyphenols. The EPR spectrum has not been reported: it could show a Cu++ signal, should show a strong free radical signal, and maybe others. Cider vinegar has an 'alternative medicine' reputation for its healthgiving properties [2]. Some of these could be due to antioxidant action. Red wine vinegar should contain some antioxidants, even if only the anthocyanins [3]. Antioxidant efficiency measurements are complementary to EPR. The comparisons are worth while: after all, vinegar is used in cooking and in salad 'dressing', and red wine vinegar is certainly part of the 'Mediterranean diet'.

2. Sample preparation

Dark Swiss (85% cocoa) and Australian (75% cocoa) chocolates were purchased from a local supermarket. Samples were scraped from each with a plastic knife, and placed into standard quartz EPR tubes (Wilmad). The measurements were carried out with a Bruker x-band (~9.4 GHz) EPR spectrometer at room temperature (20C).

A 'good' imported Italian wine vinegar, and a 'good' imported American unfiltered (cloudy) cider vinegar were purchased from a local supermarket. The cloudy cider product was chosen because it might contain more antioxidants. Recent work published *after* our work was done has verified this surmise [4]. A sample of each was cold evaporated down to 1/10 of its original volume, and a portion of each sample was placed in a standard EPR tube. The preparation for the antioxidant test, as regularly used by this group, as well as the test itself, are described in [5]. In the test, free radicals are generated in a solution at a constant rate, giving an increasing absorption in the UV. The antioxidant will reduce this absorption rate, so

an efficiency can be determined. For the EPR work, it was necessary to freeze the samples, to avoid microwave losses.

3. Results

3.1 EPR results

The Swiss dark chocolate EPR spectrum is shown in Fig 1. The Australian specimen result is almost the same. The truncated signal is from the stable free radicals on the polyphenols [3]. The broad signal is from Cu++, and some of the small narrow lines are from Mn++, previously unreported [1]. A spectrum taken 6 weeks later on the same specimen left exposed in the laboratory showed a reduced Cu++ line, and the Mn++ and free radical lines had almost vanished. EPR of milk chocolate, under the same procedures, showed the Cu++ line, but the free radical line was enormously reduced, and somewhat broadened: milk products give such a line [6].

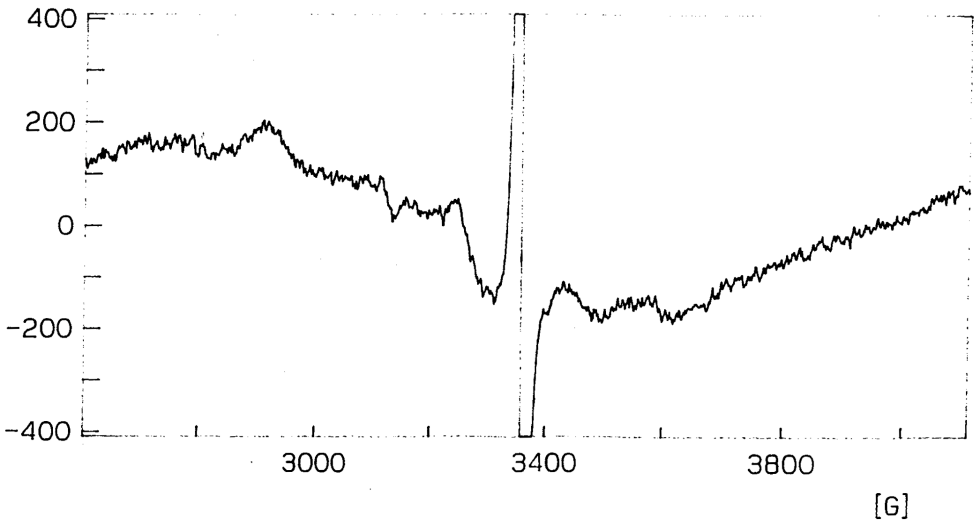

Figure 1. EPR spectrum of Swiss chocolate. Horizontal axis: magnetic induction, Gauss. Vertical axis signal strength, arbitrary units.

The wine and the cider vinegar spectra, taken under the same conditions, are almost identical (except that of the cider vinegar is less intense) so only the red wine vinegar spectrum is shown (Fig.2). The signal is from Mn++, very similar to that from wines [3].

The vinegar spectrum display is phase reversed with respect to the chocolate one. The transition is between the electron spin states (+1/2) to (-1/2): the six large peaks are due to hyperfine structure, since the Mn nuclear spin is 5/2.The small lines in between are due to 'forbidden transitions', showing that the Mn ion is in a comparatively low symmetry site for both vinegars. A free radical signal would be a single narrow line, placed at the centre of the Mn++ spectrum. Note that the free radical signal for chocolate is not at the centre of the broad line, which helps identify it as Cu++.

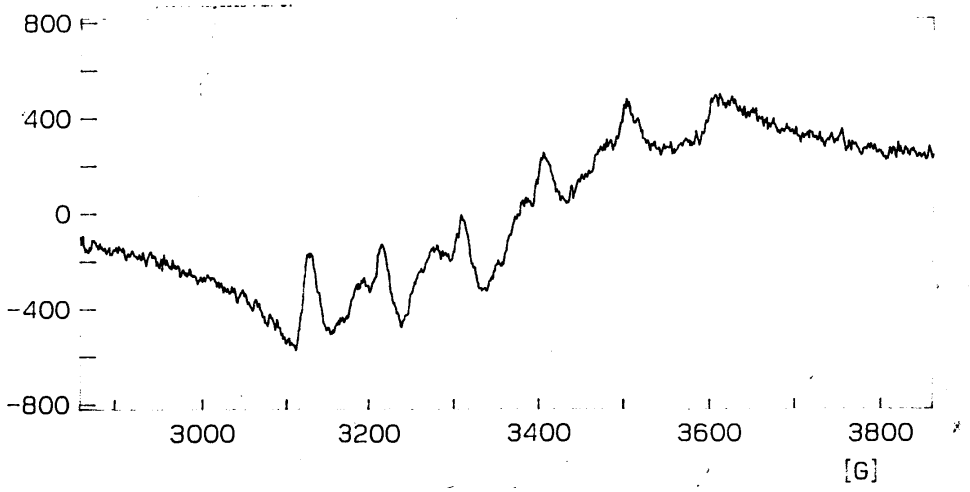

Figure 2. EPR spectrum of red wine vinegar. Horizontal axis: magnetic induction, Gauss. Vertical axis, signal strength (arbitrary units).

3.2 Antioxidant efficiency results.

The antioxidant efficiency for the red wine vinegar was 85% and for the cider vinegar, 63%, both +/- 5%, a significant difference.

4. Discussion

The dark chocolate contains Cu as Cu++, as verified. The Mn++ has not been previously reported. The diminution in all signal intensities after exposure to the air shows that the antioxidants are at work. The absence of the large free radical signal in the milk chocolate indicates that the inactivation of the polyphenol antioxidant action may already have taken place.

The similarity in the EPR spectra of the vinegars is to be expected, since both wine and cider are fermented fruit juices. The wine vinegar contains anthocyanins, the cider does not. Cu is known to 'hide' from EPR as Cu+, but is known to occur in wine. There must be fewer remaining polyphenols in the cider vinegar, because there would have been less to start with. So with hindsight, the results are explainable. Of course, further work on further samples needs to be done, but red wine vinegar has been a part of the 'Mediterranean Diet' for a long while!

References

[1] D.J.E. Ingram, *Biological and Biochemical Applications of ESR* (1969) Adam Hilger Lt., London UK

[2] S. Merson, *The 100 Best Foods* (2007) Duncan Baird/Simon & Schuster

[3] G.J. Troup and C.R. Hunter, *Ann.N.Y.Acad. Sci.* **957**, 345 (2002)

[4] J. Oszmianski, M. Wolniak, A. Wojtylo and I. Wawer, *J. Science Food and Agriculture* **87,** 573 (2007)

[5] I. Cheah, J. Kelly, S.J. Langford and G.J. Troup, *Proc. 27th Ann. Cond. Matter Mater. Meeting,* http://aip.org.au/content/publications (2003)

[6] G.J. Troup, P. Crisp, E. Scott, J. Boas, D. Hutton and I. McKinnon, *Proc. 30th Ann. Cond. Matter Mater. Meeting,* http://aip.org.au/content/publications (2006)

Improving Student Engagement in 3rd Year Condensed Matter Physics: A Case Study.

K. F. Wilson[a] and D.J. Goossens[a,b]

[a] *Department of Physics, Australian National University, ACT 0200, Australia.*
[b] *Research School of Chemistry, Australian National University, ACT 0200, Australia.*

In 2004 the authors took over the third year solid state physics course at the ANU, which at that time had an enrolment of 10 students. Since then the course has been updated to include a range of interesting assessment tasks and a more open-ended laboratory course. In 2006, 41 students completed the course. The reasons for increased participation are discussed in this paper.

1. Introduction

In 2004, PHYS3032, Condensed Matter Physics (CMP) was a typical third year physics course at the ANU, with an enrolment of 10 students. In 2005 the enrolment doubled to 20 students, and in 2006 a total of 41 students completed the course, the highest of any third year physics course at the ANU. The course is the only solid-state-physics taught at the ANU, and the only exposure to the field for most physics students. Low popularity had meant that most physics undergraduates studied no condensed matter physics. The authors took over the course in 2004 determined to rectify this, not only because it is disappointing to teach an unpopular course, but more importantly because condensed matter physics is a key field of physics and a large fraction of physicists are engaged in solid state research and/or development. Many physics courses at the ANU do not include a lab component, so it is possible for a student to graduate with a physics degree having done no laboratory work since first year. Laboratory work is however a major component of this course.

The course curriculum was adjusted and modified from 2004 to 2006 following principles of good teaching and learning abstracted from education research (e.g. [1-3]), and using student feedback solicited from course evaluation surveys, focus groups, anonymous discussion boards and personal conversations. While this feedback has contributed to course development, only some of the suggestions have been implemented. Greater effort has subsequently been put into explanations for the students about the rationale for each assessment task and the modes of learning used in the course. The changes made are discussed below.

2. The evolution of PHYS3032

In 2004 the course consisted of 30 lectures, a few tutorials and a laboratory component of 15 to 18 hours lab work. The lectures covered the basics of solid state physics in a traditional fashion, beginning with an introduction to reciprocal space and diffraction techniques then moving on to crystal binding, phonons, electronic states in solids, Fermi surfaces and their significance, semiconductors and an introduction to superconductivity and magnetism. The textbook was Kittel [4]. The course finished with six lectures on ‘soft’ CMP and two on statistical mechanics. The assessment prior to 2004 was a traditional mix of laboratory reports, textbook problem set assignments and examination. 10 students enrolled in 2004, a typical number for this course at the time.

In 2004 we introduced two open-ended assignments: a short essay and a talk. These supplemented two problem set assignments, and unassessed tutorial problem sets. For the essay, students were given a range of topics but could also choose their own topic relevant to the course material. The short talk was to be about any application of semiconductors or

superconductors. Essays were put on a website so students could read others' work. The essay and talk tasks were chosen firstly to encourage students to learn in more depth about one topic and engage in deeper learning [2]. Secondly, by choosing a topic of interest, a task can be more motivational than a set of text-book problems [3]. Thirdly, such tasks build generic skills, such as information literacy and communication (both written and oral presentation), addressed in few other assessment tasks throughout ANU physics courses. Tutorials throughout the semester provided problem sets. These were not assessed, but provided practice in examination problems, however students had to motivate themselves to attempt problems not completed in the tutorial.

With such a small number of students, course evaluation surveys have low statistical certainty, however the feedback was generally positive at the end of 2004. More importantly, the enrolment in 2005 doubled to 20 students.

In 2005 the laboratory component of the course was heavily revised, and the experiment workbooks rewritten to encourage students to think and question, and to extend the experiments where possible. Students could select which experiments they would do, subject to equipment availability. One new experiment in X-ray diffraction introduced students to 'real' research equipment and techniques. Students worked in pairs in the laboratory, and many experiments now had 3, 6 or 9 hour options, encouraging collaboration and self directed learning [3]. For assessment, students kept a laboratory logbook and wrote formal reports. Previously, many students had poor record-keeping skills, owing to limited laboratory experience.

In 2005 the syllabus of the course included a large component of statistical mechanics, replacing the 'soft' condensed matter. This part of the course was unpopular with students in 2005 partly because staff constraints required it to be taught out of sequence. As a result feedback and student evaluation were very mixed. Nonetheless, enrolments again increased in 2006.

In 2006, the course had more students than any other third year physics course, with the enrolment doubled to more than 40. The course content returned to the 2004 syllabus, but now with 9 'soft' CMP lectures. A new challenge was how to deal with the increased numbers, given limited laboratory resources and time. Additional experiments were added to the course, and two new experiments in electron microscopy were piloted. The students wrote a set of instructions for these experiments in place of an experiment report. One pair of students satisfied the requirements with a project in which they bought equipment, set up and tested an YBCO synthesis facility, and tested their own sample. They then wrote a report on their project and a description of the experiment for YBCO synthesis and characterisation. This was an extremely valuable experience for these students *and* added a new experiment to the course. Student writing of experiment instructions proved a far more valuable learning experience than was anticipated. The students reported that the exercise prompted them to think about not only the relevant experiment but also previous experiments. (The laboratory work for 2007 will consist of 18 hours chosen from: thermodynamics of Peltier devices, X-ray diffraction, magnetic susceptibility, energy gap in semiconductors, Hall effect, synthesis of YBCO, superconductivity of YBCO, magnetic hysteresis, diffraction and imaging using electron microscopes.)

The first assignment in the course in 2006 was made flexible by students choosing between an essay, a web page or 'other' activity in consultation with the lecturer. 'Others' proved extremely creative *and* enjoyable to mark, including a play about zombies that obey the nearly-free-electron model, a hands-on classroom exercise on digital logic with teacher's notes, a lattice/phonon simulator and a board game, Vortex! [5]. Students reported that they enjoyed these assignments, although some expressed concern that were not solving problems as examination preparation (problems were provided but not marked). The second assignment

was a student-run symposium, for which students had to present a talk or a poster. Students who had presented fewer than three talks previously at ANU were required to speak. Again, this assignment was designed to be motivational and help development of generic skills as well as an in-depth knowledge of a topic in CMP. The afternoon-plus-evening symposium included a dinner with a speaker invited from ANSTO. It was completely student run, and peer assessed, and was an extremely enjoyable completion to the course showcasing the students' abilities as well as the aspects of condensed matter physics they found most interesting. The student ownership of the entire event both reduced workload for the lecturers and improved the atmosphere of the event – the course lecturers became guests of the students. Handing over some power and responsibility to students was a very successful way to end third year physics.

3. Conclusions and Implications for Course Design

Designing a course which gave students choice in some assessment tasks (e.g. assignment topics and experiments) increased student motivation for those tasks *and* for the course material overall. Collaborative learning improves motivation and helps students develop organisational and communication skills. The collaborative student-run symposium gave students a sense of ownership of this part of the course. These initiatives increase student motivation, improve generic skills and encourage deep learning.

Such tasks do not completely replace, but rather supplement and enhance, problem sets and exams. Nor do they require that something else goes from the syllabus. The syllabus for PHYS3032 was the same in 2006 as in 2004, and 2003, but it was a very different course in terms of student learning outcomes, and in enrolments. Some flow on is expected with more students opting to do research in CMP. Students from recent years' classes have gone on to take up a year-in-industry position with one of Australia's leading condensed matter research institutions and to present work and publish research at this Annual Condensed Matter and Materials meeting. Even those who do not continue in the field will still have an enhanced regard for CMP, something potentially important for any tasks they might perform on future committees and advisory groups, for government, industry, or academia.

References

[1] R. Hake, *Am. J. Phys.* **66,** 1, (1998)
[2] J. Biggs and K. Collis *Evaluating the Quality of Learning: The SOLO Taxonomy* (Academic Press, 1982)
[3] R. D. Knight, *Five Easy Lessons: Strategies for Successful Physics Teaching* (Addison Wesley, NY, 2002)
[4] C. Kittel, *Introduction to Solid State Physics.* (John Wiley and Sons, NJ, 2005).
[5] R. Barry and S. Hodgman, *Proc. 31st Ann. Cond. Matter Mater. Meeting,* http://www.aip.org/publications, (2007).

Size Dependence of Critical Transition Temperature of MgB_2

C. C. Yang[1] and S. Li

School of Materials Science and Engineering, The University of New South Wales, NSW 2052, Australia.

We have studied the effect of crystal size D on the critical transition temperature $T_c(D)$ of MgB_2 physically divided into the individual particles on the nanometre scale. It is found that $T_c(D)$ decreases with the decreasing of D. A thermodynamic model for $T_c(D)$ was established quantitatively based on the size dependence of the cohesive energy. An agreement between the model prediction and the experimental results was found.

1. Introduction

The discovery of a superconducting transition at 39 K in MgB_2 initiated enormous interest both to understand the phenomenon and to exploit its remarkable intrinsic performance for magnetic and electronic applications [1,2]. In recent years size effects on the critical transition temperature $T_c(D)$ of MgB_2 nanocrystals have been extensively investigated theoretically and experimentally with D denoting the crystal size [3-5]. When D of low-dimensional materials decreases to the nanoscale, electronic, magnetic, optic, catalytic and thermodynamic properties of the materials are significantly changed, having a substantial difference from their bulk counterparts [6]. Understanding the physical nature behind the new properties is desired for fabricating the materials for practical applications [6].

In experiments, it was found that $T_c(D)$ of the MgB_2 nanocrystals progressively reduce with D decreasing [3,4]. In our work, it has been reported that MgB_2 nanocrystals were fabricated by the physical reduction method [7]. Commercial bulk MgB_2 crystals (99% purity) were milled in tungsten carbide (WC) bowls purged with Ar. The crystal size of MgB_2 nanocrystals was determined by X-ray diffraction and verified by high resolution transmission electron microscopy. It is in a range of 2.5 to 64.1 nm (about 10% size deviation). Through measuring the magnetic moments, we find that the $T_c(D)$ decreases with the decreasing of D, which is in agreement with other experimental results. However, further theoretical work is still needed to seek the physical nature behind the T_c-suppression and a $T_c(D)$ function is highly desirable.

In this contribution, we demonstrate that the cohesive energy, E, determines a number of physical-chemical properties of nanocrystalline materials. Based on this understanding, a function to predict $T_c(D)$-suppression of superconductive nanocrystals is established in a form of a model for size-dependent cohesive energy $E(D)$. The accuracy of the developed model is verified with the available experimental data of MgB_2 nanocrystals.

2. Methodology

The profile of Lennard-Jones potential is determined by both bond strength, ε, and equilibrium atomic or molecular distance, h [8]. Note that E is the sum of ε over all the coordinates of the specific atom with coordination z, and $E = zN_a\varepsilon/2$ with N_a being the Avogadro constant (Note that only the nearest-neighbor interaction is being considered in the above formula. This is the case for $P622$-symmetried MgB_2 due to considerably weak next-nearest-neighbor interaction). Thus, the variation of the potential profile for nanocrystals,

[1] Corresponding author, Fax: +61-2-93855956, E-mail: ccyang@unsw.edu.au

which is related to the crystallographic structures and the corresponding transition functions, should be determined by the change of both E and h. In this case, the size effects on the physical-chemical function could be considered to contribute by the change of E and h. As the change of h is usually in the range of 0.1%-2.5% even when D < 20 nm [9], the size effect on h can be neglected. Therefore, size dependence of physical-chemical functions could be predicted if the $E(D)$ function is available.

Based on Ising premise, T_c is determined by the spin-spin exchange interaction $E_{exc}(T)$ [10]. The latter is the sum of a portion of the cohesive energy E and the thermal vibration energy $E_v(T)$ where T denotes the temperature [5,10], e.g. $E_{exc}(T) = AE + E_v(T)$ with A ($0 < A < 1$) being a coefficient. Based on the mean field approximation and Einstein′s relation, $E_v(T) = k_B T$ as a first order approximation with k_B denoting the Boltzmann constant [5,10]. At the critical temperature, $E_{exc}(T) \approx 0$ and the thermal vibration energy required for disordering the exchange interaction is a portion of the cohesive energy at $T = 0$ [5,10]. Thus, $T_c \propto E$. It is assumed that $T_c(D)$ has the same size dependence of $E(D)$ since the nature of any phase transition is related with the potentials of the two related phases of the crystals. As a result, $T_c(D)/T_c(\infty) = E(D)/E(\infty)$.

Combining the $E(D)$ function reported in literature [11], and the above considerations, a general correlation can be expressed as,

$$\frac{T_c(D)}{T_{cb}} = \frac{E(D)}{E_b} = \left[1 - \frac{1}{(2D/h) - 1}\right] \exp\left[-\frac{2S_b}{3R}\frac{1}{(2D/h) - 1}\right] \quad (1)$$

where S_b is the bulk evaporation entropy of crystals, T_{cb} and E_b show bulk critical transition temperature and cohesive energy, respectively, and R denotes the ideal gas constant [11].

3. Results and discussion

The modelling result with Eq. (1) is plotted to compare with the experimental results for $T_c(D)/T_{cb}$ of MgB_2 nanocrystals in Fig. 1. The solid line denotes the model prediction based on Eq. (1) where $S_b \approx 13R$ as a first order approximation, which is equal to that of the mean value of the most elements, and h = 0.352 nm [12]. The symbol ♦ with the error bars denotes our experimental results [7], Δ [3] and ∇ [4] show other experimental results.

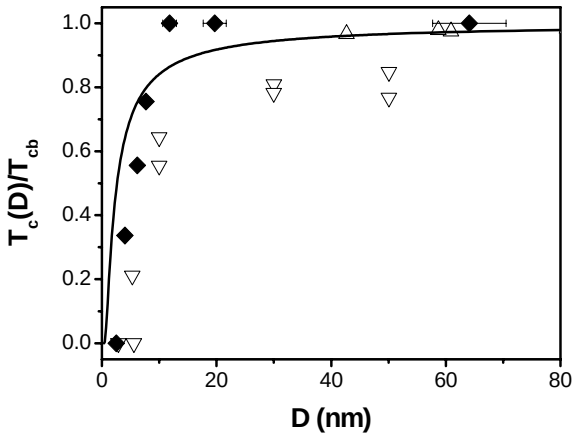

Fig. 1. $T_c(D)/T_{cb}$ function of MgB_2 superconductive nanocrystals.

As shown in this figure, $T_c(D)$ decreases with D decreasing. Although there is scatter in the experimental results, our model prediction shows the same trend as the data in a very wide span of size range. This exhibits the accuracy of Eq. (1). Certainly, there is deviation between

them since the Einstein′s relation is not accurately valid in low temperature, which needs further improvement. Note that all parameters have clear physical meaning in the developed model, which makes it easier to reveal the physical nature behind the properties.

As a general rule, $\exp(-x) \approx 1-x$ when x is small enough. In such a case, $D > 10$ nm. With the first order approximation, Eq. (1) can be rewritten as,

$$T_c(D)/T_{cb} \approx 1- [1/2+S_b/(3R)]h/D. \quad (2)$$

Eq. (2) obeys thermodynamic rule of low-dimensional materials, that the alternation of size-dependent quantity is associated with the surface/volume ratio, or $1/D$. This further supports the notion that the discussed physical-chemical properties are most likely affected by the severe bond dangling which is induced by the crystal size reduction in nanoscale. However, as the size of the nanocrystals further decreases, namely below 10 nm, the difference between Eqs. (1) and (2) becomes evident [11].

For the smallest crystals (D = 2.5 nm) in our experiments, superconductivity is completely depressed. It is noted that the thermodynamics has a statistic mechanics basis. When $D < 2$~3 nm, the particles consist of only several ten to hundred of atoms, the statistic meaning is no longer present. In addition, the crystalline structure becomes unstable due to big bond deficit where a cluster with special structure arises. In this case, the long-range ordering vanishes and the bond structures differ from the corresponding crystals. This is outside the scope of our model description since the developed model is only suitable for crystalline materials based on the consideration of a continuous medium.

It is evident from Eq. (1) that $E(D)$ (negative) increases (the absolute value decreases) with a decrease in size due to the increase of surface/volume ratio, which reflects the instability of nanocrystals in comparison with the corresponding bulk crystals [11]. If this increase for both low temperature phase and high temperature phase is almost the same, the relative energetic increase of the low temperature phase is larger than that of high temperature phase. Together with the consideration of entropy where the entropy of high temperature phase is always larger than that of low temperature phase, depression of the transition temperature between them is present.

Acknowledgments

This project is financially supported by Australia Research Council Discovery Program (Grant No. DP0666412).

References

[1] J. Nagamatsu, N. Nakagawa, T. Muranaka, Y. Zenitani and J. Akimitsu, *Nature* **410**, 63 (2001).
[2] D. Larbalestier, A. Gurevich, D. M. Feldmann and A. Polyanskii, *Nature* **414**, 368 (2001).
[3] A.V. Pogrebnyakov, J.M. Redwing, J.E. Jones, X.X. Xi, S.Y. Xu, Q. Li, V. Vaithyanathan and D.G. Schlom, *Appl. Phys. Lett.* **82**, 4319 (2003).
[4] K. Ueda and M. Natio, *J. Appl. Phys.* **93**, 2113 (2003).
[5] C.Q. Sun, W.H. Zhong, S. Li and B.K. Tay, *J. Phys. Chem. B* **108**, 1080 (2004).
[6] H. Gleiter, *Acta Mater.* **48**, 1 (2000).
[7] S. Li, T. White, C.Q. Sun, Y.Q. Fu, J. Plevert and K. Lauren, *J. Phys. Chem. B* **108**, 16415 (2004).
[8] J.E. Lennard-Jones, *Proc. R. Soc. London, Ser. A* **106**, 463 (1924).
[9] C.C. Yang, M.X. Xiao, W.Li and Q. Jiang, *Solid State Commun.* **139**, 148 (2006).
[10] R. Zhang and R.F. Willis, *Phys. Rev. Lett.* **86**, 2665 (2001).
[11] Q. Jiang, J.C. Li and B.Q. Chi, *Chem. Phys. Lett.* **366**, 551 (2002).
[12] http://www.webelements.com/

Emergence of Composite Spin-one Behaviour in Alternating Spin-1/2 Chains

Weihong Zheng[a], C.J.Hamer[a], and R.R.P. Singh[b]

[a]*School of Physics, University of New South Wales, Sydney NSW 2052, Australia;*
[b]*Department of Physics, University of California, Davis, CA 95616*

We study the alternating antiferromagnetic-ferromagnetic spin-1/2 Heisenberg chain with exchange couplings J and λJ. At small λ the antiferromagnetic bonds form spin-0 dimers, while at large negative λ the ferromagnetic bonds form spin-1 dimers. The crossover is signalled by the merging of the one-particle state with the bottom of the continuum.

1. Introduction

There has been considerable interest recently in the behaviour of the spin excitation spectrum in gapped spin-systems, when a discrete state meets the continuum [1,2]. In one-dimensional systems, the discrete state appears to merge with the bottom of the continuum [3], whereas in higher dimensional systems it appears to enter the continuum in the form of a broadened resonance [4].

Here we apply series expansion methods [5] to the alternating antiferromagnetic-ferromagnetic spin-half Heisenberg chain with Hamiltonian

$$H = \sum_i [\ \mathbf{S}_{2i} \cdot \mathbf{S}_{2i+1} + \lambda \mathbf{S}_{2i-1} \cdot \mathbf{S}_{2i}\ ]$$

This model is particularly interesting in that it interpolates smoothly between the uniform spin-half chain, when λ = 1, and the limit λ → -∞, when each alternate pair of spins form a spin-1 dimer to minimize the energy, corresponding to a spin-one chain. This model is also interesting from an experimental point of view [6], as several alternating chain compounds are suspected to have an alternating ferromagnetic/antiferromagnetic character.

Our goal here is to study the crossover in the spectrum from the dimerized behaviour near λ = 0, where the single-particle dominates the spectrum and is well separated from the multi-particle continuum, to the Haldane chain behaviour at large negative λ, where part of the single-particle spectrum begins to overlap with the two-particle continuum.

2. Energy Spectrum

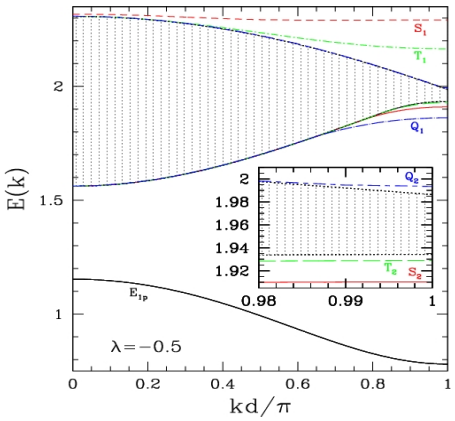

Fig. 1. The spectrum at λ = -0.5. The spacing between dimers is d.

In Fig. 1, we show the single-particle and two-particle spectra calculated for the model at a small coupling $\lambda = -0.5$. One can see that the one-particle spectrum E_{1p} has a peak at $k = 0$ and is well separated from the two-particle continuum (grey shaded). Also shown are the various bound and anti-bound states. The dominant bound and antibound states (S_1, T_1 and Q_1) in the singlet, triplet and quintuplet sectors are reversed with respect to the $\lambda > 0$ case, because the ferromagnetic interaction becomes attractive in the $S = 2$ channel and repulsive in the $S = 0$ and $S = 1$ channels.

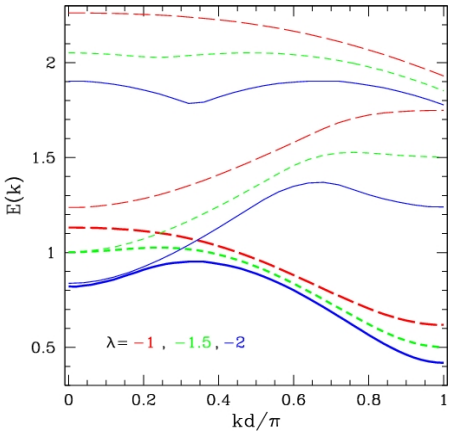

Fig. 2. One particle energies and boundaries of the two-particle continuum at different wavevectors for $\lambda = -1.0$ (red curves), -1.5 (green curves) and -2.0 (blue curves).

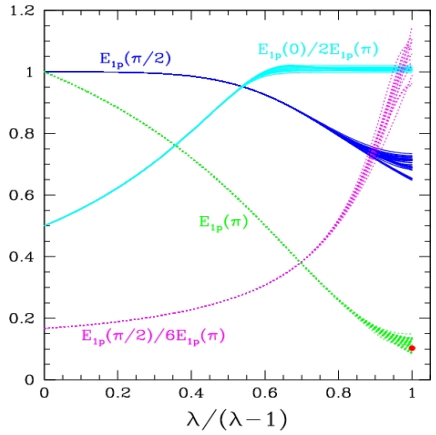

Fig. 3. Single-particle energies and energy ratios at selected wavevectors as a function of λ.

In Fig. 2, we show the one-particle spectra at $\lambda = -1$, -1.5 and -2 obtained through series extrapolation methods together with the upper and lower boundaries of the 2-particle continuum. There are several important features to observe here. First, the peak in the single-particle spectrum has moved away from $k = 0$ and the spectrum is beginning to resemble more the behaviour in Haldane chains. Second, the spectrum near $k = 0$ potentially overlaps with the two-particle spectrum. We find that the single-particle spectrum rather than moving into the continuum and broadening actually merges with the bottom of the continuum. This is consistent with observations on the Haldane chain materials [3].

Fig. 3 shows a plot of the estimated single-particle excitation energy at momenta $kd = \pi/2$ and $kd = \pi$ together with the ratio of those energies and the ratio of the excitation energy at $k = 0$ to that at $kd = \pi$, as functions of λ. Values for various integrated differential approximants are shown. The latter ratio saturates at a value of 2 implying again that the one-particle state merges with the bottom of the continuum at $k = 0$ from this coupling on. It can be seen that $E_{1p}(\pi)$ maps smoothly onto the energy gap for the spin-one chain with an exchange constant of $J/4$ as $\lambda \to \infty$. The red circle indicates the known gap for the spin-one chain.

3. Structure Factors and Spectral Weights

In Fig. 4, we show the evolution of the integrated structure factor as a function of λ. We see that the crossover to the Haldane chain behaviour is related to the development of a short-range antiferromagnetic peak at $kd = \pi$.

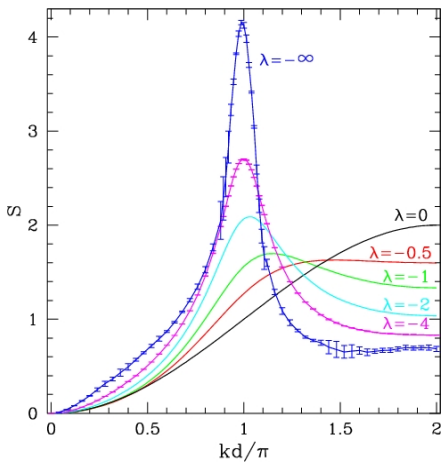

Fig. 4. Evolution of the integrated structure factor S with λ.

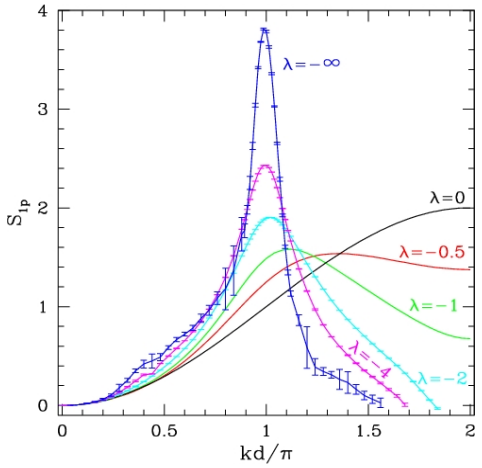

Fig. 5. Single-particle spectral weights (S_{1p}) at different wavevectors as a function of λ.

In Fig. 5, we show the evolution of one-particle spectral weights as a function of λ. We find that in the region where the single-particle spectrum merges with the continuum, its spectral weight becomes very small. Note that the x-axis for this figure runs over $0 < kd < 2\pi$. The spectra are symmetric around $kd = \pi$ and merge with the bottom of the continuum near both $kd = 0$ and $kd = 2\pi$. Near $kd = 0$, the spectral weights are very small to begin with. As the single-particle states merge with the continuum, the weights also become very small near $kd = 2\pi$.

4. Conclusions

We have studied the excitation spectra of the alternating ferromagnetic-antiferromagnetic spin-half chain, and the crossover from the dimerized phase when the antiferromagnetic interactions are stronger to the Haldane phase when the ferromagnetic interactions become stronger. We find that in the former phase the single-particle states are separated from the two-particle continuum and there is a rich spectrum of bound states. In the latter phase the single-particle states are only well defined over part of the Brillouin zone and merge with the bottom of the two-particle continuum near $k = 0$.

Acknowledgments

We thank Steven Nagler, Matt Stone, Oleg Sushkov and Jaan Oitmaa for discussions. This work is supported by a grant from the Australian Research Council and by US National Science Foundation grant number DMR-0240918.

References

[1] A. Kolezuk and S. Sachdev, *Phys. Rev. Lett.* **96**, 087203 (2006).
[2] M.E. Zhitomirsky, *Phys. Rev.* B **73**, 100404 (2006).
[3] S.L. Ma *et al.*, *Phys. Rev. Lett.* **69**, 3571 (1992).
[4] M.B. Stone *et al.*, *Nature* **440**, 187 (2006).
[5] J. Oitmaa, C.J. Hamer and W. Zheng, ``*Series Expansion Methods for Strongly Interacting Lattice Models*" (Cambridge University Press, Cambridge, 2006).
[6] D.A. Tennant *et al.*, *Phys. Rev.* B **67**, 054414 (2003).